Contrast Source Inversion Electrical Property Tomography

Is the two-dimensional CSI algorithm feasible on realistic three-dimensional data?

MSc EE Thesis project EEMCS

Nadine van Dam

Delft University of Technology

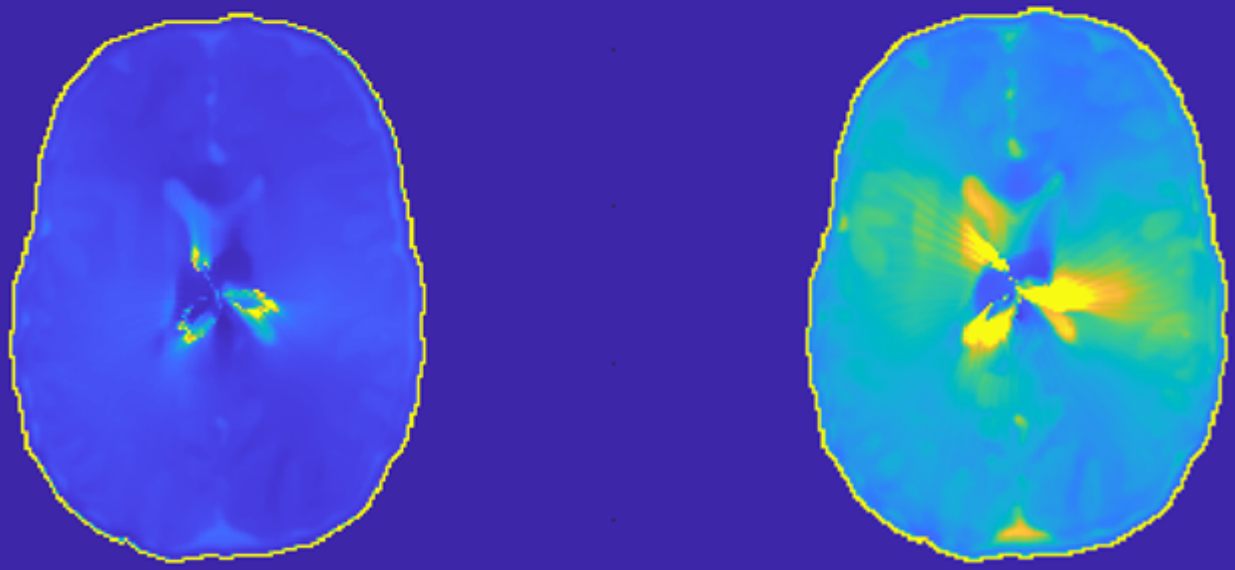

TU Delft

Contrast Source Inversion Electrical Property Tomography

Is the two-dimensional CSI algorithm feasible on realistic three-dimensional data?

by

Nadine van Dam

to obtain the degree of Master of Science
at the Delft University of Technology,
to be defended publicly on Friday August 30, 2024 at 10:00 AM.

Student number:	4912527	
Project duration:	November 16, 2023 – August 30, 2024	
Thesis committee:	Dr. ir. R. F. Remis,	TU Delft, supervisor
	Dr. ir. B. J. Kooij,	TU Delft

Cover:	Conductivity and relative permittivity of the head of the Ella body model.
Style:	TU Delft Report Style, with modifications by Daan Zwaneveld

An electronic version of this thesis is available at `http://repository.tudelft.nl/`.

TU Delft

Preface

From an early age, I wanted to create technologies that help people. During my master's, I searched for a thesis subject that fulfilled this purpose. The Advanced Magnetic Resonance Imaging course made me more aware of the usefulness of an MRI and the opportunities these scanners bring. Therefore, I decided to meet with Rob Remis and was introduced to the subject of EPT and, more specifically, the 2D-CSI algorithm. This subject challenged me to improve my skills in both mathematics and physics. Moreover, I needed to think outside the box to handle multiple issues. Under the supervision of Rob Remis, I have acquired these and many more skills and this thesis would not have been possible without him. Thank you for your support during the previous nine months.

Furthermore, I want to thank Thierry Meerbothe and the Computational Imaging Group for MR Therapy and Diagnostics of the University Medical Centre of Utrecht for creating the ADEPT dataset and helping me with questions about it. I also want to thank Stefano Mandaija and Nico van den Berg from the same group for the interesting talk midway through my thesis. This meeting gave me many new insights, which benefited my understanding and the final product. Besides that, many thanks to Tycho van Velden and Florens Helfferich for the fun discussions on the subject. Additionally, thanks to the Terahertz group for creating a welcoming environment where I could work on my thesis. Bert Jan Kooij, thank you for being a committee member of my thesis defence.

Lastly, I want to thank my friends and family for all the support in the last nine months. Especially, Evelien de Wolff and Renée Hagenman, thank you for cooking dinner when I worked late and helping me in many other ways. Thank you, Willemijn Boeije, for always being there for me and making me laugh at the harder moments. Many thanks to Karel van Dam; I am lucky to be your granddaughter, and your advice was helpful. Last but not least, I want to thank my parents, sister and Jorick. In my off days, you just listened to me and made it possible to move on and create the final product.

Nadine van Dam
Delft, August 18, 2024

Abstract

Electrical property tomography (EPT) reconstructs the human body's conductivity and relative permittivity using the radio frequency field from a magnetic resonance machine. Since conductivity and relative permittivity can be biomarkers for many illnesses, it is necessary to reconstruct them accurately. To this end, this thesis focuses on the two-dimensional tranceive phase corrected contrast source inversion algorithm (2D-CSI).

This 2D-CSI algorithm is significantly faster than its three-dimensional (3D) counterpart. However, reconstruction artefacts may appear since the 2D field description is not always applicable. In this thesis, these artefacts are identified and it is investigated if the 2D-CSI algorithm can be improved to handle them. In particular, the proposed updates are, first, implementing the early stopping principle, then adding a positivity constraint to the conductivity and relative permittivity, and lastly, initialising with Helmholtz electrical property tomography (HEPT). The first two enhancements create a more robust algorithm, while the third update could be useful only in specific cases (with no fine structures and low noise levels).

After achieving a more robust algorithm, the 2D-CSI algorithm is applied to the realistic 3D dataset "A Database for MR-based Electrical Properties Tomography" (ADEPT). The first and foremost challenge is accurately simulating the incident field, as the reconstructions depend a lot on the incident fields. If the incident fields do not match perfectly, the algorithm can only produce satisfactory reconstruction results in a part of the reconstruction domain. The reconstructions are only partly accurate because the reconstructed electric fields converge to a line creating line artefacts. It is shown that small changes in the incident fields produce small changes in the position of the artefacts. Based on this observation, a reconstruction strategy has been developed in which a reconstruction without artefacts is produced by combining reconstruction results of multiple incident fields. Integrating all modifications of the 2D-CSI algorithm in one single framework shows that the conductivity and relative permittivity of the brain in the middle of the birdcage coil can be reconstructed accurately.

Samenvatting

In Elektrische Eigenschappen Tomografie (EPT) wordt de geleiding en de relatieve permittiviteit van het menselijk lichaam gereconstrueerd met behulp van het radiofrequente veld van een MRI. De geleiding en relatieve permittiviteit kunnen biomarkers zijn voor veel ziekten, daarom is het noodzakelijk om ze nauwkeurig te reconstrueren. Om dit doel te bereiken richt dit proefschrift zich op het TweeDimensionale zend- en ontvangfase gecorrigeerd ContrastBron Inversie algoritme (2D-CSI).

Dit 2D-CSI algoritme is aanzienlijk sneller dan zijn DrieDimensionale (3D) tegenhanger. Er kunnen echter reconstructieartefacten optreden omdat de 2D-veldbeschrijving niet altijd toepasbaar is. In dit proefschrift worden deze artefacten geïdentificeerd en wordt onderzocht of het 2D-CSI algoritme kan worden verbeterd om hiermee om te gaan. De voorgestelde updates zijn een implementatie van het vroegtijdig beëindigen van het algoritme bij de kost functie minimum, het toevoegen van de beperking dat de geleidbaarheid en de relatieve permittiviteit altijd positief zijn, en het initialiseren met Helmholtz Elektrische Eigenschappen Tomografie (HEPT). De eerste twee verbeteringen zorgen voor een robuuster algoritme, terwijl de derde update alleen nuttig kan zijn in specifieke gevallen (zonder fijne structuren en met een laag ruisniveau).

Nadat het 2D-CSI algoritme door de verbeteringen robuuster is geworden, wordt het toegepast op de realistische 3D-dataset ”A Database for MR-based Electrical Properties Tomography” (ADEPT). De eerste en belangrijkste uitdaging is het nauwkeurig simuleren van het invallend veld, omdat de reconstructies sterk afhankelijk zijn van de invallende velden. Als de invallende velden niet precies kloppen met de bijbehorende totale velden, kan het algoritme alleen goede reconstructieresultaten opleveren in een deel van het reconstructiedomein. Dit effect wordt veroorzaakt doordat de gereconstrueerde elektrische velden convergeren naar een lijn, waardoor lijnartefacten ontstaan. Er wordt aangetoond dat kleine veranderingen in de invallende velden kleine veranderingen in de positie van de artefacten veroorzaken. Op basis van deze observatie is een reconstructiestrategie ontwikkeld waarbij een reconstructie met minder artefacten wordt geproduceerd door reconstructieresultaten van meerdere incidentvelden te combineren. Door alle aanpassingen van het 2D-CSI algoritme in één enkel raamwerk te integreren, blijkt dat de geleidbaarheid en de relatieve permittiviteit van de hersenen in het midden van de birdcage-spoel nauwkeurig kunnen worden gereconstrueerd.

Contents

Nomenclature

The scalars and vectors are respectively denoted in $italics$ and $\boldsymbol{bold}$ throughout this thesis. The variables in the phasor domain have a $\hat{hat}$. The domain description is given in $\mathbb{BLACKBOARD}$.

Symbols

Symbol	Definition	Unit
$\boldsymbol{A}$	Vector potential	[V]
a	Circle radius centre Greens function	[m]
$\mathbb{A}$	Two dimensional object domain	[m^2]
$\boldsymbol{B}$	Magnetic field	[T]
$\boldsymbol{B}_0$	Static background field	[T]
$\boldsymbol{B}_1$	Radio frequency field	[T]
B_1^+	Transmit field	[T]
B_1^-	Receive field	[T]
c_0	Speed of light	[m/s]
d	Distance to mirror sources	[m]
$\boldsymbol{E}$	Electric field	[V/m]
F	Cost function	[-]
$\boldsymbol{G}$	Gradient field	[T]
$\boldsymbol{g}$	Cost function derivative	[-]
$\mathbf{i}$	Unit vector	[-]
i	Imaginary unit physicists	[-]
$\boldsymbol{J}$	Electric current density	[A/m^2]
j	Imaginary unit engineers	[-]
$\boldsymbol{K}$	Magnetic current density	[V/m^2]
k_0	Wave number in vacuum	[1/$m^{\frac{1}{2}}$]
N	Number of antennas	[-]
$\boldsymbol{r}$	Position vector	[m]
R_A	Coil radius	[m]
R_s	Radio frequency shield radius	[m]
S	Induced signal	[V]
$\boldsymbol{v}$	Update direction	[-]
$\boldsymbol{w}$	Contrast source	[V/m]
α	Step length	[-]
γ	Gyromagnetic ratio	[Hz/T]
ϵ	Permittivity	[F/m]
η	Per-unit-length admittance	[S/m]
η'_B	Data normalization factor	[-]
η'_E	Object normalization factor	[-]
θ	Offset	[-]
κ	Factor	[-]
μ	Permeability	[H/m]
ρ_0	Proton density	[protons/m^3]
σ	Conductivity	[S/m]
τ	Radio frequency pulse duration	[s]
ϕ	Antenna phase	[-]
φ	Phase	[rad]
χ	Contrast function	[-]

Symbol	Definition	Unit
ω	Angular frequency	[rad/s]
ω_0	Larmor frequency	[Hz]

Subscripts and superscripts

Symbol	Definition
$(\cdot)^{ext}$	External
$(\cdot)^{inc}$	Incident
$(\cdot)^{sca}$	Scattered
$(\cdot)^{tot}$	Total
$(\cdot)^{W}$	Weakened
$(\cdot)^{w}$	Contrast source
$(\cdot)^{+}$	Transmit
$(\cdot)^{-}$	Receive
$(\cdot)^{\pm}$	Transceive
$(\cdot)_{A}$	Antenna
$(\cdot)_{B}$	Magnetic
$(\cdot)_{E}$	Electric
$(\cdot)_{M}$	Mirror source
$(\cdot)_{n}$	Iteration n
$(\cdot)_{0}$	Vacuum
$(\cdot)_{r}$	Relative
$(\cdot)_{sc}$	Scaled
$(\cdot)_{x}$	X-direction
$(\cdot)_{y}$	Y-direction
$(\cdot)_{z}$	Z-direction

Operators

Symbol	Definition
$G(\cdot)$	Greens function
$H_0^{(2)}(\cdot)$	Hankel function of second kind and zeroth order
$H_1^{(2)}(\cdot)$	Hankel function of second kind and first order
$J_1(\cdot)$	Bessel function the first kind and first order
$\mathcal{G}_B^{+}\{\cdot\}$	Data operator
$\mathcal{G}_E\{\cdot\}$	Object operator
$\Im\{\cdot\}$	Imaginary part
$\Re\{\cdot\}$	Real part
∂_k	Partial derivative towards k
∂^{+}	Wirtinger derivative $(\frac{1}{2}(\partial_x + j\partial_y))$
∂^{-}	Wirtinger derivative $(\frac{1}{2}(\partial_x - j\partial_y))$
∇	Gradient
∇^2	Laplacian
$\nabla\times$	Curl
$\nabla\cdot$	Divergence
$\angle$	Angle
$\times$	Cross product
$\left\|\cdot\right\|$	Euclidean norm
$\left\langle\cdot,\cdot\right\rangle$	Inner product
$\left\|\cdot\right\|$	Magnitude

Symbol	Definition
$(\cdot)^{\dagger}$	Adjoint
$(\cdot)^{*}$	Complex conjugate

Abbreviations

Abbreviation	Definition
2D	Two-dimensional
3D	Three-dimensional
ADEPT	A Database for MR-based Electrical Properties Tomography
AFI	Actual Flip angle Imaging
AT	Active Tumor
BSS	Bloch-Siegert Shift
bSSFP	balanced Steady-State Free Precession
CSF	CerebroSpinal Fluid
CSI	Contrast Source Inversion
DAM	Double-Angle Method
DREAM	Dual Refocusing Echo Acquisition Mode
EP	Electrical Property
EPT	Electrical Property Tomography
foIC-EPT	First order induced current EPT
GM	Gray Matter
GMT	Global Maxwell Tomography
HEPT	Helmholtz EPT
LMT	Local Maxwell Tomography
MR	Magnetic Resonance
NET	Non-Enhancing Tumor
RF	Radio Frequency
SAR	Specific Absorption Rate
SNR	Signal-to-Noise Ratio
TEPT	Transverse EPT
TPA	Tranceive Phase Assumption
WM	White Matter

1 Introduction

Cancer is an illness which affects many people around the world. The International Agency for Research on Cancer estimates approximately 20 million new cancer cases and 9.7 million deceased from cancer in 2022 [1]. Early detection can help to reduce dying as early treatment is more effective [2].

Currently, there are multiple methods to detect cancer. Examples are biopsies, roentgen, ultrasound, and magnetic resonance (MR) imaging. A biopsy can give accurate results. However, it is invasive, and the wound can be painful. On the other hand, non-invasive methods such as ultrasound and X-rays have different limitations. Ultrasound can capture tissues using sound, although the sound has difficulties penetrating hard tissues, resulting in bad-quality images of tissues inside bones [3]. The X-ray uses roentgen radiation, which shows clear images of hard tissues, while soft tissue is more challenging to image [3]. Another significant disadvantage is that this radiation can damage the patient's tissue [3]. The MR imaging can accurately show the soft and hard tissue and is far less hazardous than the roentgen images. Therefore, MR imaging is a favourable tool for imaging patients.

Conventional MR images are created by applying a radio frequency (RF) magnetic field to disturb the magnetic fields in the body, and the relaxation time of different tissue types creates the images. Instead of considering the relaxation times, the RF field in each pixel could be determined to find the Electric Properties (EPs) of the tissue inside the body. This method is called Electrical Property Tomography (EPT). The EPs can function as biomarkers for health issues such as cancer, cysts, and strokes [4, 5, 6, 7, 8, 9]. Therefore, EPT images are preferred above conventional MR images. The EPs include conductivity and relative permittivity. In the cancerous regions, strokes and cysts, the conductivity is increased [4, 10]. Hence, especially knowledge about conductivity can help determine a patient's health.

In addition to finding abnormalities, EPT can be useful for calculating the Specific Absorption Rate (SAR). SAR measures the absorption of the electric field, which is safe for the body. If the SAR is exceeded, the body can be harmed. Especially at high-field MR machines (for example, a background magnetic field of 7T), the SAR can be violated during the scan. Unfortunately, this SAR is different for every individual. To avoid damage to the patient, there are large safety margins. However, if the SAR can be measured simultaneously with the MR imaging scan, this is not necessary. This procedure increases the image quality as more information can be obtained. Hence, EPT could be a valuable tool to acquire more knowledge about the patient's health and avoid damage to the patient's tissue [4, 5].

The EPT research area can be divided into two subareas: acquiring the radio frequency magnetic field and reconstructing the EPs from the radio frequency magnetic field. Most research, including this thesis, is done on the reconstruction of the EPs, as this area allows for many reconstruction algorithms which can be optimized. The reconstruction algorithms can be divided into the local, the global and the combinations algorithms. The local algorithms often use the (second-order) derivative of the RF field. These algorithms are easy to implement and fast. Unfortunately, the derivatives blow up around tissue boundaries, resulting in inaccurate reconstructions at edges. Moreover, the noise gets amplified in the

presence of noise, resulting in unreliable reconstructions. Helmholtz-EPT (HEPT) and Local Maxwell Tomography (LMT) are examples of solely local algorithms [9].

The global methods, such as Contrast Source Inversion (CSI) [11] and Global Maxwell Tomography (GMT) [9], often use an iterative approach to find the EPs. These global methods are less noise-sensitive and do not have boundary issues. Unfortunately, these methods take longer and are harder to implement than the local approaches. Furthermore, the iterative approach flattens the data. However, even with the flattened data, these methods create more accurate reconstructions than the local methods.

The methods which are both local and global (Transverse EPT (TEPT) [12] and first order induced current EPT (foIC-EPT) [13]) are easier to implement and faster than the full global methods. Moreover, the combination algorithms have fewer boundary and noise issues than the full local approaches. However, the combination methods still fail earlier with high noise levels compared to the global methods, making it less preferable than the full global methods.

Therefore, the focus of this research is on the CSI method. More specifically, the two-dimensional (2D) CSI algorithm is implemented. This algorithm is 2D, assuming that the electric field is fully directed in the longitudinal direction while the RF field only has components in the transversal plane [14]. In the three-dimensional (3D) CSI algorithm, this assumption is not considered to make it more realistic, but at the cost of a much more complex, computationally heavy, and slow algorithm [7]. These disadvantages of the 3D-CSI algorithm make it necessary to see if the 2D-CSI algorithm could be used instead. However, the 2D-CSI algorithm needs to be enhanced to achieve similar-quality images. This thesis investigates multiple improvements on two datasets.

This thesis uses the HEPT method beside the 2D-CSI algorithm for comparison. In Figure 1.1, a brain slice with fine structures is reconstructed with both HEPT and CSI. From the HEPT reconstruction, the problems around boundaries can be seen easily. This results in an image which misses fine details from the original data. The CSI algorithm is closer to the original; however, the reconstruction seems to be a filtered version of the original data, and the relative permittivity reconstruction is not completely accurate.

The algorithms are implemented on two datasets. First, a dataset is considered, named the ”Ella dataset”, throughout the paper. This dataset includes conductivity and relative permittivity information of multiple slices of the Ella body model from the Virtual Family [15]. The EPs create the corresponding magnetic and electric fields under the 2D assumption. Hence, the created fields only include 2D information. Therefore, applying the 2D-CSI algorithm seems straightforward. Note that this dataset does not include error sources created by an MR machine, such as the limited length of the antennas. From this dataset, the reconstruction of multiple different body parts is possible. However, the other dataset only includes brain models. Therefore, the focus is on brain reconstruction for the Ella dataset. Appendix B discusses the other body parts.

The second dataset is provided by T.G. Meerbothe et al. from the University Medical Center Utrecht [16]. This dataset is called ”A Database for MR-based Electrical Properties Tomography” or, in short, ADEPT. The ADEPT dataset includes electric and magnetic field data and the EPs of multiple brain models. These fields are created with the Sim4Life simulation platform, which applies more information about the MR machine. Moreover, it creates more realistic 3D fields. Besides that the data is more realistic, there are brain models which include tumour tissue as well. Therefore, the algorithm can also be tested to reconstruct data with tumors. As this dataset includes 3D fields, it might sound more reasonable to use the 3D-CSI algorithm. Unfortunately, as mentioned before, the 3D-CSI algorithm takes much longer than the 2D-CSI algorithm [8]. Therefore, it is investigated if using the 2D-CSI algorithm to reconstruct a slice in a 3D dataset is possible.

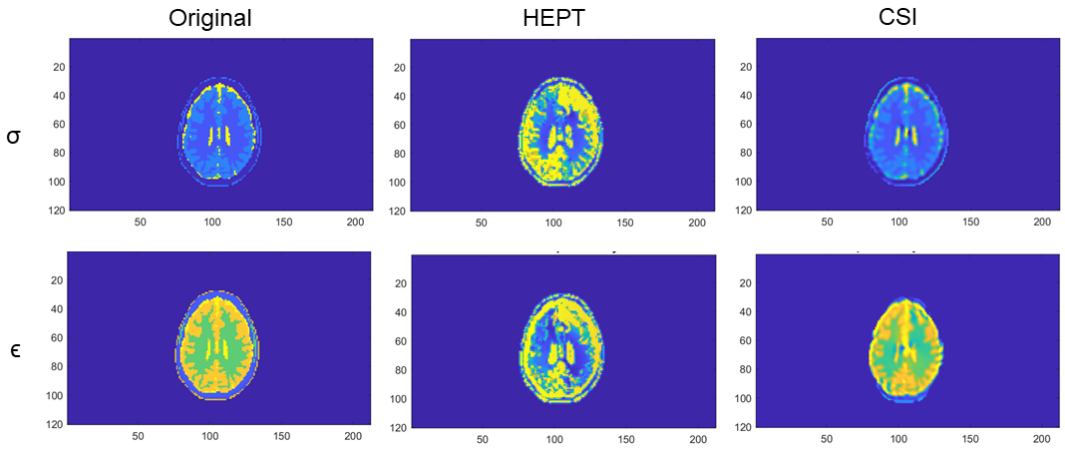

Figure 1.1: Comparison between the reconstruction of HEPT and CSI. The top and bottom rows show the conductivity and relative permittivity, respectively. The first column represents the original slice, the middle displays the HEPT reconstruction, and the last presents the CSI reconstruction. The data on which the algorithms are applied is slice 320 of the Ella body model (from the Virtual Family [15]) using 2.5 mm resolution.

1.1. Research question

The following research question provides the scope of the project:

How well does the two-dimensional Contrast Source Inversion algorithm perform in finding the Electrical Properties from realistic three-dimensional field data of the human brain?

To reach an answer to this question, some sub-questions are designed:

- *SQ1* How can the 2D-CSI algorithm be improved to be more robust for the 3D data?
- *SQ2* How should the incident fields be adjusted to fit the 3D data?
- *SQ3* How can information of multiple images be combined automatically?

Note that the CSI algorithm has multiple versions. In this paper, the multiplicative regularisation is not implemented, but in each iteration, the RF field phase is updated to match the physics better.

1.2. Contribution

During this thesis project, some contributions have been made to improve the reconstruction with the 2D-CSI algorithm. These contributions are categorized into the corresponding sub-question:

- *C1a* The reconstruction at the cost function minimum is superior to later reconstructions as errors due to failing assumptions are modelled in later iterations.
- *C1b* A positivity constraint is implemented to help the algorithm converge to a correct minimum as the phase reconstruction of the RF field becomes more realistic.
- *C2a* The dependence of the magnitude of the incident fields and the reconstruction is investigated.
- *C2b* The offset of the incident fields changes the reconstruction.
- *C3* The locations which are not redirected by the positivity constraint include the accurate reconstructions.

The contributions of C1a and C1b were implemented on both the 2D Ella dataset and the 3D ADEPT dataset and showed improved reconstructions. The contributions C2a, C2b, and C3 were only applied in the ADEPT dataset.

1.3. Outline

The thesis is structured as follows. First, a mathematical background is provided in Chapter 2. After that, some improvements to the 2D-CSI algorithm are proposed and implemented to reconstruct the EPs of the Ella dataset in Chapter 3. Next, in Chapter 4, the 2D-CSI algorithm is applied to the ADEPT dataset to create useful reconstructions. Lastly, conclusions are drawn in Chapter 5.

2 Method

In this chapter, the 2D-CSI algorithm is explained in detail. However, it is essential to start with some background about EPT. To understand the physics behind EPT better, some background knowledge about MR machines is necessary. The MR machine creates a static background field ($\boldsymbol{B}_0$). When the imaging object lies inside the MR machine, the magnets create a net magnetisation in the body. The images are created by applying two additional fields: an RF field ($\boldsymbol{B}_1$) and a gradient field ($\boldsymbol{G}$). This RF field is used to bring the net magnetisation out of equilibrium, and the gradient field creates focus on a specific area in the body. Different tissue types of the body react differently on the RF field due to the distinct electrical properties of the tissue. The received RF field thus holds EP information. As mentioned in the introduction, part of the research in EPT is on the $\boldsymbol{B}_1$ mapping. This $\boldsymbol{B}_1$ mapping includes finding the magnitude and phase of the RF field. Before a small summary of the different $\boldsymbol{B}_1$ mapping can be explained, it is necessary to understand more about the RF field.

2.1. Background Mathematics

2.1.1. Radio frequency field

When a person lies inside an MR machine, a large static magnetic field, $\boldsymbol{B}_0$, aligns the protons in the body, resulting in a net magnetisation. The net magnetisation rotates in a left-handed manner with the Larmor frequency ($\omega_0 = \gamma \boldsymbol{B}_0$, where γ is the gyromagnetic ratio) around the $\boldsymbol{B}_0$ field assuming that the $\boldsymbol{B_0}$ field is in the negative z direction (negative longitudinal direction). A second smaller field is then applied, which rotates with the same frequency. This field is the radio frequency field $\boldsymbol{B}_1$ and can be divided into two parts: a part which rotates left-handed, resulting in the transmit field $\boldsymbol{B}_1^+$, and a right-handed field called the receive field $\boldsymbol{B}_1^-$. The transmit field in the phasor domain is defined as

$$\hat{\boldsymbol{B}}_1^+(\boldsymbol{r}, j\omega) = \hat{B}_1^+(\boldsymbol{r}, j\omega)(\mathbf{i}_x - j\mathbf{i}_y) \text{ with } \hat{B}_1^+(\boldsymbol{r}, j\omega) = \frac{\hat{B}_{1,x}(\boldsymbol{r}, j\omega) + j\hat{B}_{1,y}(\boldsymbol{r}, j\omega)}{2} \tag{2.1}$$

and the receive field is defined as

$$\hat{\boldsymbol{B}}_1^-(\boldsymbol{r}, j\omega) = \left[\hat{B}_1^-(\boldsymbol{r}, j\omega)\right]^\dagger (\mathbf{i}_x + j\mathbf{i}_y) \text{ with } \hat{B}_1^-(\boldsymbol{r}, j\omega) = \left[\frac{\hat{B}_{1,x}(\boldsymbol{r}, j\omega) - j\hat{B}_{1,y}(\boldsymbol{r}, j\omega)}{2}\right]^\dagger, \tag{2.2}$$

where $\mathbf{i}_x$ and $\mathbf{i}_y$ are the unit vectors in respectively the x and y directions, $\boldsymbol{r}$ is the position vector, $\hat{B}_{1,x}$ and $\hat{B}_{1,y}$ are the RF fields in the x and y direction, and the dagger denotes the adjoint. The transmit field rotates with the net magnetisation, which influences the net magnetisation. This influence depends on the tissue type; therefore, the transmit field contains information about the underlying EPs of the tissue. Hence, most EPT algorithms use the transmit field in the reconstruction algorithm. The transmit field is acquired with the B_1 mapping.

B_1 mapping

As mentioned, a separate research area focuses on B_1 mapping. However, it is important to know some fundamental challenges that affect reconstruction. In B_1 mapping, the induced signal caused

by the changes in the net magnetisation due to the RF field is used as a starting point. A simplified equation for the induced signal is

$$S(\boldsymbol{r}, j\omega) = \sin(\gamma\tau \left|\hat{B}_1^+(\boldsymbol{r}, j\omega)\right|) \exp\left[j\hat{\varphi}^{\pm}(\boldsymbol{r}, j\omega)\right] \rho_0(\boldsymbol{r}) \left|\hat{B}_1^-(\boldsymbol{r}, j\omega)\right|, \tag{2.3}$$

where τ, ρ_0, and $\varphi^{\pm} = \varphi^+ + \varphi^-$ are the RF pulse duration, the spatial-dependent proton density, and transceive phase, respectively [5, 9, 10, 17]. In the equation, it can be observed that the transmit field magnitude exhibits non-linear behaviour. Therefore, it is relatively easy to determine the $\left|\hat{B}_1^+(\boldsymbol{r}, j\omega)\right|$ using multiple acquisitions. Methods which have been explored are the Double-Angle Method (DAM) [18], Bloch-Siegert Shift (BSS) [19], Actual Flip angle Imaging (AFI) [20], and Dual Refocusing Echo Acquisition Mode (DREAM) [21].

The phase of the transmit field is more difficult to determine as it is entangled with the receive phase. However, it is known that the transmit and receive fields are very similar for symmetric objects in circularly polarised fields [10]. Hence, it can be assumed that

$$\varphi^+ = \frac{\varphi^{\pm}}{2}, \tag{2.4}$$

which is often denoted as the Transceive Phase Assumption (TPA) [4, 5, 8, 11, 12, 13, 10, 17]. The transceive phase can be found using different sequences. For example, Van Lier proposes to use two spin-echo sequences [22], while Gavazzi took a balanced Steady-State Free Precession (bSSFP) and a phase cycled bSSFP sequence into account [23].

Many algorithms only require knowledge about the transmit field, not the receive field. On the other hand, when the receive field is known, it is possible to check if the reconstructions are physically reliable. Therefore, there are studies which estimate the magnitude of the receive field. The main challenge is that the magnitude of the receive field is multiplied by the spatial-dependent proton density.

Recently, some machine learning algorithms have been proposed for the B_1-mapping [24, 25]. These algorithms need large datasets to estimate the magnitude and phase of the $\hat{B}_1^+$ field correctly. However, the results from these machine learning algorithms are promising.

Time convention

Another important consideration is the direction of the RF field components. This direction depends on the chosen direction of the $\boldsymbol{B}_0$ field and the time convention selected to reach the phasor domain. The chosen time convention in the 2D-CSI algorithm is $\exp(j\omega)$ (equal to the time convention of an engineer); however, the time convention selected in the ADEPT dataset is $\exp(-i\omega)$ (equal to the time convention of a physicist). Therefore, the fields of the ADEPT dataset can be adjusted to fit the algorithm. This adjustment of the fields can be done with the conversion formulas

$$\hat{B}_1^+(\boldsymbol{r}, j\omega) = \left[\hat{B}_1^-(\boldsymbol{r}, -i\omega)\right]^* \text{ and } \hat{B}_1^-(\boldsymbol{r}, j\omega) = \left[\hat{B}_1^+(\boldsymbol{r}, -i\omega)\right]^*, \tag{2.5}$$

where asterisk represents the complex conjugate. Besides converting the magnetic field, the electric field is adjusted to handle the time convention change. This conversion is done with the following formula

$$\hat{E}_z(\boldsymbol{r}, j\omega) = \left[\hat{E}_z(\boldsymbol{r}, -i\omega)\right]^*. \tag{2.6}$$

The description of the transmit field can be used for the 2D-CSI algorithm. This RF field and additional physical relations are verified to make the algorithm robust to noise. These physical relations come from the Maxwell equations.

2.1.2. Maxwell equations

The starting point for the physical relations behind EPT is the time-harmonic Maxwell equations (in the phasor domain shown with a circumflex). These are the Ampère-Maxwell law :

$$-\nabla \times \hat{\boldsymbol{B}} + \hat{\eta}\mu\hat{\boldsymbol{E}} = -\mu\hat{\boldsymbol{J}}^{ext}, \tag{2.7}$$

and Faraday's law:

$$\nabla \times \hat{\boldsymbol{E}} + j\omega\hat{\boldsymbol{B}} = -\hat{\boldsymbol{K}}^{ext}. \tag{2.8}$$

In these equations $\hat{\eta}$, μ, ω, and j are per-unit-length admittance, permeability, angular frequency, and the imaginary unit, respectively. The per-unit-length admittance can be formulated as $\hat{\eta} = \sigma + j\omega\epsilon_0\epsilon_r$ in which σ is the conductivity and ϵ_0, and ϵ_r are respectively the permittivity in vacuum and the relative permittivity. Moreover, $\hat{\boldsymbol{J}}^{ext}$ is the external electric current density, and $\hat{\boldsymbol{K}}^{ext}$ the external magnetic current density. In the case of EPT, there are no external electric- and magnetic-current densities present in the body [9] therefore those are equal to zero. Furthermore, the tissue permeability is almost constant throughout the body and is assumed to be equal to the permeability of vacuum (μ_0). This results in the following equations:

$$-\nabla \times \hat{\boldsymbol{B}} + \hat{\eta}\mu_0\hat{\boldsymbol{E}} = \boldsymbol{0}, \tag{2.9}$$

and

$$\nabla \times \hat{\boldsymbol{E}} + j\omega\hat{\boldsymbol{B}} = \boldsymbol{0}. \tag{2.10}$$

2.2. Two-dimensional Contrast Source Inversion algorithm

Van den Berg and Kleinman proposed the CSI algorithm in 1997 [26]. Since then, the algorithm has been applied to different inversion problems such as the reconstruction of geological structures using full-waveform seismic information [27], spoilage detection of grain with microwave imaging [28], and borehole logging from electromagnetic measurements [29]. The first time CSI was applied to the EPT problem was in 2013 by Balidema et al. [30]. Thereafter, much research has been performed in improving the CSI algorithm [11, 9, 31, 14].

In the 2D formalism, it is assumed that the fields are E-polarized in the middle of a birdcage coil [32, 33]. Therefore, it is assumed that there is only a longitudinal component for the electric field $\boldsymbol{E} = E_z\boldsymbol{i}_z$ and the magnetic field is solely in the transversal plane $\boldsymbol{B} = B_x\boldsymbol{i}_x + B_y\boldsymbol{i}_y$. This assumption simplifies the algorithm, which makes the algorithm faster. Leijsen formulated the full 3D formalism [7].

2.2.1. Scattering formalism

CSI adopts the scattering formalism and divides the entire field into the incident and scattered fields. Figure 2.1 shows a schematic of this scattered formalism and

$$\{\hat{\boldsymbol{E}}, \hat{B}_1^+\} = \{\hat{\boldsymbol{E}}^{inc}, \hat{B}_1^{+;inc}\} + \{\hat{\boldsymbol{E}}^{sca}, \hat{B}_1^{+;sca}\} \tag{2.11}$$

shows the corresponding equation, where the incident fields, $\{\hat{\boldsymbol{E}}^{inc}, \hat{B}_1^{+;inc}\}$, are the fields which are present even when the imaging object is not inside the MR machine. This field can be measured or simulated and, therefore, known beforehand. On the other hand, the imaging object creates the scattered fields. For the 2D scattered fields, the magnetic and electric fields can be represented by

$$\hat{B}_1^{+;sca}(\boldsymbol{r}) = \frac{\omega}{c_0^2}\partial^+\hat{\boldsymbol{A}}^{sca}(\boldsymbol{r}), \text{ and } \hat{\boldsymbol{E}}^{sca}(\boldsymbol{r}) = k_0^2\hat{\boldsymbol{A}}^{sca}(\boldsymbol{r}), \tag{2.12}$$

where $\partial^+ = \frac{1}{2}(\partial_x + j\partial_y)$ is the Wirtinger derivative, $\boldsymbol{r}$ is the position vector of the observation point, c_0 light speed in a vacuum, $k_0 = \dfrac{\omega}{c_0}$ the wave number in a vacuum, and the scattered vector potential is

$$\hat{\boldsymbol{A}}^{sca}(\boldsymbol{r}) = \int_{\boldsymbol{r}'\in\mathbb{A}} \hat{G}(\boldsymbol{r}-\boldsymbol{r}')\hat{\boldsymbol{w}}(\boldsymbol{r}')dS, \tag{2.13}$$

where $\boldsymbol{r}'$ is the position vector of the source point, the $\hat{G}(\boldsymbol{r})$ is the 2D Green's function, $\mathbb{A}$ the object domain, and $\hat{\boldsymbol{w}}(\boldsymbol{r})$ the contrast source [8, 14]. The 2D Green's function is given by

$$\hat{G}(\boldsymbol{r}) = -\frac{j}{4}H_0^{(2)}(k_0|\boldsymbol{r}|), \tag{2.14}$$

where $H_0^{(2)}(\cdot)$ denotes the Hankel function of the second kind zeroth order [8, 14]. The contrast source is defined as

$$\hat{\boldsymbol{w}}(\boldsymbol{r}) = \hat{\chi}(\boldsymbol{r})\hat{\boldsymbol{E}}(\boldsymbol{r}), \tag{2.15}$$

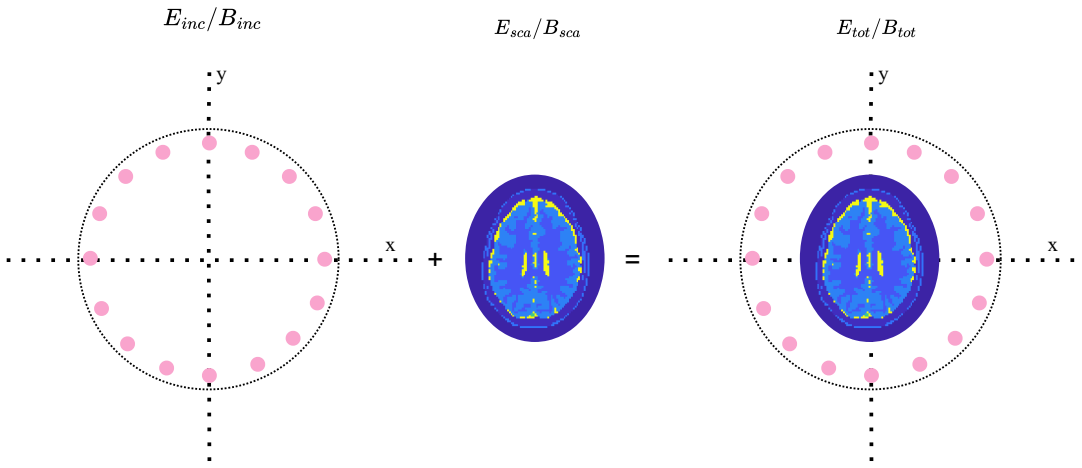

Figure 2.1: Schematic of the scattering formalism. On the left, an empty coil used for the incident field is shown, where the pink dots represent the antenna positions, and the dotted circle is the RF shield surrounding the antennas. In the middle, the head is given as a scattered object. On the right, the situation with the total field is demonstrated.

where $\hat{\chi}$ is the contrast function which can be described as

$$\hat{\chi}(\boldsymbol{r}) = \frac{\hat{\eta}(\boldsymbol{r}) - \hat{\eta}_0}{\hat{\eta}_0} = \epsilon_r(\boldsymbol{r}) - 1 - \frac{j\sigma(\boldsymbol{r})}{\omega\epsilon_0}, \tag{2.16}$$

using $\hat{\eta}_0 = j\omega\epsilon_0$. The scattered transmit field in Equation 2.12 is referred to as the data equation and is often written more compactly as

$$\hat{B}_1^{+;sca}(\boldsymbol{r}) = \mathcal{G}_B^+\{\hat{\boldsymbol{w}}\}. \tag{2.17}$$

Moreover, the scattered electric field is often shortened to

$$\hat{\boldsymbol{E}}^{sca}(\boldsymbol{r}) = \mathcal{G}_E\{\hat{\boldsymbol{w}}\}. \tag{2.18}$$

The object equation is then reached by multiplying the electric fields of Equation 2.11 with the contrast,

$$\hat{\boldsymbol{w}}(\boldsymbol{r}) = \hat{\chi}\hat{\boldsymbol{E}}^{inc}(\boldsymbol{r}) + \hat{\chi}\mathcal{G}_E\{\hat{\boldsymbol{w}}(\boldsymbol{r})\}. \tag{2.19}$$

2.2.2. Cost function

From equation 2.16, it is clear that the contrast and (indirectly) the contrast source include the EPs; therefore, the contrast and contrast source should be accurately determined during the CSI process. A cost function is introduced to successfully determine the contrast and contrast source, which tries to minimise the error with the data and object equation [7]. Minimising the data equation error ensures the result is close to the MR data. The object equation error should be minimised to satisfy Maxwell's equation. Therefore, the cost function for the simplest 2D-CSI algorithm becomes

$$F(\hat{\boldsymbol{w}}, \hat{\chi}) = \frac{\left\|\hat{B}^{+;sca} - \mathcal{G}_B^+\{\hat{\boldsymbol{w}}\}\right\|_{\mathbb{A}}^2}{\left\|\hat{B}_1^{+;sca}\right\|_{\mathbb{A}}^2} + \frac{\left\|\hat{\chi}\hat{\boldsymbol{E}}^{inc} - \hat{\boldsymbol{w}} + \hat{\chi}\mathcal{G}_E\{\hat{\boldsymbol{w}}\}\right\|_{\mathbb{A}}^2}{\left\|\hat{\chi}\hat{\boldsymbol{E}}^{inc}\right\|_{\mathbb{A}}^2}, \tag{2.20}$$

where the first term represents the normalised data equation error and the second term the normalised object equation error [9].

However, the measured magnetic field's phase is not the transmit but the transceive phase. The transmit phase can be determined using the known transceive and unknown receive phases ($\varphi^+ = \varphi^\pm - \varphi^-$). Therefore, if the receive phase is included in the cost function, the results should have fewer

issues related to the TPA. This approach is often called Transceive Phase Correct (TPC) CSI-EPT. The cost function becomes

$$F(\hat{\boldsymbol{w}},\hat{\chi},\varphi^{-}) = \frac{\left\| \left|\hat{B}_1^{+}\right| e^{j\varphi^{\pm}} e^{-j\varphi^{-}} - \mathcal{G}_B^{+}\{\hat{\boldsymbol{w}}\} - \hat{B}_1^{+;inc} \right\|_{\mathbb{A}}^2}{\left\| \left|\hat{B}_1^{+}\right| e^{j\varphi^{\pm}} e^{-j\varphi^{-}} - \hat{B}_1^{+;inc} \right\|_{\mathbb{A}}^2} + \frac{\left\| \hat{\chi}\hat{\boldsymbol{E}}^{inc} - \hat{\boldsymbol{w}} + \hat{\chi}\mathcal{G}_E\{\hat{\boldsymbol{w}}\} \right\|_{\mathbb{A}}^2}{\left\| \hat{\chi}\hat{\boldsymbol{E}}^{inc} \right\|_{\mathbb{A}}^2}, \tag{2.21}$$

[14]. The normalisation factors are necessary to ensure that the optimisation focuses on the data and object equation equally. To simplify the expressions, these normalization factors can be defined as single variables as

$$\eta'_B = \left(\left\| \left|\hat{B}_1^{+}\right| e^{j\varphi^{\pm}} e^{-j\varphi^{-}} - \hat{B}_1^{+;inc} \right\|_{\mathbb{A}}^2 \right)^{-1} \text{ and } \eta'_E = \left(\left\| \hat{\chi}\hat{\boldsymbol{E}}^{inc} \right\|_{\mathbb{A}}^2 \right)^{-1}, \tag{2.22}$$

where η'_B and η'_E correspond to the data and object equation. The cost function is minimised by fixing all except one variable, updating this variable, and repeating until all variables have been updated. The order of updating is first the contrast source, then the contrast and lastly the receive phase.

2.2.3. Updating the contrast source

The contrast source is updated using the formula

$$\hat{\boldsymbol{w}}_n = \hat{\boldsymbol{w}}_{n-1} + \alpha_n^w \boldsymbol{v}_n, \tag{2.23}$$

where $\hat{\boldsymbol{w}}_{n-1}$, $\alpha_n^{\boldsymbol{w}}$ and $\boldsymbol{v}_n$ are the previous contrast source, the step length and the update direction, respectively. The update direction is the Polak-Ribière conjugate gradient update direction:

$$\boldsymbol{v}_n = \boldsymbol{g}_n^w + \frac{\Re\left\{ \left\langle \boldsymbol{g}_n^w, \boldsymbol{g}_n^w - \boldsymbol{g}_{n-1}^w \right\rangle_{\mathbb{A}} \right\}}{\left\| \boldsymbol{g}_{n-1}^w \right\|_{\mathbb{A}}^2} \boldsymbol{v}_{n-1} \text{ with } \boldsymbol{v}_0 = \boldsymbol{0}, \tag{2.24}$$

where the $\langle \cdot,\cdot \rangle_{\mathbb{A}}$ denotes the inner product and $\boldsymbol{g}_n^w$ is the gradient of the cost function with respect to the contrast source [34]. This gradient can be obtained by

$$\boldsymbol{g}_n^w = -\left[\eta'_B \mathcal{G}_B^{+;\dagger} \left\{ \left|\hat{B}_1^{+}\right| e^{j\varphi^{\pm}} e^{-j\varphi_{n-1}^{-}} - \mathcal{G}_B^{+}\{\hat{\boldsymbol{w}}_{n-1}\} - \hat{B}_1^{+;inc} \right\} + \eta'_E \left(\hat{\boldsymbol{E}}_{n-1} - \mathcal{G}_E^{\dagger}\left\{ \hat{\chi}_{n-1}^{\dagger} \hat{\boldsymbol{E}}_{n-1} \right\} \right) \right], \tag{2.25}$$

where $\mathcal{G}_B^{+;\dagger}$ and $\mathcal{G}_E^{\dagger}$ are the adjoint Green's operators of $\mathcal{G}_B^{+}$ and $\mathcal{G}_E$ respectively, and the asterisk denotes the complex conjugate [34]. Next, to determine the real step length, the following minimisation problem needs to be solved [34]:

$$\alpha_n^w = \underset{\alpha}{\text{argmin}} \left[F(\hat{\boldsymbol{w}}_{n-1} + \alpha \boldsymbol{v}_n, \hat{\chi}_{n-1}, \varphi_{n-1}^{-}) \right]. \tag{2.26}$$

This minimisation problem leads to a step length of

$$\alpha_n^w = \frac{-\Re\left\{ \left\langle \boldsymbol{g}_n^w, \boldsymbol{v}_n \right\rangle_{\mathbb{A}} \right\}}{\eta'_B \left\| \mathcal{G}_B^{+}\left\{ \boldsymbol{v}_n \right\} \right\|_{\mathbb{A}}^2 + \eta'_{E,n} \left\| \boldsymbol{v}_n - \hat{\chi}_{n-1} \mathcal{G}_E\left\{ \boldsymbol{v}_n \right\} \right\|_{\mathbb{A}}^2}. \tag{2.27}$$

The above-described update direction and step length can now be substituted in Equation 2.26. Lastly, the initialisation of the contrast source can have large effects on the resulting reconstructions as an incorrect initialisation might lead to local minima [31]. However, often, the initialisation is calculated by back projection. Throughout this thesis, the back projection will be used unless stated otherwise. The initial contrast source is then obtained by

$$\hat{\boldsymbol{w}}_0 = \frac{\left\| \mathcal{G}_B^{+;\dagger}\left\{ \hat{B}_1^{+} \right\} \right\|_{\mathbb{A}}^2}{\left\| \mathcal{G}_B^{+}\left\{ \mathcal{G}_B^{+;\dagger}\left\{ \hat{B}_1^{+} \right\} \right\} \right\|_{\mathbb{A}}^2} \mathcal{G}_B^{+;\dagger}\left\{ \hat{B}_1^{+} \right\}. \tag{2.28}$$

Algorithm 1 2D-Contrast Source Inversion

Initialize $\hat{\boldsymbol{w}}_0$, and corresponding $\hat{\chi}_0$, $\hat{\boldsymbol{E}}_0$, and φ_0^-
  while $n \leq N$ **do**
    Fix $\hat{\boldsymbol{E}}_{n-1}$, $\hat{\chi}_{n-1}$, and φ_{n-1}^- to update $\hat{\boldsymbol{w}}_n = \hat{\boldsymbol{w}}_{n-1} + \alpha_n^w \boldsymbol{v}_n$
    Fix $\hat{\boldsymbol{w}}_n$, $\hat{\chi}_{n-1}$, and φ_{n-1}^- to update $\hat{\boldsymbol{E}}_n = \hat{\boldsymbol{E}}^{inc} + \mathcal{G}_E\{\hat{\boldsymbol{w}}_n\}$
    Fix $\hat{\boldsymbol{w}}_n$, $\hat{\boldsymbol{E}}_n$, and φ_{n-1}^- to update $\hat{\chi}_n = \frac{\hat{\boldsymbol{w}}_n \cdot \hat{\boldsymbol{E}}_n^\dagger}{|\hat{\boldsymbol{E}}_n|^2}$
    Fix $\hat{\boldsymbol{w}}_n$, $\hat{\boldsymbol{E}}_n$, and $\hat{\chi}_n$ to update $\varphi_n^- = \angle(\hat{B}_{1;n}^{-;sca} + \hat{B}_1^{-;inc})$
    if $F_n(\hat{\boldsymbol{w}}_n, \hat{\chi}_n, \varphi_n^-) <$ tolerance **then**
      Break
  Calculate $\epsilon_r = \Re\{\chi\} + 1$
  Calculate $\sigma = -\omega\epsilon_0 \Im\{\chi\}$

2.2.4. Updating the contrast

If the contrast source is known, the total electric field is updated

$$\hat{\boldsymbol{E}}_n = \hat{\boldsymbol{E}}^{inc} + \mathcal{G}_E\left\{\hat{\boldsymbol{w}}_n\right\}. \tag{2.29}$$

This updated electric field is necessary to calculate the new contrast. The contrast is determined by minimising the least squares problem

$$\hat{\chi}_n = \min_{\chi} \left\| \hat{\boldsymbol{w}}_n - \chi \hat{\boldsymbol{E}}_n \right\|_{\mathbb{A}}^2. \tag{2.30}$$

Therefore, the contrast is updated using the equation

$$\hat{\chi}_n = \frac{\hat{\boldsymbol{w}}_n \cdot \hat{\boldsymbol{E}}_n^\dagger}{\left|\hat{\boldsymbol{E}}_n\right|^2}. \tag{2.31}$$

Note that, at small electric field strengths, the contrast becomes large. Therefore, instead of the least squares approach, a similar updating scheme for the contrast source could be used [35]. However, this approach is more complex, increasing the computation time. Hence, this thesis uses the least squares method to keep the computational time reasonable.

2.2.5. Updating the receive phase

The last variable that is updated is the receive phase. Therefore, the receive field is determined by first computing the scattered receive field. The scattered field can be determined with

$$\hat{B}_1^{-;sca}(\boldsymbol{r}) = -\frac{\omega}{c_0^2} \partial^- \hat{\boldsymbol{A}}^{sca}(\boldsymbol{r}), \tag{2.32}$$

where $\partial^- = \frac{1}{2}(\partial_x - j\partial_y)$ is the Wirtinger derivative for the receive field. The total transmit field is then obtained by $\hat{B}_1^- = \hat{B}_1^{-;inc} + \hat{B}_1^{-;sca}$. Lastly, the receive phase is determined by

$$\varphi_n^- = \angle(\hat{B}_{1;n}^-). \tag{2.33}$$

A summary of the 2D-CSI is shown in Algorithm 1. Note that additional regularisation often improves the CSI algorithm, such as the multiplicative regularisation with a total variation factor [31]. However, this thesis does not implement regularisation, so the focus is on the proposed adjustment.

2.2.6. Weakened Green's function

One last important remark: Green's function, as described in Equation 2.14, has a logarithmic singularity at zero [36]. In EPT, the source and object domain overlap, and therefore, it is possible that $\boldsymbol{r} - \boldsymbol{r}'$ vanishes. Hence, the Green's function is adjusted to handle this situation, introducing the weakened Green's function. First, a small circular area $\mathbb{A}^{circ}$ around the origin is implemented with a radius

$a = \frac{1}{2}\min\{\Delta x, \Delta y\}$ where Δx and Δy are the resolution in the x and y direction respectively. The weakened Green's function outside this circle is defined as

$$\hat{G}^W(\boldsymbol{r}) = -\frac{j}{2k_0 a} J_1(k_0 a) H_0^{(2)}(k_0|\boldsymbol{r}|), \tag{2.34}$$

where $J_1(\cdot)$ is the first-order Bessel function of the first kind [36]. This weakened Green's function is still very similar to the original Green's function, but only with a factor difference. Furthermore, the weakened Green's function at the origin is now defined as

$$\hat{G}^W(\mathbf{0}) = -\frac{j}{2k_0 a}\left[H_1^{(2)}(k_0 a) - \frac{2j}{\pi k_0 a}\right], \tag{2.35}$$

where $H_1^{(2)}(\cdot)$ is the Hankel function of first-order second kind. Using the weakened Green's function, the scattered action potential becomes

$$\hat{\boldsymbol{A}}^{sca}(\boldsymbol{r}) = \int_{\boldsymbol{r}' \in \mathbb{A}} \hat{G}^W(\boldsymbol{r} - \boldsymbol{r}')\hat{\boldsymbol{w}}(\boldsymbol{r}')dS. \tag{2.36}$$

2.3. Helmholtz Electrical Property Tomography algorithm

A simpler HEPT method is also implemented to compare these reconstructions with the 2D-CSI reconstructions. The first time the EPT algorithm was implemented was in 1991 by Haacke et al. [37]. Many papers have used this algorithm due to the simplicity and short time the algorithm takes [13, 17, 9, 12, 5, 16]. To obtain the HEPT equations, the two Maxwell Equations 2.9 and 2.10 are combined by first taking the curl of Equation 2.9. This results in

$$-\nabla \times \nabla \times \hat{\boldsymbol{B}} + \mu_0 \nabla \times (\hat{\eta}\hat{\boldsymbol{E}}) = \mathbf{0}. \tag{2.37}$$

The next step is to apply the identities $\nabla \times \nabla \times \hat{\boldsymbol{B}} = \nabla\nabla \cdot \hat{\boldsymbol{B}} - \nabla^2 \hat{\boldsymbol{B}}$ and $\nabla \times (\hat{\eta}\hat{\boldsymbol{E}}) = \nabla\hat{\eta} \times \hat{\boldsymbol{E}} + \hat{\eta}\nabla \times \hat{\boldsymbol{E}}$. Therefore, Equation 2.37 can be rewritten to

$$-\nabla\nabla \cdot \hat{\boldsymbol{B}} + \nabla^2 \hat{\boldsymbol{B}} + \mu_0 \nabla\hat{\eta} \times \hat{\boldsymbol{E}} + \mu_0 \hat{\eta}\nabla \times \hat{\boldsymbol{E}} = \mathbf{0}. \tag{2.38}$$

The equation above still includes both the electric and magnetic fields. Fortunately, from Equation 2.10, it is known that $\nabla \times \hat{\boldsymbol{E}} = -j\omega\hat{\boldsymbol{B}}$ and Equation 2.9 shows that $\hat{\boldsymbol{E}} = \frac{1}{\hat{\eta}\mu_0}\nabla \times \hat{\boldsymbol{B}}$. Hence, the electric field in Equation 2.38 can be substituted by the equations as mentioned earlier, resulting in

$$-\nabla\nabla \cdot \hat{\boldsymbol{B}} + \nabla^2 \hat{\boldsymbol{B}} + \frac{\nabla\hat{\eta}}{\hat{\eta}} \times (\nabla \times \hat{\boldsymbol{B}}) - j\omega\mu_0 \hat{\eta}\hat{\boldsymbol{B}} = \mathbf{0}. \tag{2.39}$$

The first term vanishes as the divergence of Equation 2.10 is $\nabla \cdot (\nabla \times \hat{\boldsymbol{E}}) + j\omega\nabla \cdot \hat{\boldsymbol{B}} = 0$ and the divergence of the curl is always zero. Therefore, $\nabla \cdot \hat{\boldsymbol{B}}$ must be zero as well. Furthermore, in HEPT, a homogeneous medium is assumed, resulting in $\nabla\hat{\eta} = \mathbf{0}$. Equation 2.39 can be simplified to

$$\nabla^2 \hat{\boldsymbol{B}} - j\omega\mu_0 \hat{\eta}\hat{\boldsymbol{B}} = \mathbf{0}. \tag{2.40}$$

The magnetic field can be converted to the transmit field by taking the inner product of Equation 2.40 and $\mathbf{i}^+ = \frac{1}{2}(\mathbf{i}_x + j\mathbf{i}_y)$. Consequently,

$$\nabla^2 \hat{B}_1^+ - j\omega\mu_0 \hat{\eta}\hat{B}_1^+ = 0. \tag{2.41}$$

Moreover, the formula for the admittance can be substituted, and the terms can be reordered to

$$\frac{\nabla^2 \hat{B}_1^+}{\hat{B}_1^+} = j\omega\mu_0(\sigma + j\omega\epsilon_0\epsilon_r). \tag{2.42}$$

The conductivity is included in the imaginary part, while the relative permittivity is included in the real part of the transmit field. Hence, the conductivity can be found using

$$\sigma = \frac{1}{\omega\mu_0}\Im\left(\frac{\nabla^2 \hat{B}_1^+}{\hat{B}_1^+}\right), \tag{2.43}$$

Algorithm 2 HEPT algorithm

Calculate $\sigma = \frac{1}{\omega\mu_0}\Im\left(\frac{\nabla^2\hat{B}_1^+}{\hat{B}_1^+}\right)$
Calculate $\epsilon_r = \frac{-1}{\omega^2\mu_0\epsilon_0}\Re\left(\frac{\nabla^2\hat{B}_1^+}{\hat{B}_1^+}\right)$
Gaussian filter over σ and ϵ_r
if $\sigma(\boldsymbol{r}) > \text{mean}\{\sigma(\boldsymbol{r})\} + 3 * \text{std}\{\sigma(\boldsymbol{r})\}$ **then**
    $\sigma(\boldsymbol{r}) = \text{mean}\{\sigma(\boldsymbol{r})\} + 3 * \text{std}\{\sigma(\boldsymbol{r})\}$
if $\epsilon_r(\boldsymbol{r}) > \text{mean}\{\epsilon_r(\boldsymbol{r})\} + 3 * \text{std}\{\epsilon_r(\boldsymbol{r})\}$ **then**
    $\epsilon_r(\boldsymbol{r}) = \text{mean}\{\epsilon_r(\boldsymbol{r})\} + 3 * \text{std}\{\epsilon_r(\boldsymbol{r})\}$

and the relative permittivity

$$\epsilon_r = \frac{-1}{\omega^2\mu_0\epsilon_0}\Re\left(\frac{\nabla^2\hat{B}_1^+}{\hat{B}_1^+}\right). \tag{2.44}$$

The Laplacian of the transmit field results in boundary issues as the sharp edges between different tissue areas result in data amplification at the boundaries. Moreover, if noise is present, the HEPT reconstructions become noisy as the noise intensity is heightened due to the spatial differentiation of the data. A spatial Gaussian filter is applied to the reconstructions to mitigate these problems. Moreover, upper limits are implemented to prevent the algorithm from exceeding far above realistic values. The upper limits are set to $mean\{\sigma(\boldsymbol{r})\} + 3 * std\{\sigma(\boldsymbol{r})\}$, and $mean\{\epsilon_r(\boldsymbol{r})\} + 3 * std\{\epsilon_r(\boldsymbol{r})\}$ for the conductivity and relative permittivity, respectively [38]. If these values are exceeded in any pixel, the algorithm sets the pixel equal to the limit. A summary of the HEPT implementation is provided in Algorithm 2.

3

Performance of 2D-CSI on the 2D Ella dataset

This chapter investigates multiple enhancements on a 2D dataset to make the CSI algorithm more robust and better at handling 3D data. First, an explanation of the creation of the 2D dataset is provided. Afterwards, the effect of early stopping on the image quality is considered. Subsequently, the inclusion of a positivity constraint is discussed. The chapter ends with a small investigation of the effect of the chosen initialisation.

3.1. Create dataset

The Ella body model from the virtual family [15] includes tissue information of a 26-year-old female and is used to create the 2D dataset. From the body model, three different slices are chosen (Figure 3.1). Throughout this thesis, the focus is on the head (slice 320), while the legs (slice 55) and pelvis (slice 168) are discussed in Appendix B. Figure 3.2 shows the 2D conductivity and relative permittivity map corresponding to the head slice (these values correspond to EP values measured at $3\ T$). The EPs are discretised using a square meshing with a mesh size of $2.5\ mm$, resulting in images of 120×212 pixels.

3.1.1. Incident fields

The incident and scattered fields are created first to determine the total fields. The incident fields are simulated in an empty bird cage coil with 16 legs. The legs inside the bird cage coil are modelled as 16 equally spaced infinite long wires on a circle with a radius of $R_A = 0.352\ m$. In the middle of a birdcage coil, the legs can indeed be assumed to be infinitely long lines, as, at this location, the edge effect of the coil is negligible. Furthermore, it is necessary to implement an RF shield as this removes external RF fields [14]. This RF shield is modelled with 16 mirror sources spread evenly on a circle at a distance of

$$d = \frac{R_S^2}{R_A}, \tag{3.1}$$

where $R_s = 0.3715\ m$ is the RF shield radius [39, 14]. These mirror sources are also assumed to be infinite long wires, but the current is going in the opposite direction. Figure 3.3 shows the empty coil with all distances. Moreover, a parameter θ is introduced, showing the MR machine's phase offset. This offset affects the phase of the simulated incident fields. The incident fields can be calculated similarly as in Equation 2.12 but with an external vector potential instead of the scattered vector potential. Hence, the incident fields are defined as

$$\hat{B}_1^{+;inc}(\boldsymbol{r}) = \frac{\omega}{c_0^2}\partial^+ \hat{\boldsymbol{A}}^{ext}(\boldsymbol{r}),\ \hat{B}_1^{-;inc}(\boldsymbol{r}) = -\frac{\omega}{c_0^2}\partial^- \hat{\boldsymbol{A}}^{ext}(\boldsymbol{r}),\ \text{and}\ \hat{\boldsymbol{E}}^{inc}(\boldsymbol{r}) = k_0^2 \hat{\boldsymbol{A}}^{ext}(\boldsymbol{r}), \tag{3.2}$$

where the external vector potential becomes

$$\hat{\boldsymbol{A}}^{ext}(\boldsymbol{r}) = \frac{1}{j\omega\epsilon_0}\int_{\boldsymbol{r}'\in\mathbb{A}} \hat{G}(\boldsymbol{r}-\boldsymbol{r}')\hat{\boldsymbol{J}}^{ext}(\boldsymbol{r}')dS. \tag{3.3}$$

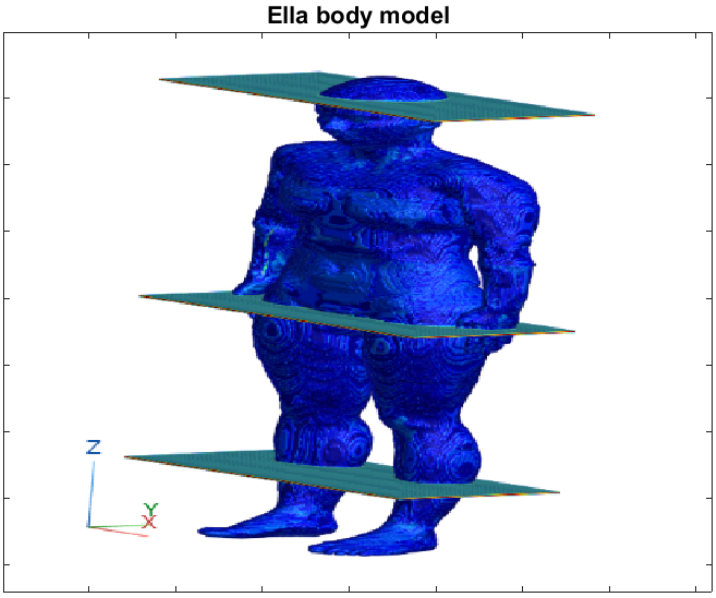

Figure 3.1: 3D image of the Ella body with the planes of interest shown. From bottom to top, slices 55, 168, and 320 show the legs, pelvis and head, respectively.

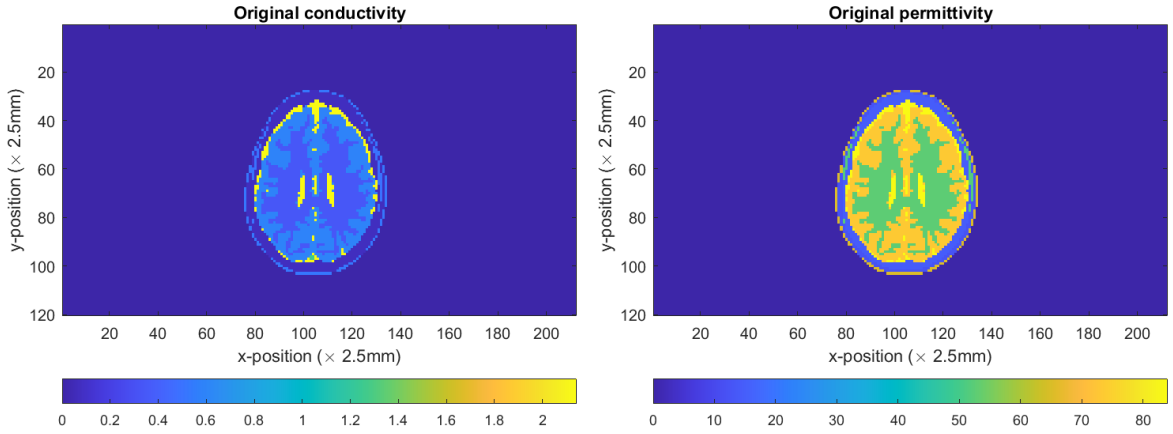

(a) Conductivity **(b)** Relative permittivity

Figure 3.2: The conductivity and relative permittivity of slice 320 as provided in the Ella dataset.

The external current $\hat{\boldsymbol{J}}^{ext}$ can be modelled as a positive delta at the location of the legs and a negative delta at the position of the mirror sources. These deltas should be multiplied by a magnitude factor, representing the inserted power, and a phase factor, due to the operating mode of the MR machine. The deltas make it possible to reduce integrals to sums. Moreover, the Green's function is no longer zero as the sources are outside the imaging domain, making using the normal Green's function possible. Therefore, the external vector potential can be described as

$$\hat{\boldsymbol{A}}^{ext}(\boldsymbol{r}) = \frac{1}{4\omega\epsilon_0} \sum_{n=1}^{N} e^{j(\phi_n+\theta)} \left[-H_0^{(2)}(k_0|\boldsymbol{r} - \boldsymbol{r}_{A;n}|) + H_0^{(2)}(k_0|\boldsymbol{r} - \boldsymbol{r}_{M;n}|) \right], \tag{3.4}$$

where N is the number of legs, $e^{j(\phi_n+\theta)}$ is the quadrature mode term, and $\boldsymbol{r}_{A;n}$ and $\boldsymbol{r}_{M;n}$ are the antenna locations and mirror sources for the n-th leg respectively. The phase $\phi_n = \frac{2\pi}{N}(n-1)$ is used to determine these locations, namely

$$\boldsymbol{r}_{\xi;n} = R_\xi \begin{bmatrix} \cos(\phi_n) \\ \sin(\phi_n) \end{bmatrix}, \tag{3.5}$$

where ξ represents either the antenna locations (A) or the mirror source location (M). Applying this external vector potential to Equation 3.2 results in the incident electric, transmit, and receive field in Figure 3.4, 3.5, and 3.6 respectively. The magnitude of these incident fields indeed corresponds to fields in quadrature mode [32]. For the phase figures, note that the sharp edges are at locations where one side is $-\pi$ and the other side π, which are values very close to each other, so the phases show smooth patterns.

3.1.2. Total electric field

The simulated incident electric field is necessary to create the total electric field. The total electric field is found with the Generalized Minimal Residual (GMRES) method [40]. GMRES's outcome consists of a vector that minimises an error in a defined residual. In this case, the minimization problem becomes

$$\hat{\boldsymbol{E}}^{tot} = \min_{E} \left\| E - \mathcal{G}_E\{\hat{\chi} E\} - \hat{\boldsymbol{E}}^{inc} \right\|_2, \tag{3.6}$$

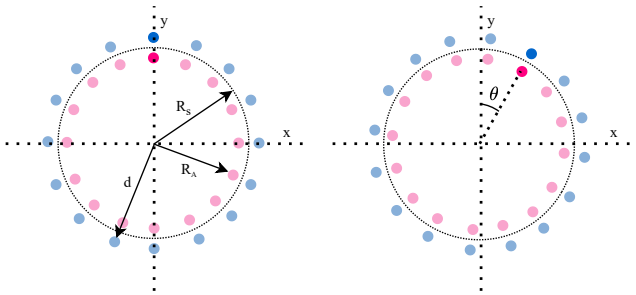

Figure 3.3: Schematic of the birdcage coil without (left) and with (right) an offset θ. The pink and blue circles indicate the coil legs and mirror sources. Moreover, the darker circle represents the main legs. The dotted circle is the RF-shield location.

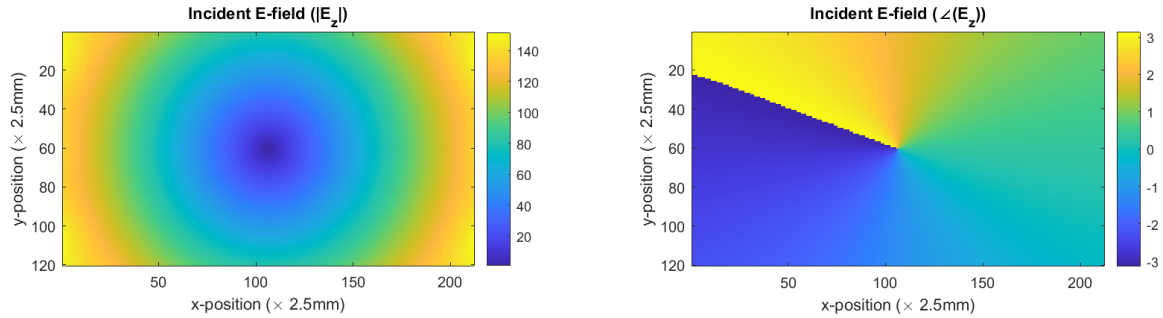

Figure 3.4: The electric incident field with the magnitude on the left and the phase on the right with an offset $\theta = 0°$

.

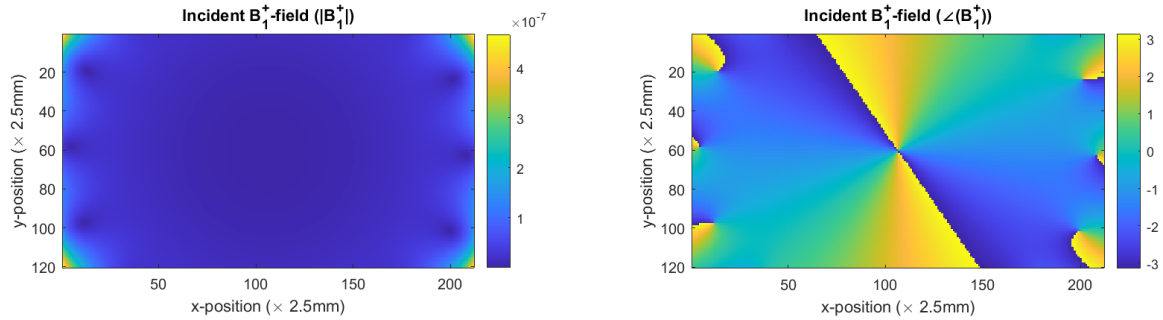

Figure 3.5: The incident transmit field with the magnitude on the left and the phase on the right with an offset $\theta = 0°$

.

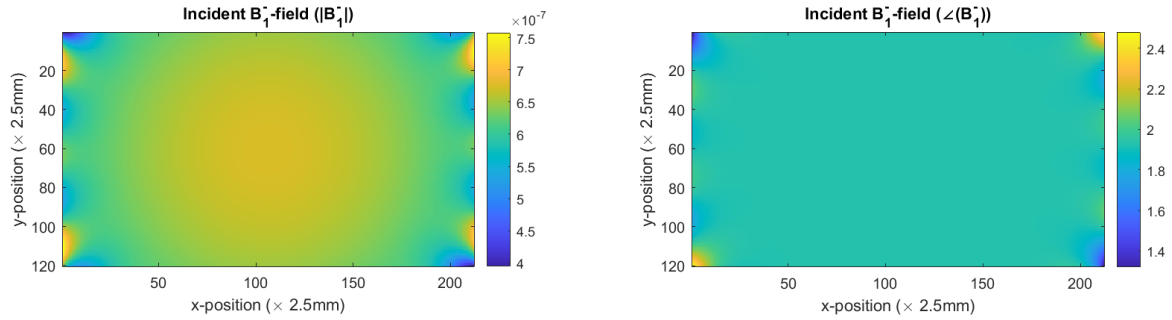

Figure 3.6: The incident receive field with the magnitude on the left and the phase on the right with an offset $\theta = 0°$

.

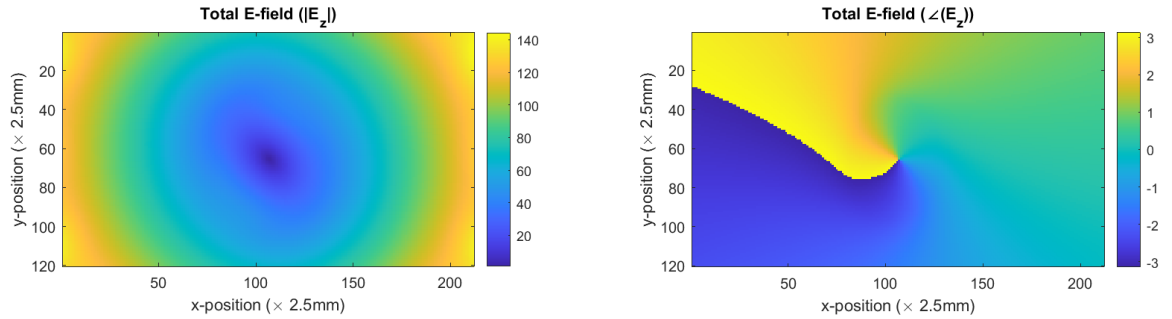

Figure 3.7: The total electric field with the magnitude on the left and the phase on the right with an offset $\theta = 0°$

.

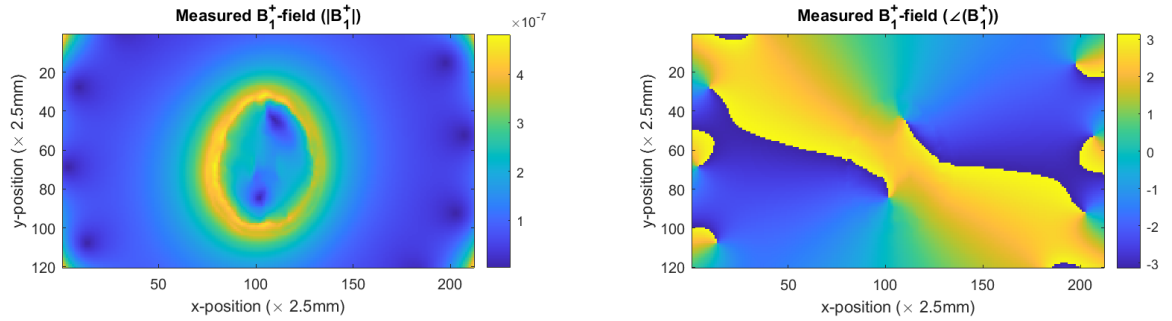

Figure 3.8: The total transmit field with the magnitude on the left and the phase on the right with an offset $\theta = 0°$

.

where r_E is the residual of the electric field as defined in Equation 2.29 with the contrast source written in components as defined in Equation 2.15. Figure 3.7 provides the total electric field. The magnitude of the total electric field is no longer a perfect circle; instead, the EPs are imprinted. The phase is also adjusted, as the clear lines in the incident field now show a wavy pattern. This suggests that the GMRES method can indeed be used to create the electric field.

3.1.3. Creation of other variables

When the electric field is known, the contrast source is calculated with Equation 2.15. The contrast source is then inserted in the scatter field Equations 2.12 and 2.32 to create the scattered transmit and receive field. Lastly, the scattered transmit and receive fields are combined with the incident transmit and receive fields to determine the total transmit and receive fields. Figure 3.8, and 3.9 provide these total transmit and receive fields. In these images, it is possible to see the outline of the head, which suggests that the contrast has affected the transmit and receive fields. The creation of the Ella dataset is summarised in Figure 3.10.

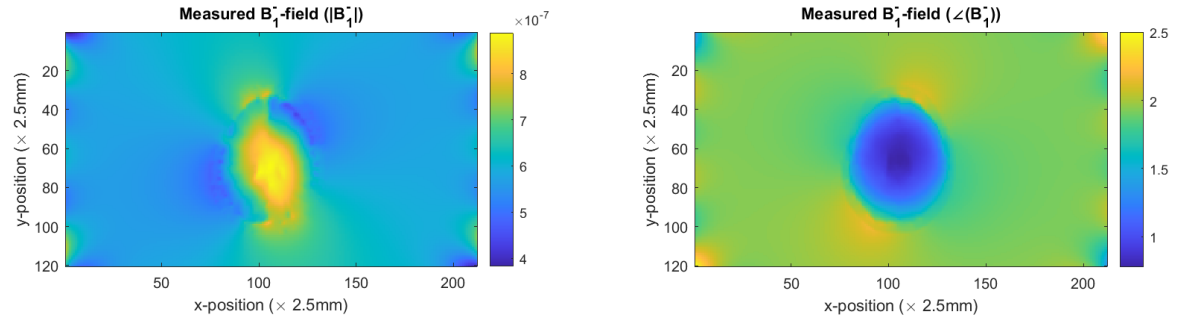

Figure 3.9: The total receive field with the magnitude on the left and the phase on the right with an offset $\theta = 0°$

.

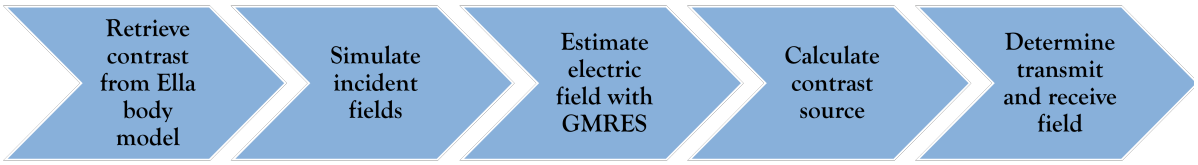

Figure 3.10: An overview of the process used to create the Ella dataset.

3.2. Experiments

This section starts with the introduction of multiple adjustments, and afterwards, a robustness analysis is performed, but before discussing multiple improvements, the algorithm is first run without enhancements and with the following parameters:

- Maximum number of iterations: 1000
- Tolerance: $1e-6$
- Update receive phase: on
- Multiplicative regularisation: off
- Data: 2D

The bottom of Figure 3.11 shows the reconstruction after 1000 iterations. When the reconstructions are compared to the original, the conductivity is close to the original except for small deviations on the antidiagonal and at boundaries. On the other hand, the relative permittivity has large errors on the antidiagonal and at boundaries. These larger errors for the relative permittivity compared to the conductivity can originate from the fact that at $3\ T$, the displacement current is relatively small compared to the conduction current, where the displacement current is proportional to the relative permittivity and the conduction current to the conductivity.

Furthermore, the antidiagonal and boundaries are most affected as the TPA fails at those locations. Therefore, it is important to investigate adjustments to the algorithm to mitigate these effects. Moreover, seeing if the results are better at another iteration is interesting. Hence, the first proposed improvement is an implementation of early stopping. Leijsen has mentioned that iterating too far results in the algorithm modelling error sources and so reaching worse reconstructions [31].

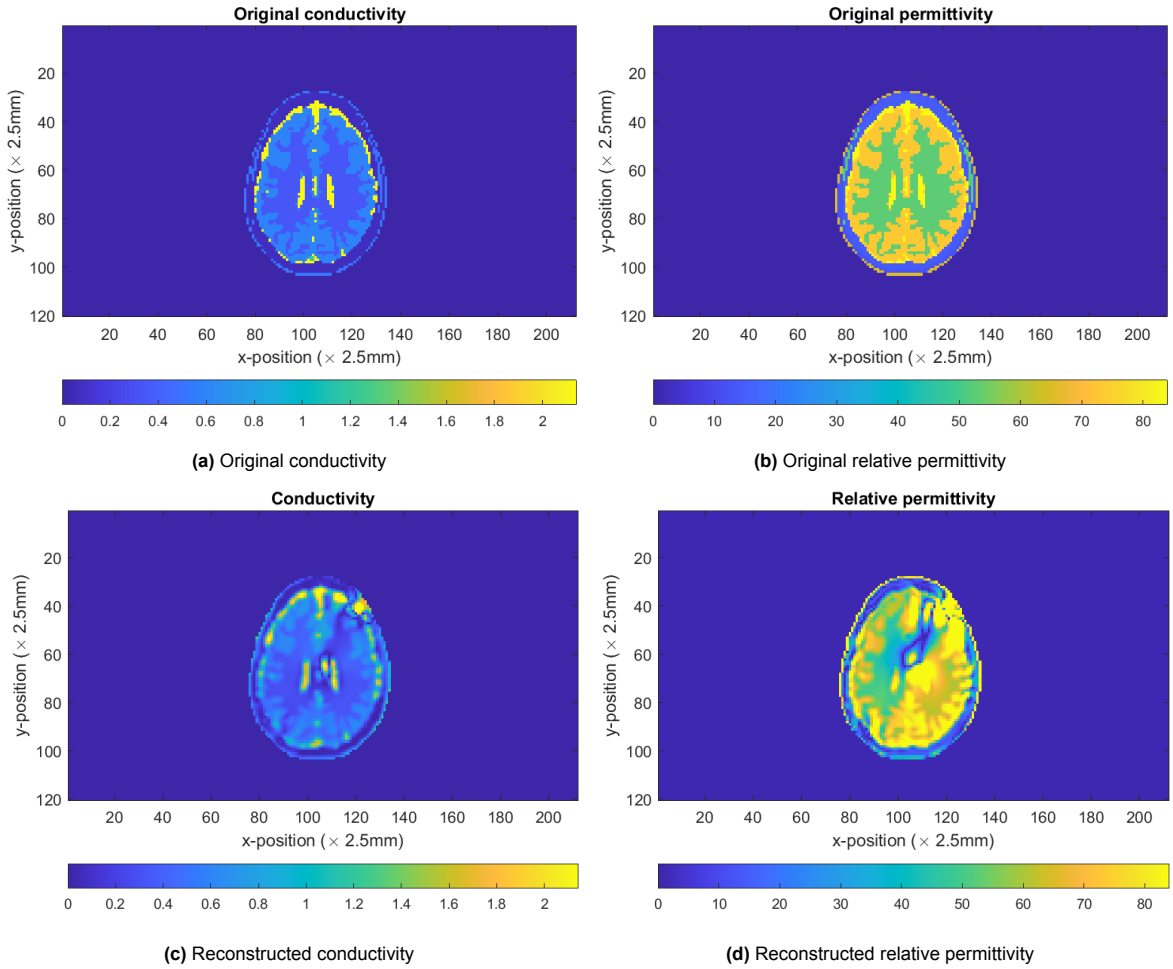

(a) Original conductivity

(b) Original relative permittivity

(c) Reconstructed conductivity

(d) Reconstructed relative permittivity

Figure 3.11: The conductivity (a, c) and relative permittivity (b, d) of slice 320 with on the top the original EPs and at the bottom the result after applying the CSI algorithm at the 1000th iteration.

3.2.1. Early stopping

As eyeballing the reconstructions at each iteration is unrealistic, it has been decided to look at three performance metrics instead. The first is the magnitude of the cost function at each iteration. The mean squared error between the original and reconstructed conductivity is calculated. The last metric is the mean squared error between the original and reconstructed relative permittivity. Note that the first metric can always be taken while the others can only be used when the ground truth is available. Figure 3.12 shows the results at each iteration. The cost functional first drops, and after 346 iterations, it increases again. On the other hand, the conductivity error has a minimum at the 677th iteration. The relative permittivity error first increases and then has a steep decrease until iteration 76 and afterwards increases slowly again.

Figure 3.13 provides the reconstructions at the different minima. The reconstruction of the 76th iteration is hardly interpretable, as everything is blurred. The lower relative permittivity error in the early iterations can be explained by the algorithm converging away from the ground truth in some pixels after more iterations. Since the difference for each point counts equally, these pixels increase the error substantially while the reconstruction becomes better interpretable. More specifically, in the beginning, the boundary is still captured correctly, but later on, parts of the boundary converge to zero. Despite the increase in error, the readability of the relative permittivity at iterations 346 and 677 is better. When the 346th iteration is compared to the 677th iteration, it can be seen that the second is a sharper version of the first. Furthermore, the EPs of the 346th iteration have fewer gaps in the reconstruction at the edges, which makes this reconstruction better. Lastly, when comparing the final reconstruction

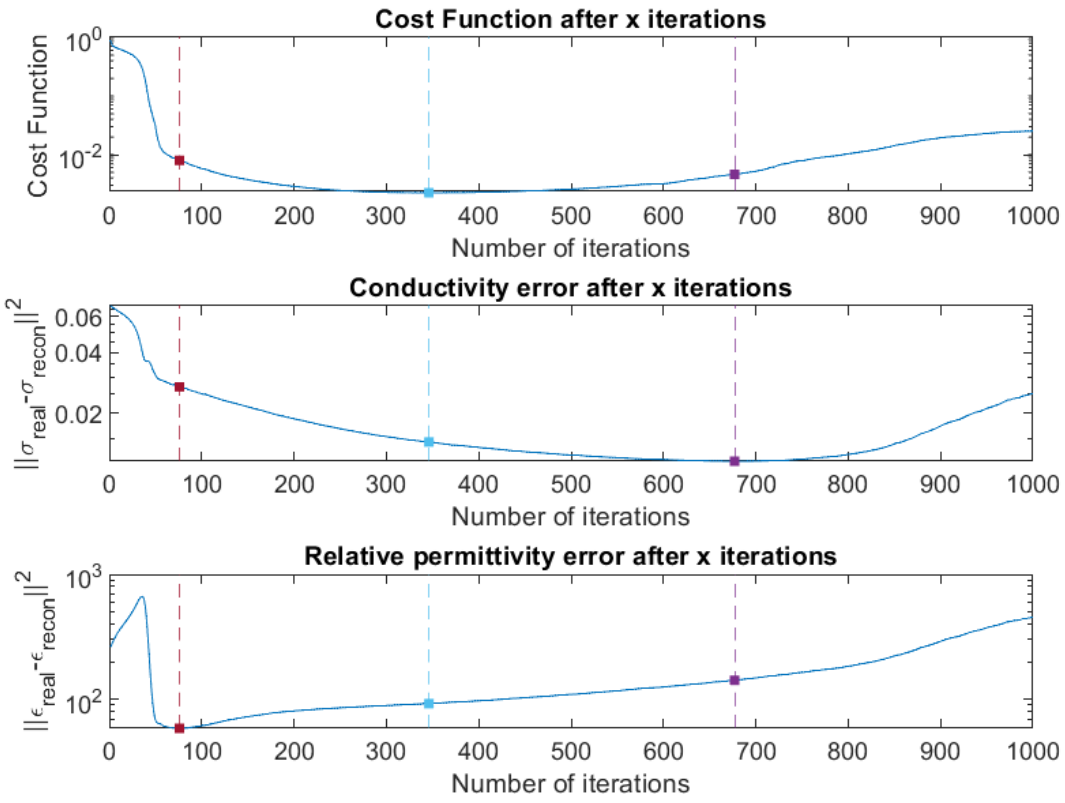

Figure 3.12: The algorithm's performance for slice 320 over different iterations measured using the cost function magnitude, the mean squared error of both the conductivity and the relative permittivity. The light blue, purple, and red vertical lines represent the iterations with the lowest cost functional, conductivity error, and relative permittivity error, respectively.

and the reconstruction at iteration 346, the latter is closer to the original, especially for the relative permittivity. Therefore, the reconstruction at the minimum of the cost functional is a reasonable option for an early stopping mechanism, this effect was even more clearly seen in Appendix B. Additionally, the early stopping can increase the speed of the algorithm. However, there are still some errors in the reconstruction. Therefore, a second proposed enhancement is the addition of a positivity constraint for both the conductivity and relative permittivity.

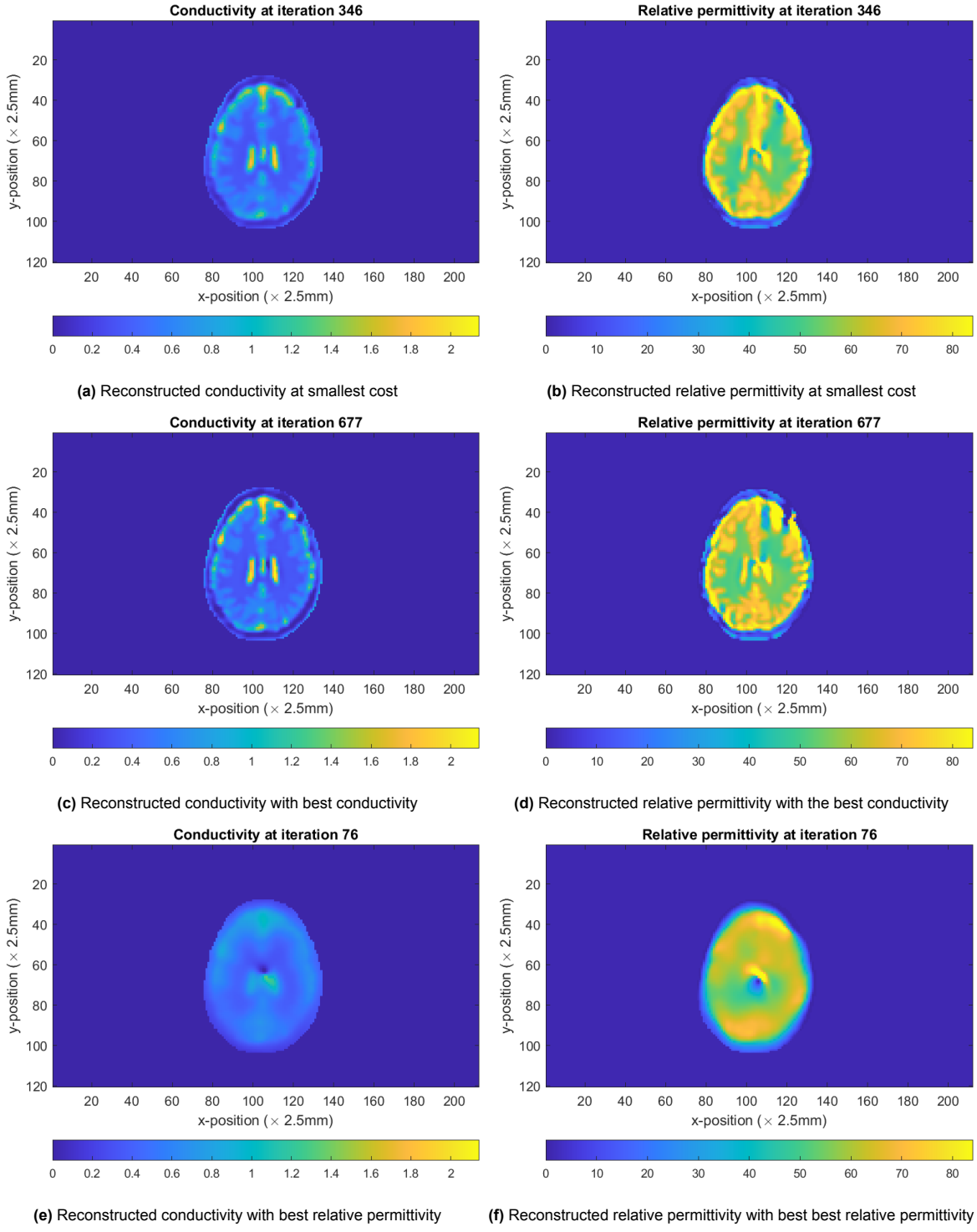

(a) Reconstructed conductivity at smallest cost

(b) Reconstructed relative permittivity at smallest cost

(c) Reconstructed conductivity with best conductivity

(d) Reconstructed relative permittivity with the best conductivity

(e) Reconstructed conductivity with best relative permittivity

(f) Reconstructed relative permittivity with best best relative permittivity

Figure 3.13: The conductivity (a, c, e) and relative permittivity (b, d, f) of slice 320, where the upper, middle and bottom rows show the reconstructions at the minima of the cost functional, conductivity error and relative permittivity error, respectively.

3.2.2. Positivity constraint

It is physically known that both the conductivity and the relative permittivity should be positive, which could be implemented in the algorithm. However, as the CSI algorithm does not directly depend on conductivity and relative permittivity, this constraint is implemented in the contrast function update. Therefore, Equation 2.16 needs to be revised. The real part depends on the relative permittivity, and the imaginary part depends on the conductivity. Hence, the positivity constraint can be implemented

by verifying these two conditions:

1. $\Re\{\chi(\boldsymbol{r})\} + 1 \geq 0$,
2. $\Im\{\chi(\boldsymbol{r})\} \leq 0$,

where $\chi(\boldsymbol{r})$ is the contrast function at position $\boldsymbol{r}$. If these conditions fail for any position at any iteration, the contrast function is brought back to the Hilbert space through the following rules:

1. $\chi_{new}(\boldsymbol{r}) = -\Re\{\chi_{old}(\boldsymbol{r})\} + j\Im\{\chi_{old}(\boldsymbol{r})\}$,
2. $\chi_{new}(\boldsymbol{r}) = \Re\{\chi_{old}(\boldsymbol{r})\} - j\Im\{\chi_{old}(\boldsymbol{r})\}$.

Note that, in this case, the sign of the contrast function part which fails the condition is flipped. Figure 3.14 shows the reconstructions with implemented positivity constraint. The reconstructions are very close to the original. Moreover, the difference between the final reconstruction at iteration 1000 and the 993th iteration cannot be seen. Therefore, the 993 iteration reconstruction could minimally decrease the computational time. When the positivity constraint is applied, the reconstruction has improved much compared to the final reconstruction in Figure 3.11. More specifically, the previously noted problems with the diagonal and in the middle are reduced. Lastly, when studying the differences between the 346 slice (Figure 3.13) without positivity and the reconstructions with positivity, the image is less blurred in the second case, and the permittivity is reconstructed better around the diagonal. Hence, these results show that the positivity constraint helps to avoid some issues due to the failing TPA. This behaviour was also observed for the pelvis slice in Appendix B.

Instead of flipping the sign of the real and imaginary part, the conductivity and relative permittivity can be set to zero when the condition fails. This zero implementation is investigated in Appendix A. It can be seen that the reconstructions for the head slice and the different implementations of the positivity constraint are very close to each other. Moreover, the results were similar in the pelvis slice (not provided). Further on, as there is not a clear advantage for the zero implementation, the sign flip implementation is used as it is known that the EPs are larger than zero in the body.

The last adjustment which is considered is choosing a different initialisation. Leijsen mentioned that the initialisation could significantly impact the reconstructions [31].

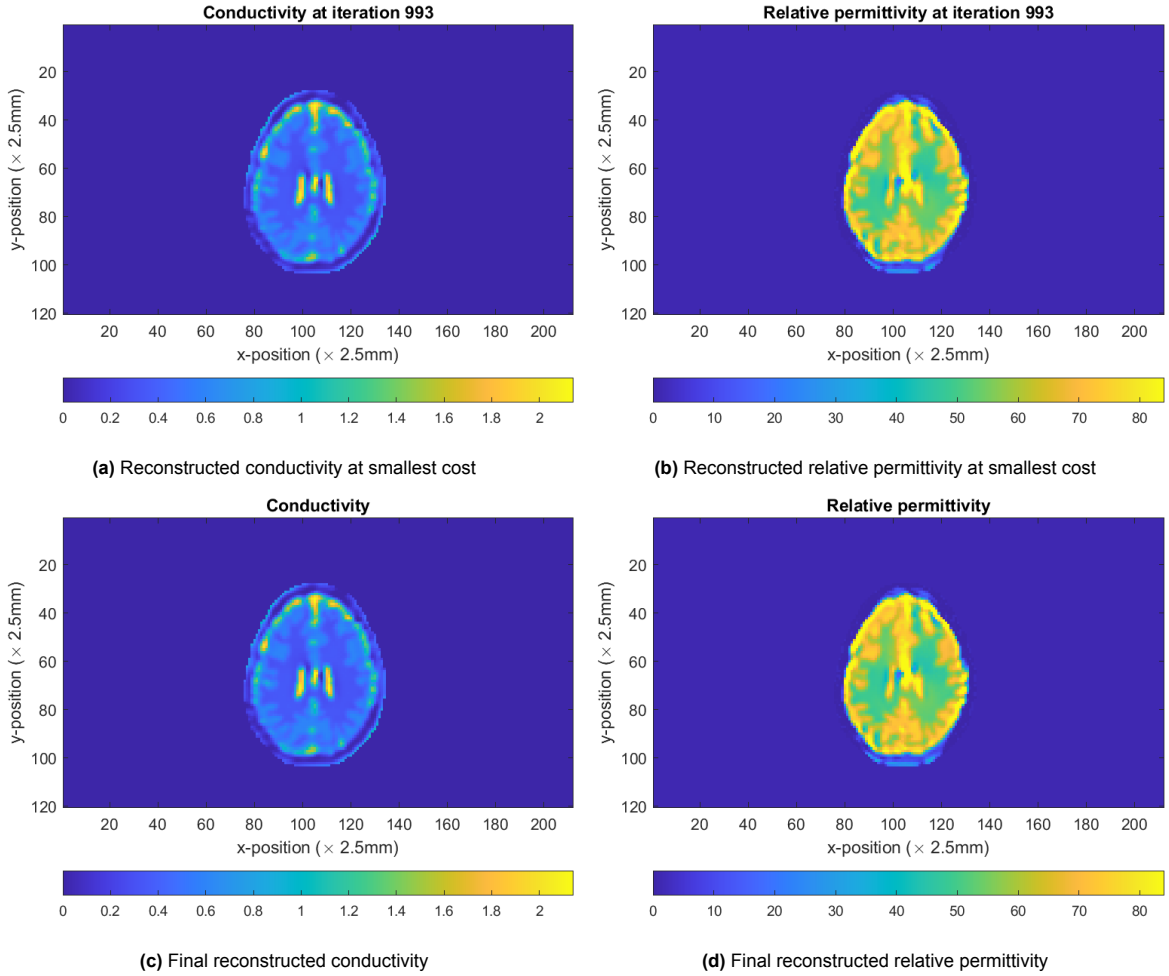

(a) Reconstructed conductivity at smallest cost

(b) Reconstructed relative permittivity at smallest cost

(c) Final reconstructed conductivity

(d) Final reconstructed relative permittivity

Figure 3.14: The conductivity (a, c) and relative permittivity (b, d) of slice 320 with the positivity constraint implemented. The upper row shows the reconstruction at the iteration with the minimum cost functional, and the bottom row shows the final reconstruction.

3.2.3. Initialisation

The other proposed initialisation is to calculate the contrast function using the reconstructions from HEPT. Figure 3.15 provides the reconstructions with HEPT initialisation. The reconstructions after the first iteration are difficult to interpret because of the fine structures inside the head. The HEPT algorithm has difficulties as it amplifies the values at these edges. If the iterations progress, the reconstruction improves, and at the 980th iteration, the cost function is minimal. The resulting reconstructions include most details from the original EPs, but the boundaries are not very sharp, and the different tissue areas are not smooth, which increases the difficulty of interpreting the reconstructions correctly. When comparing the reconstructions with HEPT and the reconstructions with back projection initialisation (Figure 3.14), using HEPT does not speed up the algorithm in the head slice. Moreover, the images with back projection are better around the boundaries and are smoother in the different tissue areas. If noise is added to the fields, the reconstruction of HEPT is even worse as the field is differentiated twice, so the noise gets amplified. Therefore, with the HEPT initialisation, the algorithm has even more problems finding the actual data than the backpropagation initialisation. Hence, it is decided to use backpropagation throughout the rest of the thesis.

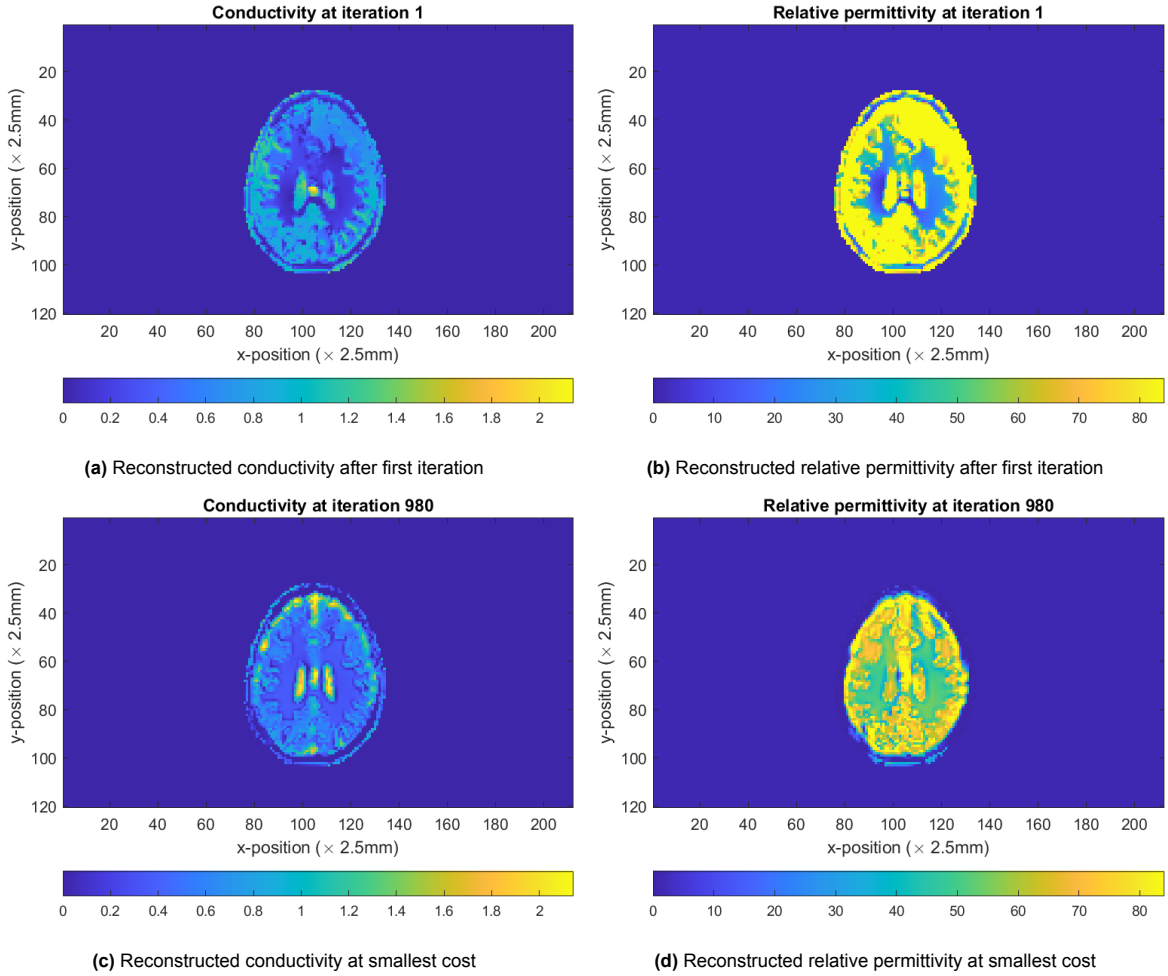

(a) Reconstructed conductivity after first iteration

(b) Reconstructed relative permittivity after first iteration

(c) Reconstructed conductivity at smallest cost

(d) Reconstructed relative permittivity at smallest cost

Figure 3.15: The conductivity (a, c) and relative permittivity (b, d) of slice 320 with HEPT initialisation and positivity constraint implemented. The upper row shows the reconstruction after the first iteration. The bottom row shows the reconstruction at the cost functional minimum.

3.2.4. Robustness analysis

The robustness analysis first considers the effect of a change in offset. Second, the quality of the reconstructions with different noise levels is investigated.

Effect on offset

The data created by an MR machine has an uncertain offset θ. Therefore, the algorithm should be robust even though the wrong offset is chosen for simulating the incident fields. A wrongly chosen offset is simulated by creating the Ella dataset according to Figure 3.10, after which the incident fields are simulated again, but with an offset of 5 degrees. Figure 3.16 shows the 2D-CSI algorithm reconstruction with and without applying the positivity constraint. The conductivity and relative permittivity without positivity constraint at the cost functional minimum are blurred and too inaccurate to be used. When the positivity constraint is applied, the conductivity becomes very accurate except for the outer edge and the centre. The relative permittivity lacks more details at the edge and in the centre than the conductivity but is still better interpretable than the results without the positivity constraint. Hence, adding the positivity constraint makes the model more robust to inaccurately known offsets.

Effect on noise

The data used so far is noiseless. Unfortunately, this is not realistic in a real-life setting. Therefore, the measured data should be distorted by noise. This noise is implemented by adding random values scaled to the Signal-to-Noise Ratio (SNR) to both the magnitude and phase of the transmit and receive field. A realistic SNR value for a 3T MR machine is 54 ($\approx 34.6dB$) [14]. In this thesis, it is decided to

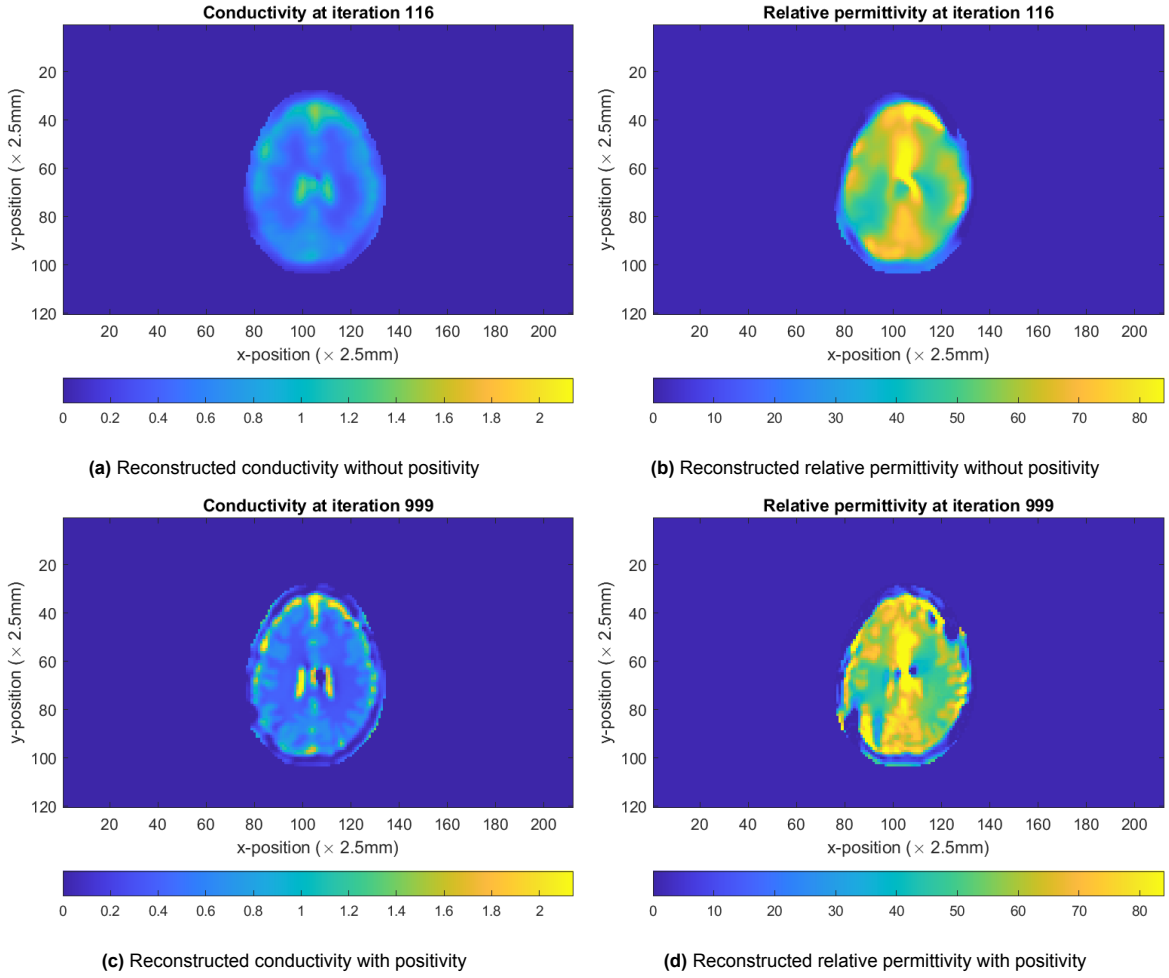

(a) Reconstructed conductivity without positivity

(b) Reconstructed relative permittivity without positivity

(c) Reconstructed conductivity with positivity

(d) Reconstructed relative permittivity with positivity

Figure 3.16: The conductivity (a, c) and relative permittivity (b, d) of slice 320 with an offset difference of 5° between the measured fields and the incident fields at the iteration with the smallest cost function. The upper row shows the reconstructions without positivity constraint, while the bottom shows the reconstruction with positivity constraint.

investigate the reconstruction results for SNRs of 50 ($\approx 34dB$), 100 ($\approx 40dB$), and 150 ($\approx 43.5dB$). After distorting the transmit and receive field, a Gaussian filter is applied in the frequency domain to create smoother, more realistic fields. The reconstructions corresponding to the implementation without and with positivity constraint are seen in Figures 3.17 and 3.18, respectively. As expected, the quality of the reconstructions increases when the SNR increases. Moreover, if the reconstructions with and without a positivity constraint are compared, the reconstructions with a positivity constraint are clearer, but noise is also more present. This behaviour is because the minimum cost function is at a later iteration when the positivity constraint is implemented, so the algorithm has had more iterations to model the noise. Another observation is that the positivity constraint still helps by capturing more details on the outer boundary of the head, especially for the relative permittivity.

3.3. Conclusion

In this chapter, three adjustments to the 2D-CSI algorithm are tested. The early stopping makes the algorithm faster and ensures that the algorithm does not model many data artefacts. Unfortunately, the early stopping can result in less sharp images. Nevertheless, the images still become better interpretable. The advances are not evident in the head slice, but the pelvis slice (in Appendix B) does show large improvements. The larger advances in the pelvis slice originate from this slice being less circular and symmetric. Therefore, the TPA is known to cause larger issues. Early stopping is a useful tool to avoid these problems.

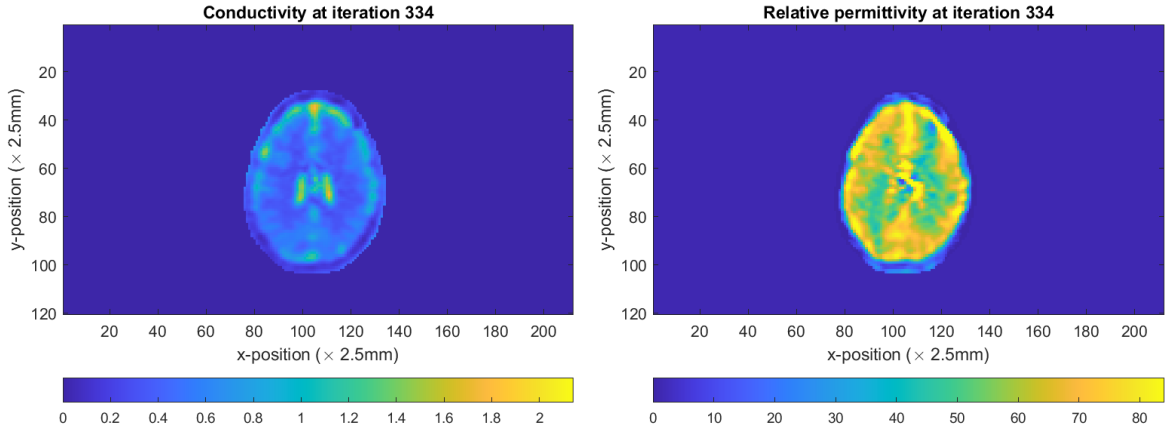

(a) Reconstructed conductivity at SNR 50

(b) Reconstructed relative permittivity at SNR 50

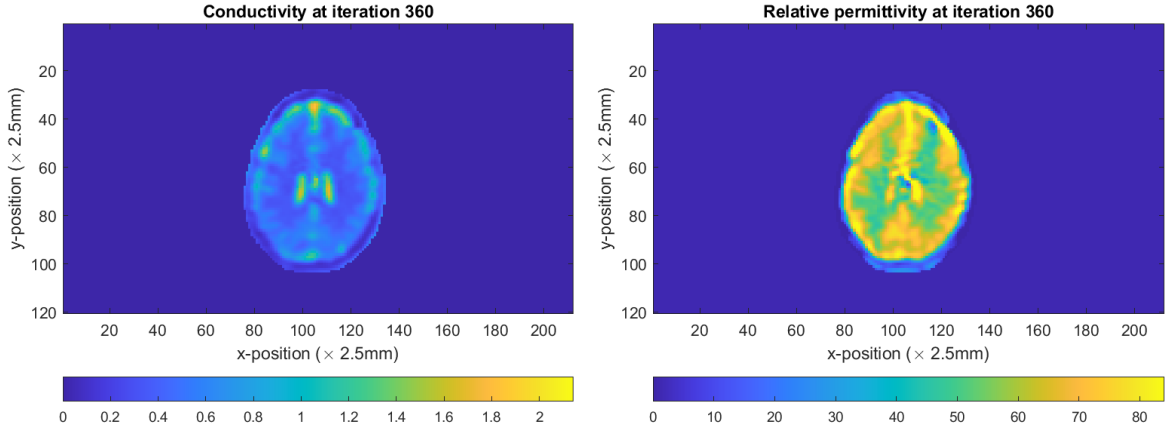

(c) Reconstructed conductivity at SNR 100

(d) Reconstructed relative permittivity at SNR 100

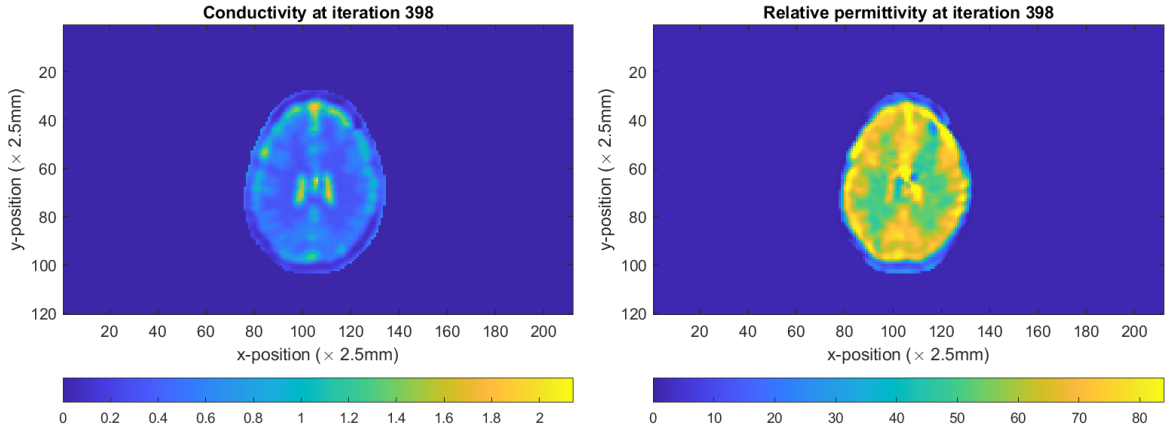

(e) Reconstructed conductivity at SNR 150

(f) Reconstructed relative permittivity at SNR 150

Figure 3.17: The conductivity (a, c, e) and relative permittivity (b, d, f) of slice 320 without the positivity constraint, where the upper, middle and bottom rows show the reconstructions with an SNR of 50, 100 and 150, respectively.

The second improvement is the implementation of a positivity constraint on the conductivity and relative permittivity. The positivity constraints are checked at each iteration, and the contrast is adjusted if a constraint fails. The positivity constraint helps by correctly estimating the receive phase; therefore, the artefacts due to a failing TPA are reduced. Moreover, for the head slice, the reconstructions are sharper and more detailed than before the positivity analysis. Hence, the positivity constraint helps the model to converge to the ground truth. As before, larger advances can be seen in the pelvis in

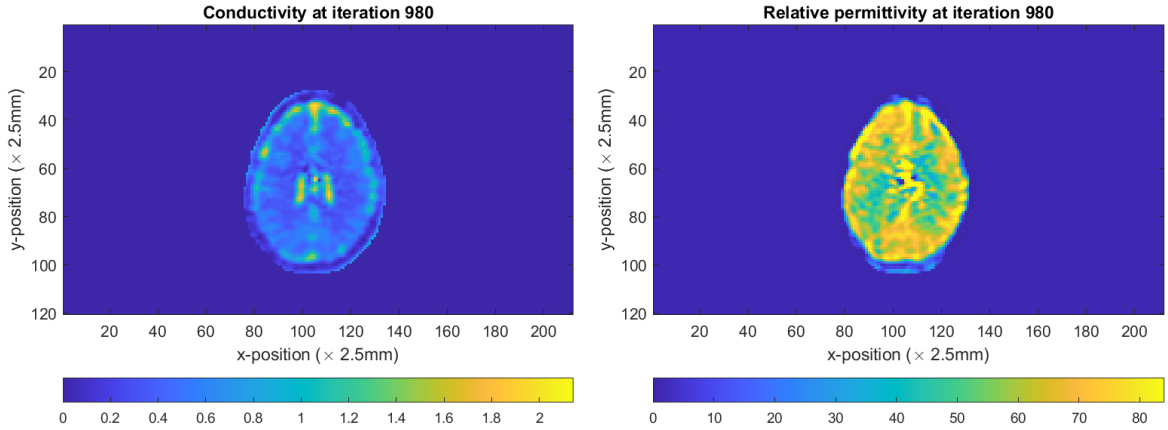

(a) Reconstructed conductivity at SNR 50

(b) Reconstructed relative permittivity at SNR 50

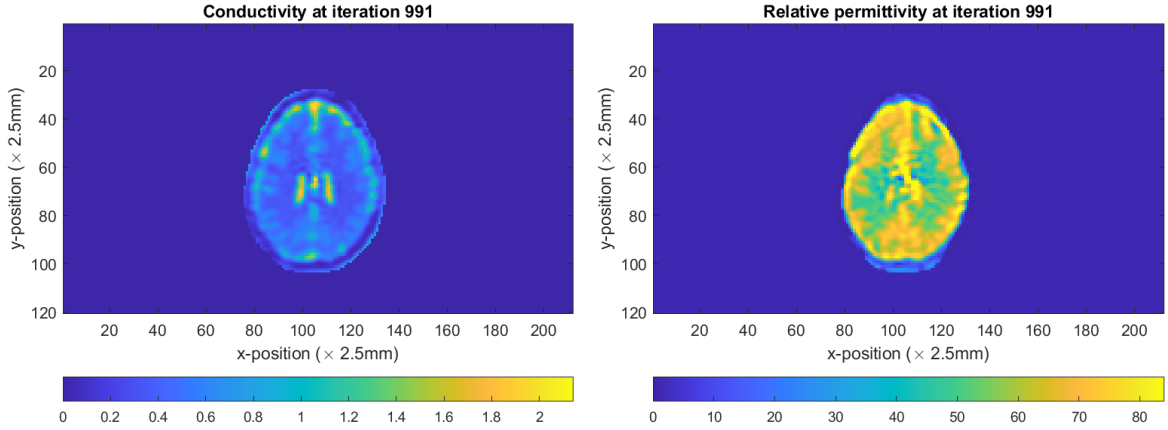

(c) Reconstructed conductivity at SNR 100

(d) Reconstructed relative permittivity at SNR 100

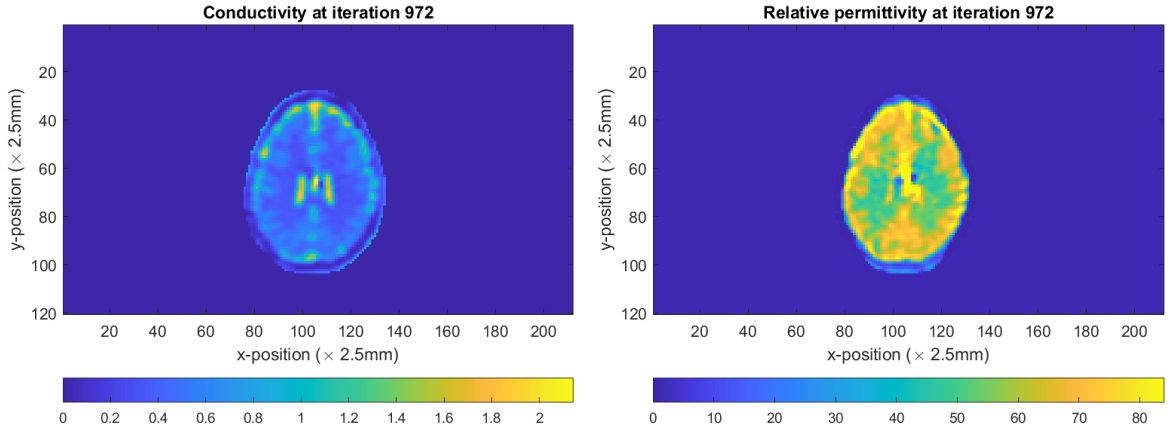

(e) Reconstructed conductivity at SNR 150

(f) Reconstructed relative permittivity at SNR 150

Figure 3.18: The conductivity (a, c, e) and relative permittivity (b, d, f) of slice 320 with the positivity constraint, where the upper, middle and bottom rows show the reconstructions with an SNR of 50, 100 and 150, respectively.

Appendix B due to similar reasons. In the images, the boundary issues are also reduced due to the positivity constraint. Consequently, this enhancement is useful.

Lastly, the initialisation can help the algorithm to converge to the correct minimum. In this report, HEPT was considered. In noise-free slices with large areas, such as the pelvis slice, the HEPT functions well (see Appendix B). On the other hand, the slices with detailed structures, such as the head

slice, are more challenging to recover when using the HEPT initialisation. Moreover, in noisy data, the HEPT reconstruction is not helpful. It can even cause the algorithm to model the HEPT noise instead of the ground truth. Therefore, it is decided to still use the backpropagation instead of the HEPT initialisation.

Lastly, a robustness analysis was made to investigate if the early stopping and positivity constraint makes the algorithm more robust. First, the data was created with a different offset than the incident fields. In this case, it was seen that the positivity constraint still makes it possible to create decent reconstructions, while without this positivity constraint, the reconstructions lost most details. Furthermore, the positivity constraint helps to get sharp conductivity images even though the data was corrupted by noise. The relative permittivity was more affected by the noise than the conductivity, so the reconstructions are less accurate, but they still capture more details than without the positivity constraint. The early stopping results in blurred images when no positivity constraint is implemented, but the final reconstructions have far more errors (see Appendix A). Therefore, the robustness analysis suggests that the enhancements indeed improve the 2D-CSI algorithm.

Algorithm 3 2D-Contrast Source Inversion with enhancements

Initialize $\boldsymbol{w}_0$, χ_0, $\boldsymbol{E}_0$, and φ_0^-
  while $n \leq N$ **do**
    Fix χ to update $\boldsymbol{w}_n = \boldsymbol{w}_{n-1} + \alpha_n^w \boldsymbol{v}_n$
    Fix $\boldsymbol{w}_n$ to update $\boldsymbol{E}_n = \boldsymbol{E}^{inc} + \mathcal{G}_D\{\boldsymbol{w}_n\}$
    Fix $\boldsymbol{w}_n$ and $\boldsymbol{E}_n$ to update $\chi_n = \dfrac{\boldsymbol{w}_n \cdot \boldsymbol{E}_n^\dagger}{|\boldsymbol{E}_n|^2}$
    Update $\varphi_n^- = \angle(B_1^{-;sca} + B_1^{-;inc})$
    if $\Re\{\chi(\boldsymbol{r})\} + 1 \leq 0$ **then**
      $\chi_n(\boldsymbol{r}) = -\Re\{\chi_n(\boldsymbol{r})\} + j\Im\{\chi_n(\boldsymbol{r})\}$
    if $\Im\{\chi(\boldsymbol{r})\} \geq 0$ **then**
      $\chi_n(\boldsymbol{r}) = \Re\{\chi_n(\boldsymbol{r})\} - j\Im\{\chi_n(\boldsymbol{r})\}$
    if $F(\boldsymbol{w}_n, \chi_n) <$ tolerance or $F(\boldsymbol{w}_n, \chi_n) > F(\boldsymbol{w}_{n-1}, \chi_{n-1})$ **then**
      Break
  Calculate $\epsilon_r = \Re(\chi) + 1$
  Calculate $\sigma = -\omega\epsilon_0\Im(\chi)$

Therefore, positivity constraints and early stopping should be implemented. The adjusted algorithm now becomes Algorithm 3 in which the positivity constraint implementation is cyan coloured and the early stopping blue coloured.

4

Performance of 2D-CSI on the 3D ADEPT dataset

4.1. Available dataset

The ADEPT dataset [16] consists of 120 different brain models, of which 84 are healthy brains, and 36 have a tumor inclusion. The brain models are segmented into three distinct tissue types: CerebroSpinal Fluid (CSF), Gray Matter (GM), and White Matter (WM). Moreover, the tumor data is divided into three types: Edema, Non-Enhancing Tumor (NET) and Active Tumor (AT). All brains were inserted in the Duke body model from the virtual family [15]. This thesis considers two randomly chosen brain models from the dataset, of which one is a healthy brain model (M30) and one is a brain model with a tumor (M86); see Figure 4.1. Table 4.1 provides the corresponding EPs for all tissue types for both brain models. Each brain model consists of 164 slices with each dimension of $260\ mm$ by $220\ mm$ and a $1\ mm$ isotropic grid. The main focus is on the 80th slice of both brains, placed in the middle of the birdcage coil. The assumption for a non-varying electric field in the z-direction is the most viable in the middle, so the 2D assumption is reasonable. Figure 4.2 provides the EP maps for the two brain models at the 80th slice.

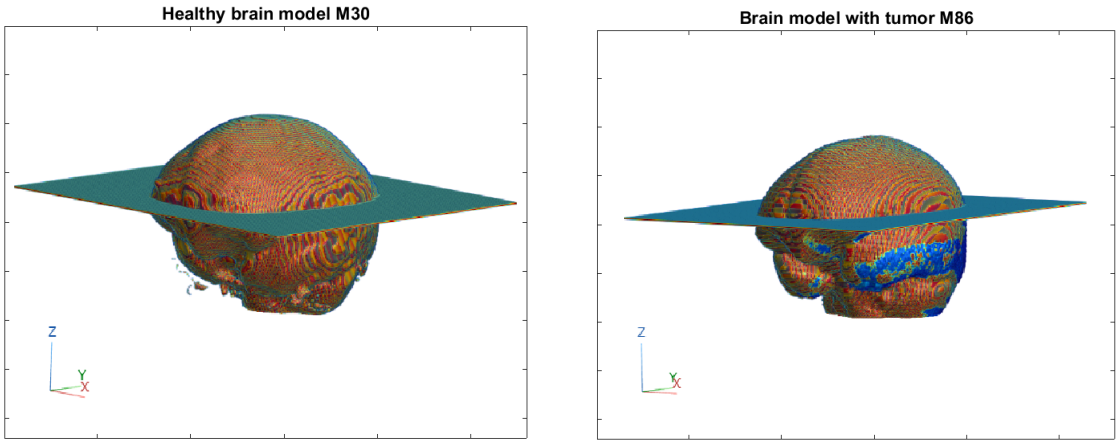

(a) Brain model M30 **(b)** Brain model M86

Figure 4.1: The brain models of the considered subjects and the planes of interest, with (a) the healthy brain model M30 and (b) the brain model M86 with a tumor inclusion (in blue).

4.1.1. Electric and magnetic fields

The corresponding electric and magnetic fields are calculated using the electromagnetic simulation program Sim4life (Zurich MedTech, Zurich, Switzerland). In Sim4life, a 3T birdcage coil is modelled

Table 4.1: The EPs from each tissue type for both brain models.

Subject information		EP healthy tissue (σ [S/m], ε[-])						EP tumor tissue (σ [S/m], ε [-])					
Identifier	Health	σ_{CSF}	ϵ_{CSF}	σ_{GM}	ϵ_{GM}	σ_{WM}	ϵ_{WM}	σ_{Edema}	ϵ_{Edema}	σ_{NET}	ϵ_{NET}	σ_{AT}	ϵ_{AT}
M30	Healthy	2.13	86	0.56	75	0.35	52	n.a.	n.a.	n.a.	n.a.	n.a.	n.a.
M86	Tumor	2.14	84	0.59	73	0.34	53	0.74	60	0.94	80	1.14	70

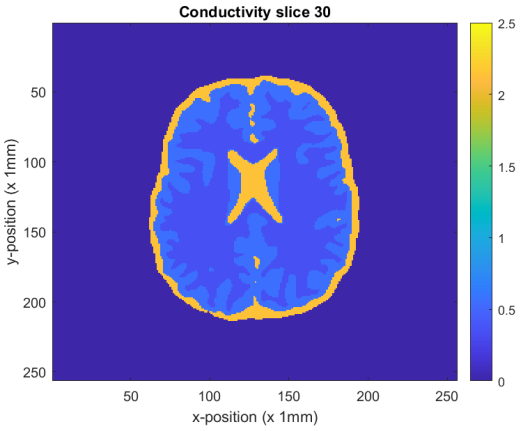

(a) Original conductivity M30 slice 80

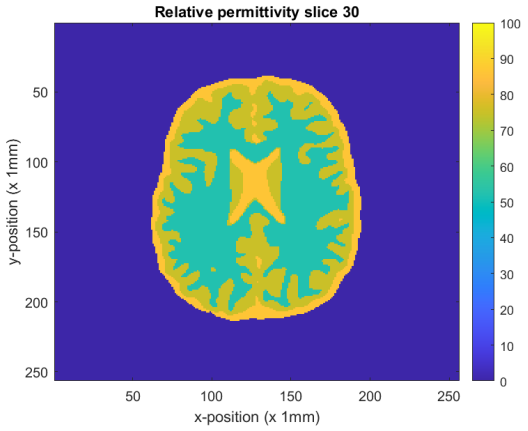

(b) Original relative permittivity M30 slice 80

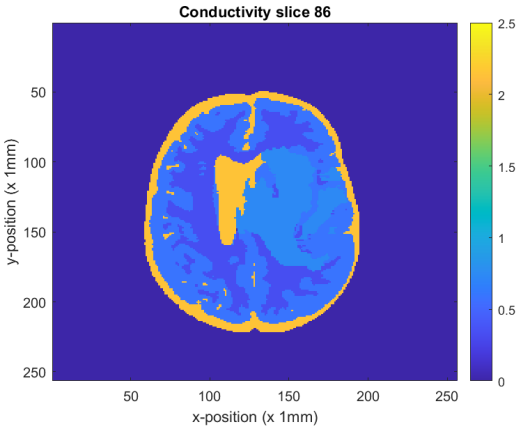

(c) Original conductivity M86 slice 80

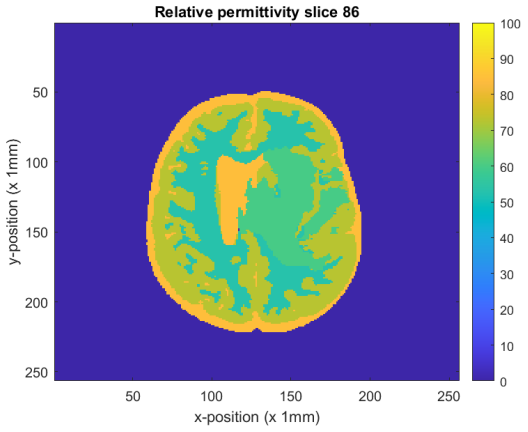

(d) Original relative permittivity M86 slice 80

Figure 4.2: The conductivity (a, c) and the relative permittivity (b, d) of slice 80 of M30 in the top row and M86 in the bottom row, respectively.

with 16 legs, an RF-shield radius of 371.5 mm, and a coil radius of 352 mm. As the 2D-CSI algorithm assumes a constant electric field in the z-direction, it is important to see to what extent the assumption is true. In Figure 4.3, phase changes are observed in the middle and at the edges of the brain. Hence, the algorithm is expected to not work properly in these areas. Moreover, when the E_z magnitude is considered in Figure 4.4, the magnitude is low at the centre, resulting in even more problems. Furthermore, the surrounding slices have multiple pixels at slightly different magnitudes. However, the magnitude differences are small. The E_z values show that the assumption is not completely true at certain locations (in the middle and at the edges). Therefore, it is expected that the algorithm might be affected at the centre and edged by these factors. Nevertheless, there could still be reasonable results.

Figure 4.5 provides the magnetic fields. The magnitude of the transmit and receive fields are almost mirrored. Furthermore, if the transmit phase is compared with the transceive phase, there are small deviations at the edge. Therefore, the TPA does not hold perfectly at the edges, which can cause some artefacts in the reconstruction.

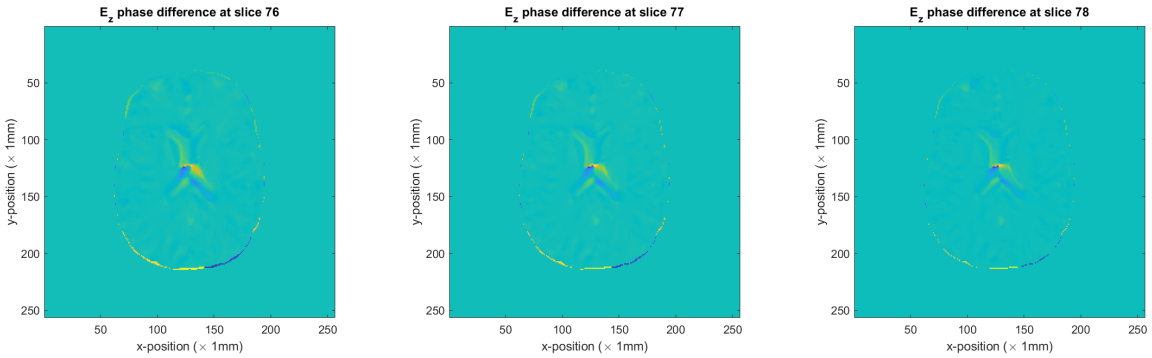

(a) Phase difference between slices 76 and 80 **(b)** Phase difference between slices 77 and 80 **(c)** Phase difference between slices 78 and 80

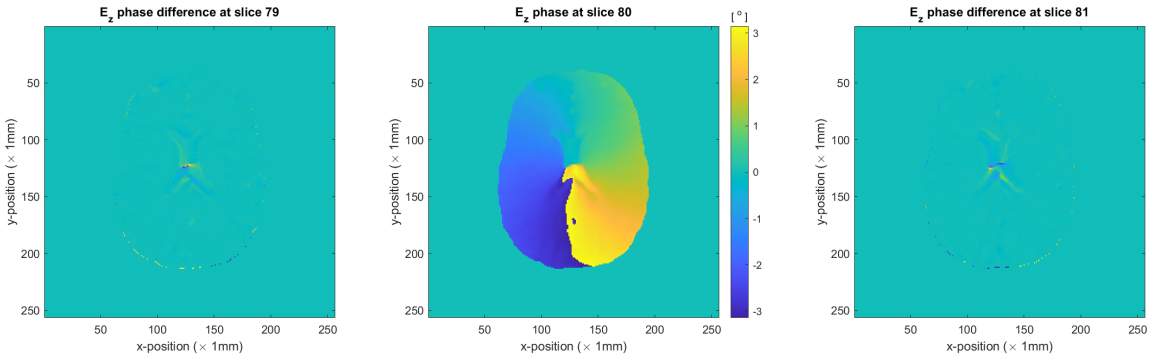

(d) Phase difference between slices 79 and 80 **(e)** Phase of slice 80 **(f)** Phase difference between slices 81 and 80

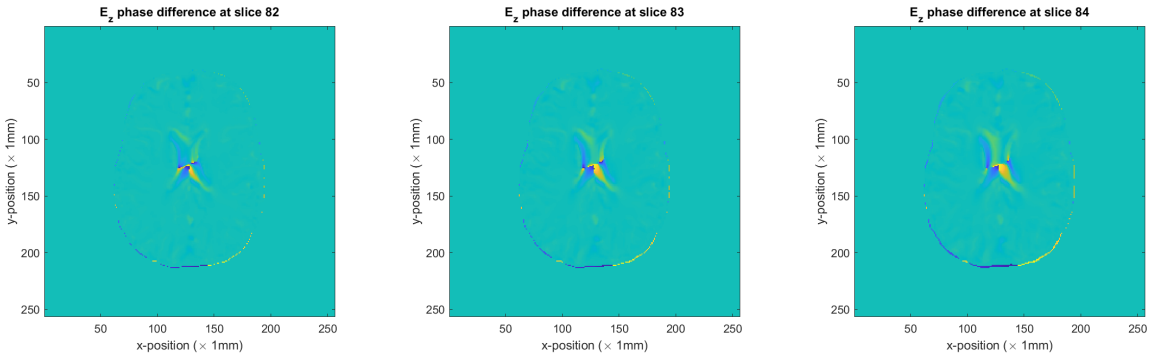

(g) Phase difference between slices 82 and 80 **(h)** Phase difference between slices 83 and 80 **(i)** Phase difference between slices 84 and 80

Figure 4.3: The phase difference of E_z (a-d and f-i) around (e) slice 80 of the healthy brain model M30.

The dataset did not provide the required incident fields for the CSI algorithm. Therefore, the incident fields are simulated in a similar way as in Chapter 3. However, the incident fields' magnitude should align with the total field's magnitude. After some research (explained in detail in Appendix C), the best results were achieved by multiplying the incident electric field with $\frac{4}{3}$ and the incident magnetic fields with $\frac{1}{10}$. Furthermore, the results largely depended on the chosen offset θ; see Figure 3.3. Therefore, multiple offsets are tested.

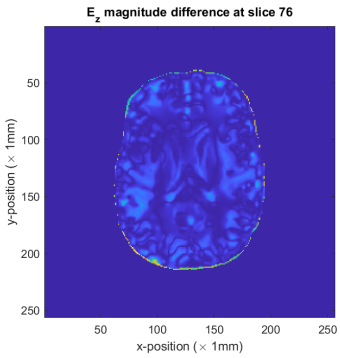

(a) Magnitude difference between slices 76 and 80

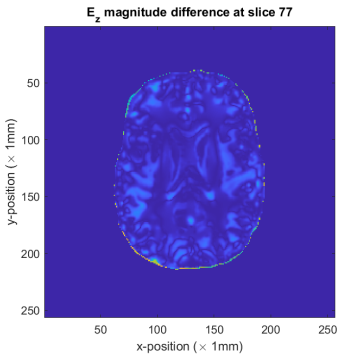

(b) Magnitude difference between slices 77 and 80

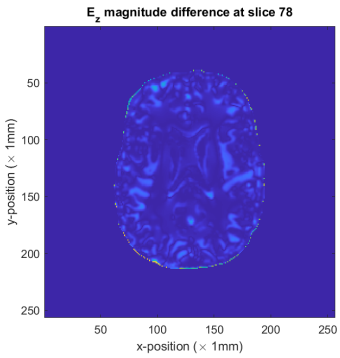

(c) Magnitude difference between slices 78 and 80

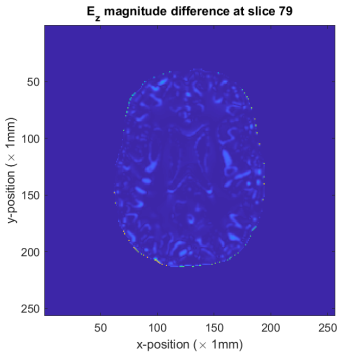

(d) Magnitude difference between slices 79 and 80

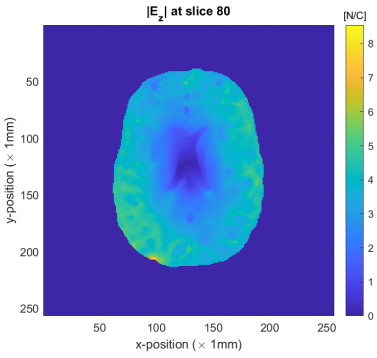

(e) Magnitude of slice 80

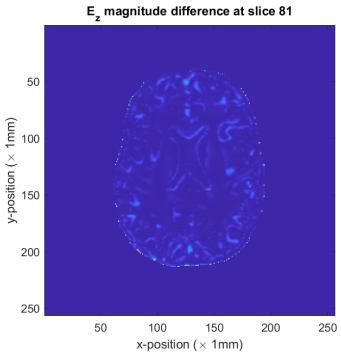

(f) Magnitude difference between slices 81 and 80

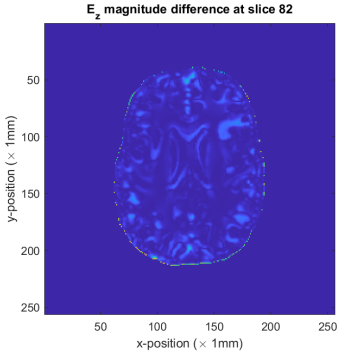

(g) Magnitude difference between slices 82 and 80

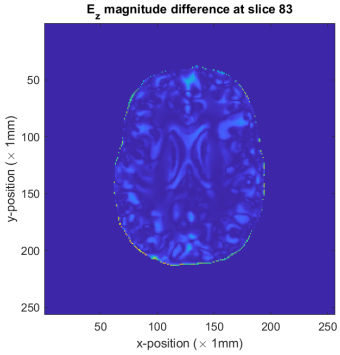

(h) Magnitude difference between slices 83 and 80

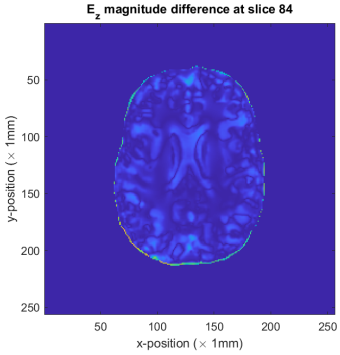

(i) Magnitude difference between slices 84 and 80

Figure 4.4: The magnitude difference of E_z (a-d and f-i) around (e) slice 80 of the healthy brain model M30.

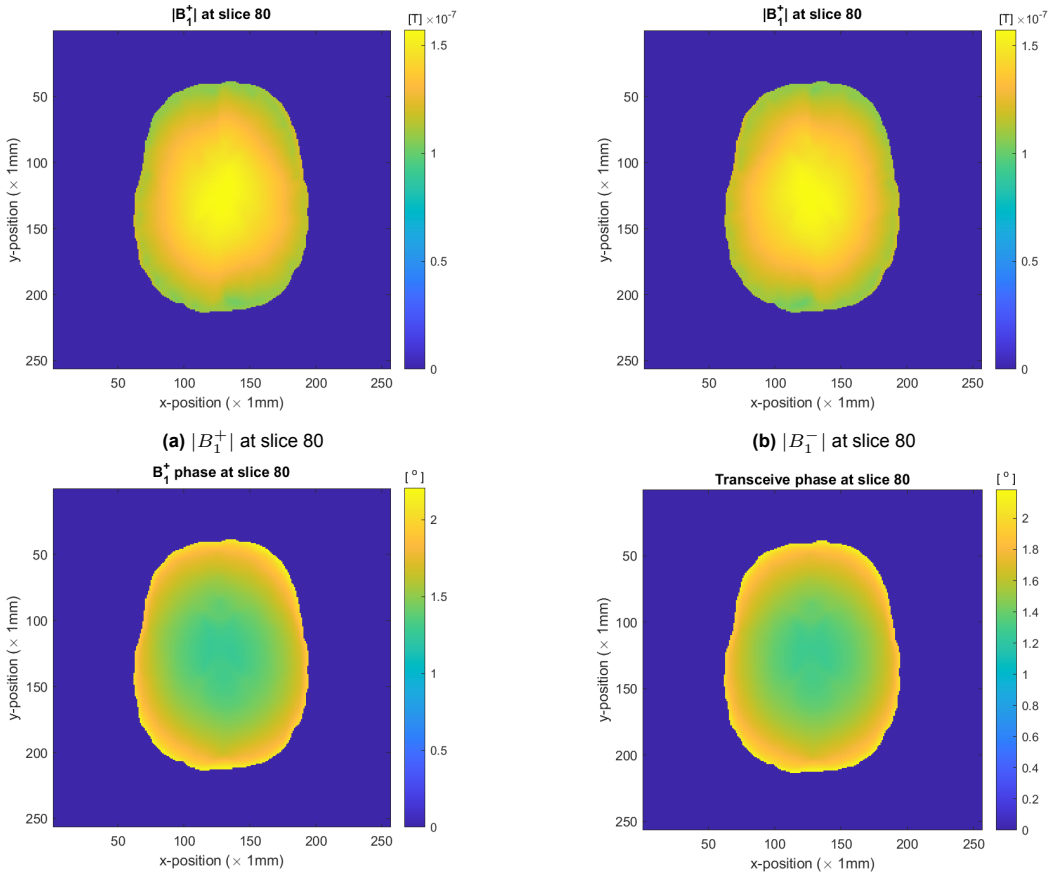

(a) $|B_1^+|$ at slice 80

(b) $|B_1^-|$ at slice 80

(c) B_1^+ phase at slice 80

(d) Transceive phase/2 at slice 80

Figure 4.5: The magnitude (a, b) and phase (c, d) of the transmit and receive field of M30 at slice 80.

4.2. Experiments with time convention conversion

This section investigates the effect of the positivity constraint on 3D data. The algorithm is run with and without this improvement to achieve this. Furthermore, the general settings are the same as for the Ella dataset, but it is important to note that it is now implemented on 3D data.

- Maximum number of iterations: 1000
- Tolerance: $1e-6$
- Update receive phase: on
- Multiplicative regularization: off
- Data: 3D

Moreover, as mentioned in Chapter 2, the time convention chosen by the designers of the ADEPT dataset is the physicist's convention. However, the algorithm expects the time convention of the engineers. Therefore, before the algorithm can be applied to the data, the dataset is converted to the other time convention by Equations 2.5, and 2.6.

4.2.1. Without positivity

Healthy brain model

Figure 4.6 gives the algorithm's results for the healthy brain model without the positivity constraint with two different offsets (0^o and 240^o). The reconstructed conductivity and relative permittivity underestimate the actual EP values; see the top row of Figure 4.2 for comparison, which is expected since Stijnman found similar effects [14]. Another reason for this underestimation is that the magnitude of the incident fields does not match the magnitude of the fields in the ADEPT dataset perfectly. Besides the underestimation, the reconstructions show areas that were reconstructed correctly and others that show artefacts. For both offsets, the centre causes problems. Moreover, each offset has an additional line in which the algorithm fails. The artefacts in the reconstructions with the first offset almost coincide with the vertical line, while the second is a slightly tilted horizontal line.

Figure 4.7 presents the final reconstructed electric fields to understand the cause of these errors. The electric fields show a magnitude close to zero around the same area where most errors in the reconstructions were found. In the contrast update, there is a division by the electric field; therefore, the larger conductivity and relative permittivity values seem reasonable. A solution could be to either change the update scheme of the contrast to gradient descent (similar to the contrast source update schema) or calculate the points at the lowest electric field differently (interpolate with surrounding points or set to zero). The reconstructions show, indeed, a significant difference with another offset. Hence, it is necessary to choose the offset carefully.

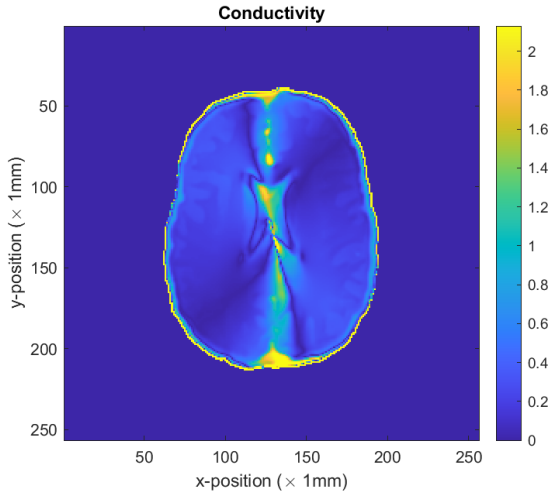

(a) Reconstructed conductivity

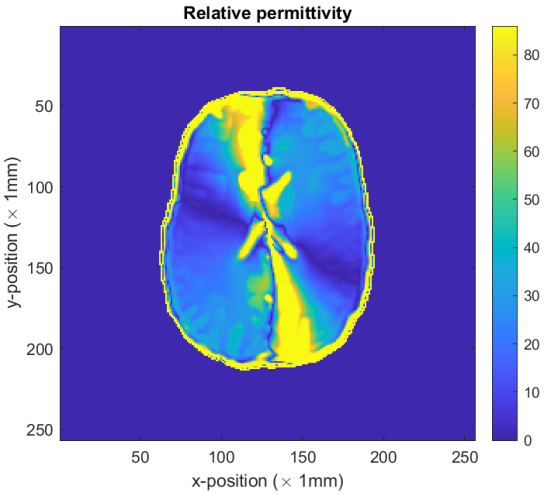

(b) Reconstructed relative permittivity

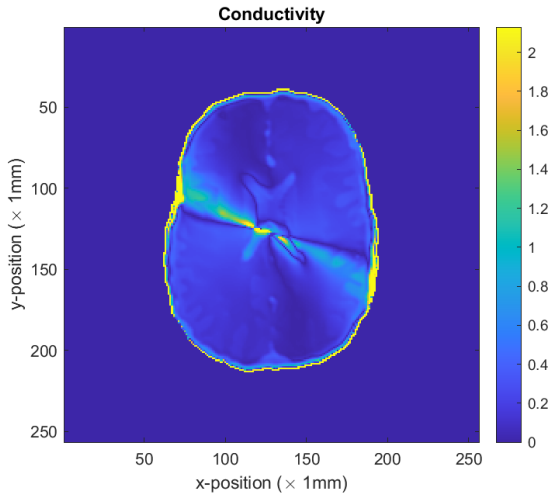

(c) Reconstructed conductivity

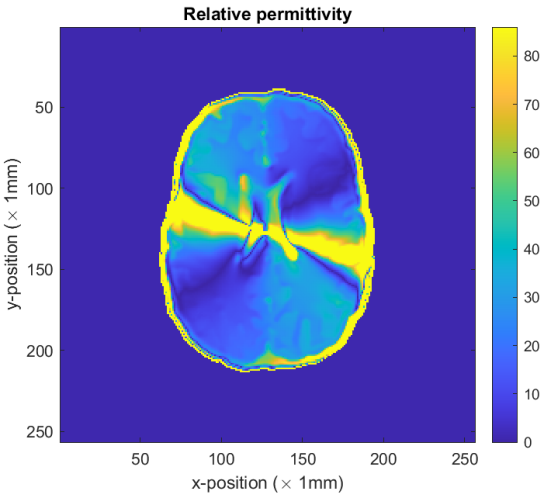

(d) Reconstructed relative permittivity

Figure 4.6: The reconstructions without positivity constraint of the conductivity (a, c) and the relative permittivity (b, d) of M30 slice 80. The reconstructions in the top row are made with an incident field offset of 0^o, while the bottom row has an offset of 240^o.

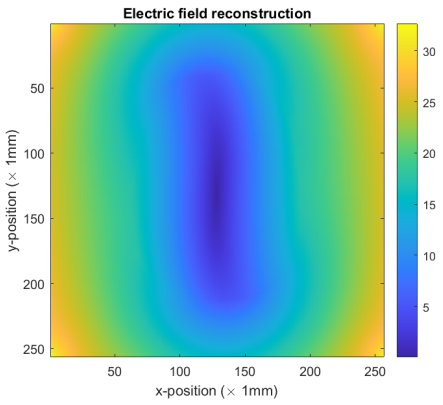

(a) Final electric field

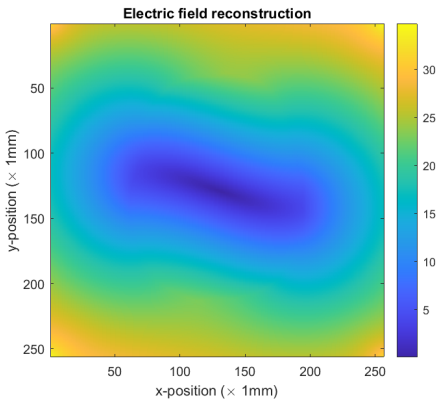

(b) Final electric field

Figure 4.7: The total electric field reconstructions without positivity constraint of M30 slice 80. The reconstruction in the left column was made with an incident field offset of 0^o, while the right column has an offset of 240^o.

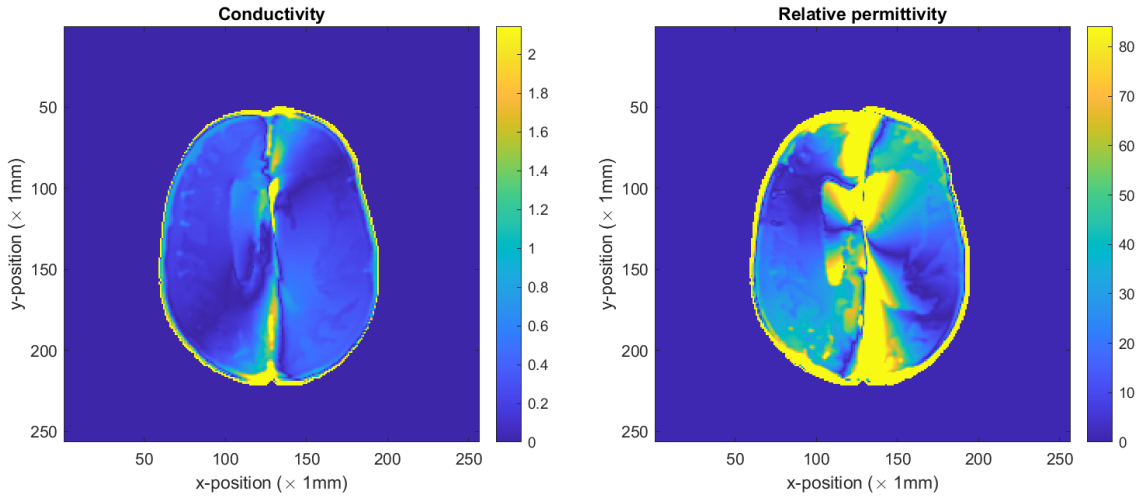

(a) Reconstructed conductivity

(b) Reconstructed relative permittivity

Figure 4.8: The reconstruction without positivity constraint of the conductivity (a) and the relative permittivity (b) of M86 slice 80 with an offset of 0^o.

Brain model with tumor

The brain model with the tumor inclusion has results similar to the healthy brain model. Figure 4.8 shows the reconstructions without the positivity constraint. The structure of the original EPs (Figure 4.2 bottom row) is imprinted in some areas in the reconstruction. However, in this case, the algorithm underestimates the values again for the same reasons. Moreover, the electric field again converged to a line, resulting in additional artefacts on the line where the electric field is small, in this case on the vertical axis, just as the results in the healthy brain model. The spot at which this artefact is present again depends on the chosen offset for the incident field, and the position is changed with a different offset.

4.2.2. With positivity

Healthy brain model

Figure 4.9 shows the reconstructions of the healthy brain model with the positivity constraint implemented. The algorithm converges to realistic values in small areas of the imaging domain. The conductivity, especially, is only reconstructed correctly in very small areas. A reason for these small areas could be that the positivity constraint is too strict, considering that the 2D algorithm is now applied to 3D data, and so can not help the algorithm converge correctly everywhere. Nevertheless, the reconstruction quality is better in those areas than without positivity constraint. Still, there are some pixels inside the imaging domain in which the values overshoot. The pixel locations correspond to the areas with a small electric field (Figure 4.10).

Figure 4.11 reveals a match between the position where the positivity constraint is applied and where the algorithm does not converge. Furthermore, at most of these positions, the flip is done in almost every iteration (the amount of flips is close to 1000). Hence, implementing the positivity constraint does not help the algorithm converge for the entire image, only in small sections. On the other hand, these constraint maps could help by automatizing the full reconstruction. Namely, the areas where the positivity constraint is not used are equal to the correctly reconstructed areas, so only these areas should be used in a full reconstruction.

Combine images

The entire reconstruction with the positivity constraint can be created by combining multiple reconstructions with different offsets. As the conductivity is reconstructed correctly in small areas, it is decided to take offset differences of 10^o, resulting in 36 independent reconstructions. The constraint maps can be used as an indication of the proper reconstruction areas. Hence, the images are combined, con-

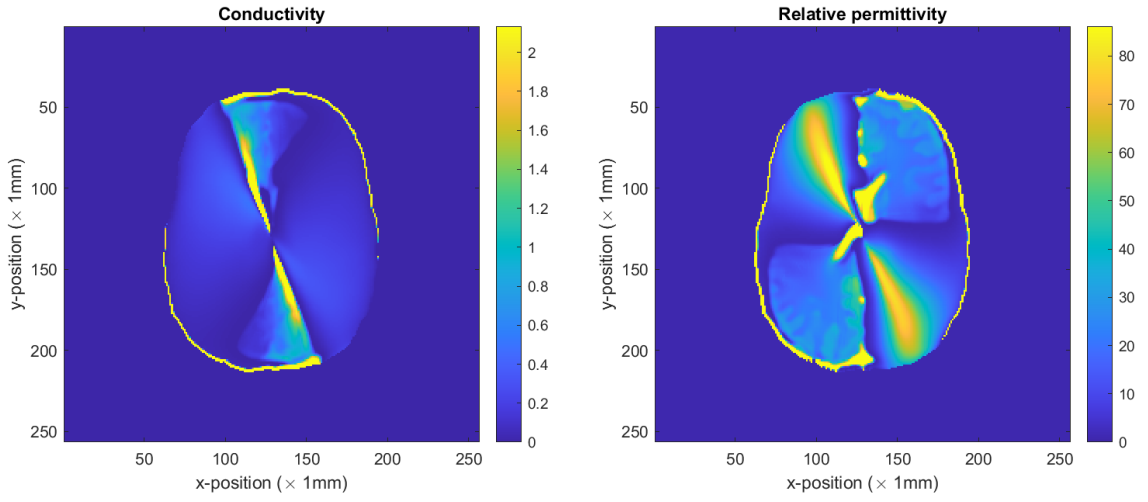

(a) Reconstructed conductivity

(b) Reconstructed relative permittivity

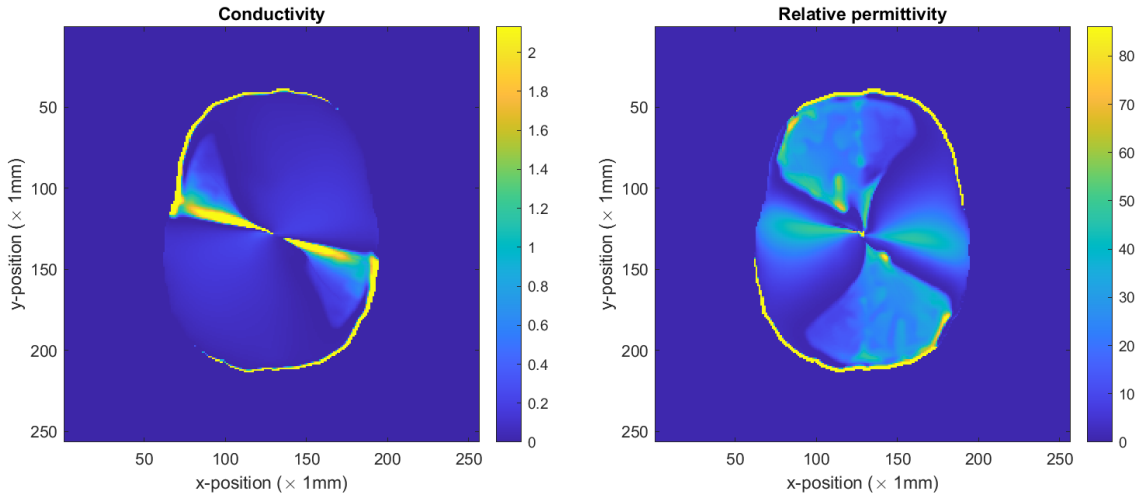

(c) Reconstructed conductivity

(d) Reconstructed relative permittivity

Figure 4.9: The reconstructions with positivity constraint of the conductivity (a, b) and the relative permittivity (b, d) of M30 slice 80. The reconstructions in the top row are made with an incident field offset of 0^o, while the bottom row has an offset of 240^o.

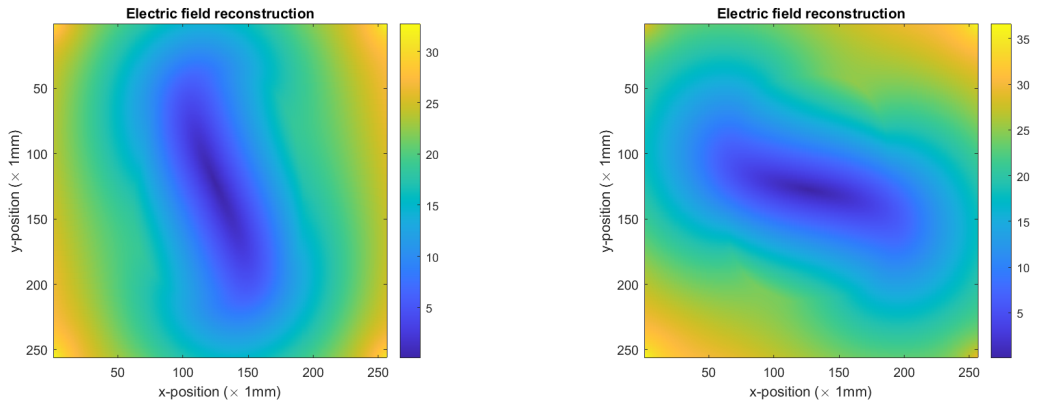

(a) Final electric field

(b) Final electric field

Figure 4.10: The total electric field reconstructions with positivity constraint of M30 slice 80. The reconstruction in the left column was made with an incident field offset of 0^o, while the right column has an offset of 240^o.

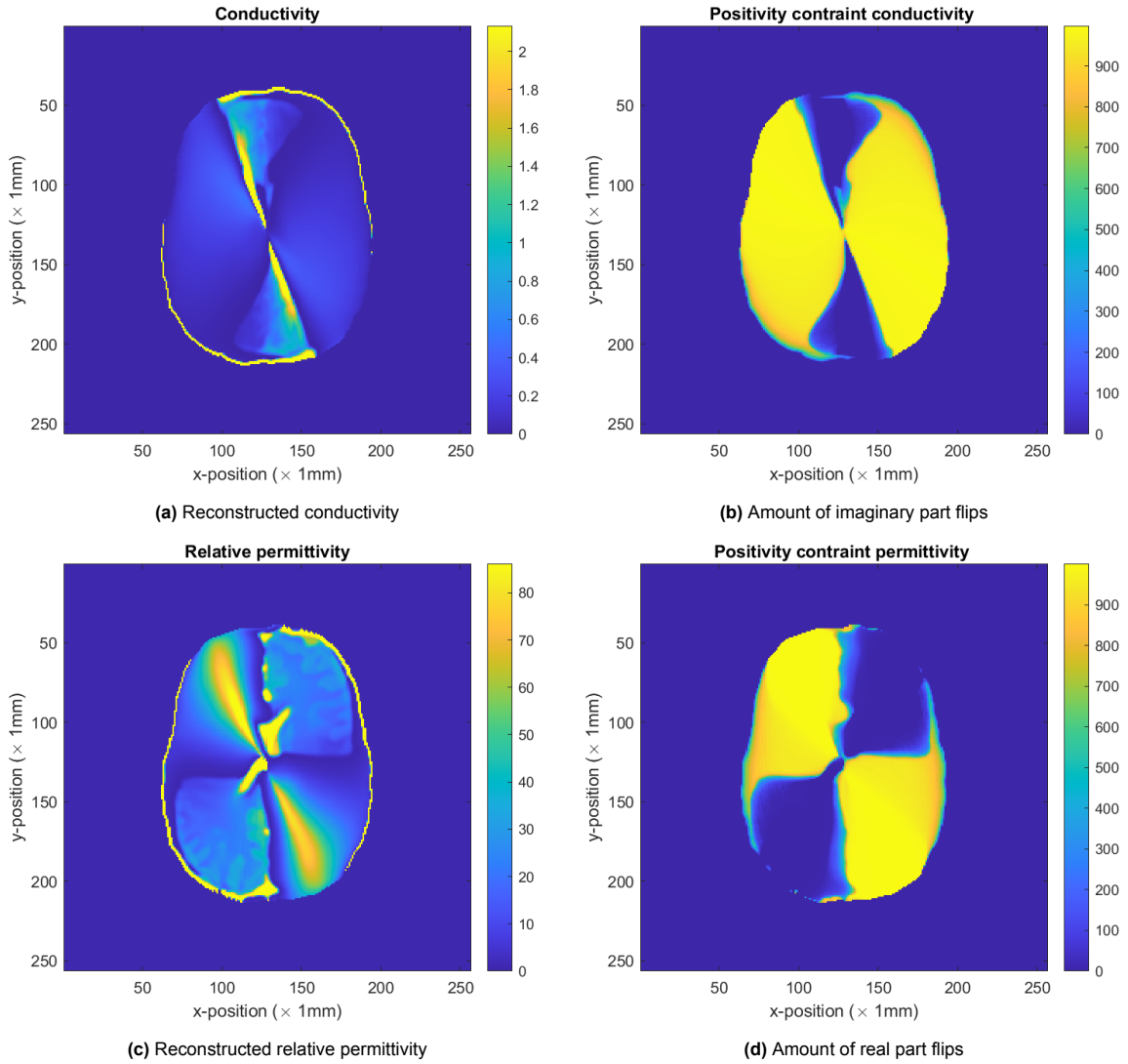

(a) Reconstructed conductivity

(b) Amount of imaginary part flips

(c) Reconstructed relative permittivity

(d) Amount of real part flips

Figure 4.11: The upper row shows the conductivity reconstruction (a) and the number of flips of the imaginary part (b). The bottom row shows the relative permittivity reconstruction (c) and the number of flips of the real part (d).

sidering how many reconstructions work for each pixel. Figure 4.12 shows the reconstructions when the multiple runs with different offsets are combined. The conductivity reconstruction is reconstructed quite well except for some areas in the centre, and the values are still underestimated. The relative permittivity reconstruction also underestimated the actual values. However, the contrast between areas is seen more clearly in these reconstructions. Unfortunately, the different offset reconstructions did not all have similar magnitudes, making the upper left and lower right corners brighter. This effect might be mitigated by taking the median instead of the average in each pixel. Moreover, the centre of the image still causes some problems, as expected, as the Ez polarization is not small there. Nevertheless, the reconstructions are of better quality than those without positivity constraints. This positivity constraint does come at the cost of a longer calculation time, as the reconstruction is now performed 36 times instead of once.

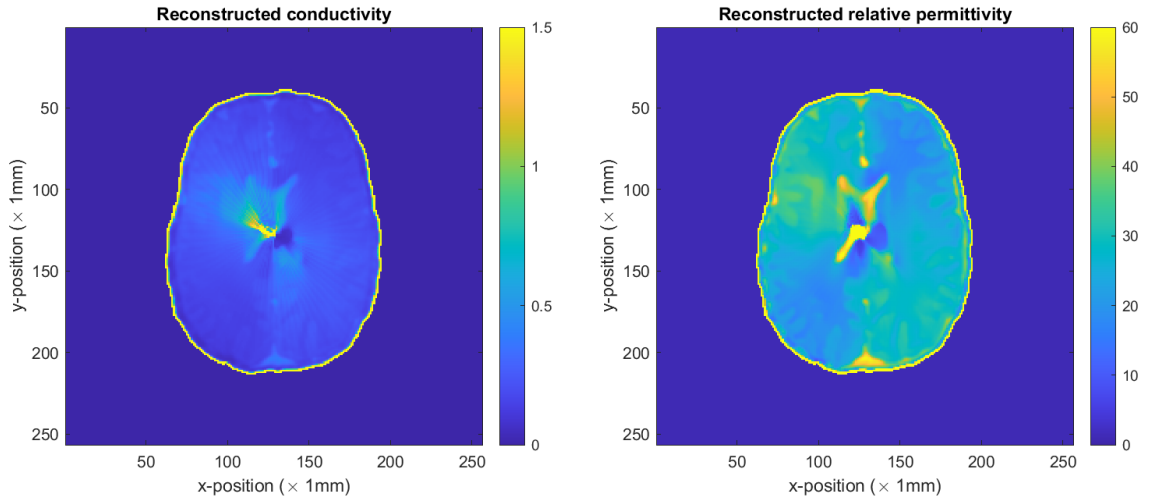

(a) Combined conductivity

(b) Combined relative permittivity

Figure 4.12: The conductivity (a) and relative permittivity (b) combined reconstructions are given for slice 80 of brain model M30. The combination comprises 36 images with an offset difference of 10^o.

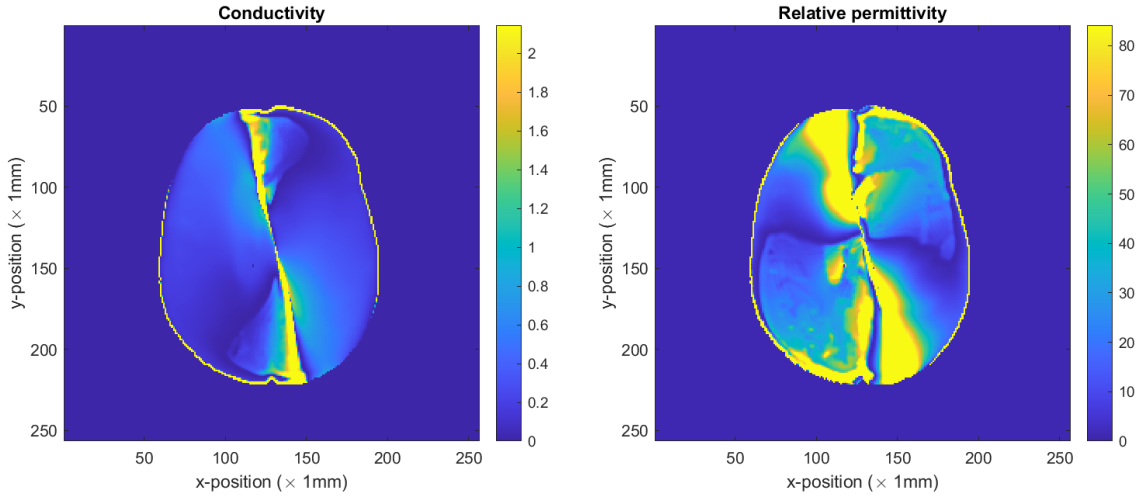

(a) Reconstructed conductivity

(b) Reconstructed relative permittivity

Figure 4.13: The reconstruction with positivity constraint of the conductivity (a) and the relative permittivity (b) of M86 slice 80. The reconstructions are made with an offset of 0^o.

Brain model with tumor

Figure 4.13 provides the reconstructions of the brain model with tumor inclusion. The chosen offset of the incident field is again 0^o. As seen before by the healthy brain model, the reconstructions only converge partly. However, if the reconstructions are compared with Figure 4.8, the reconstructions in the converge areas are more accurate. This larger accuracy can be observed for the relative permittivity as a larger area converges. As before, masks can be designed for locations where the positivity constraint is not applied, as the algorithm has converged correctly in those areas.

Combine images

Figure 4.14 combines 36 reconstructions with different offsets to create the combined conductivity and relative permittivity. The reconstructions in the upper right and lower left corners can be interpreted correctly. The other areas, however, are less readable, on the one hand, due to slight deviations between the average of different reconstructions and, on the other, due to an overshoot on the diagonal.

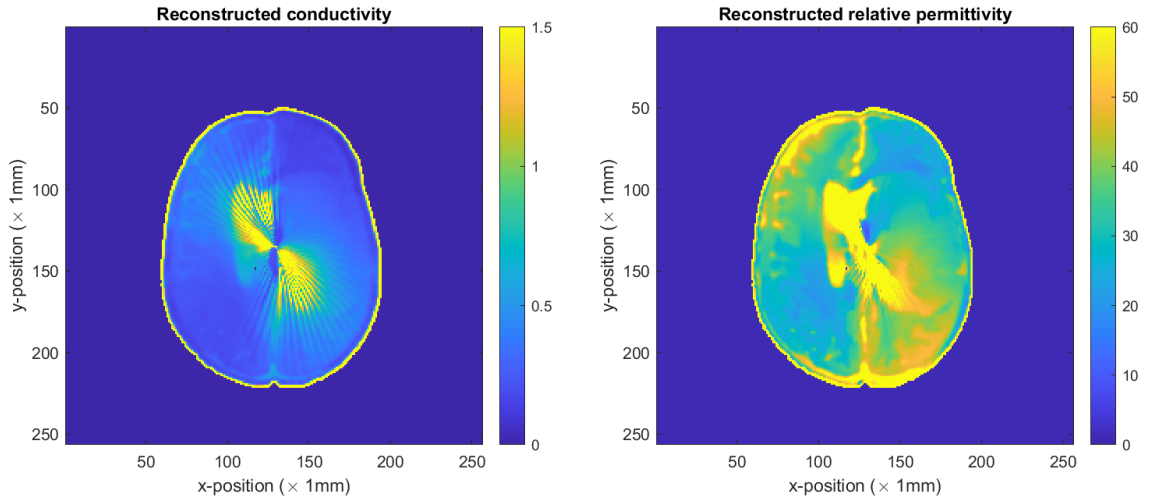

(a) Combined conductivity

(b) Combined relative permittivity

Figure 4.14: The conductivity (a) and relative permittivity (b) combined reconstructions are given for slice 80 of brain model M86. The combination comprises 36 images with an offset difference of 10^o.

These effects can be mitigated by taking the median instead of the average between pixels and not considering the values of pixels which are sufficiently larger than the other pixels.

4.3. Experiments without time convention conversion

The results show that the algorithm has problems correctly retrieving the entire reconstruction area in a single run. These problems suggest that there is no perfect match between the incident fields and the received data or that the 2D constraints are too strict for the algorithm to converge correctly. The algorithm is run without applying the conversion formulas to the ADEPT data to investigate further if the results depend on the incident fields. Therefore, the time convention of the data does not correspond to the time convention of the incident fields and algorithm. Furthermore, the general settings are identical, and the dataset is still 3D.

- Maximum number of iterations: 1000
- Tolerance: $1e-6$
- Update receive phase: on
- Multiplicative regularization: off
- Data: 3D

4.3.1. Without positivity

Healthy brain model

Figure 4.15 gives the algorithm's results for the healthy brain model without the positivity constraint with two different offsets (0^o and 240^o). The figure shows that the algorithm can still achieve reasonable reconstructions. As before, the values of the EPs are underestimated. In this case, a larger part of the conductivity is reconstructed correctly, while the algorithm has more difficulties with the relative permittivity. Furthermore, the centre is causing problems, and each image has a line at which the reconstruction is unreliable. Unlike before, the offset of 0^o corresponds to artefacts on a horizontal line instead of the vertical line. The offset of 240^o has the artefacts mainly on the anti-diagonal instead of a slightly tilted horizontal line. When Figure 4.16 is compared with Figure 4.7, similar variations in the electric field reconstruction are observed. The variations correspond to a shift of 90^o, where this shift between conventions is seen for every offset.

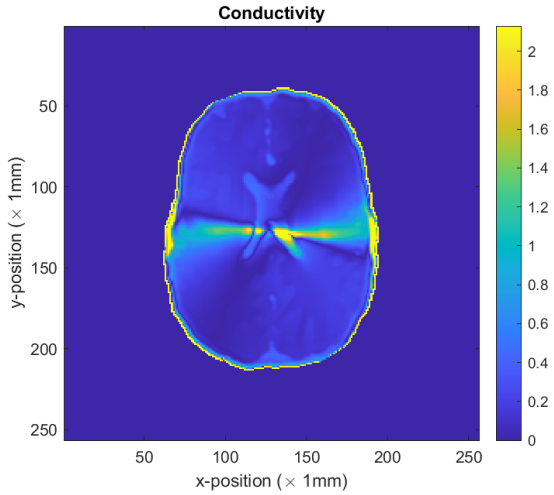

(a) Reconstructed conductivity

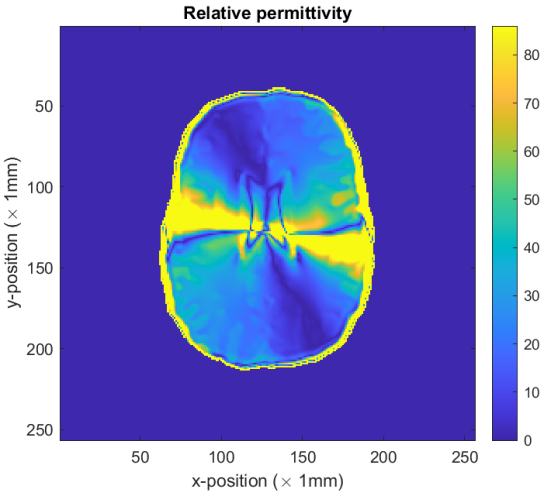

(b) Reconstructed relative permittivity

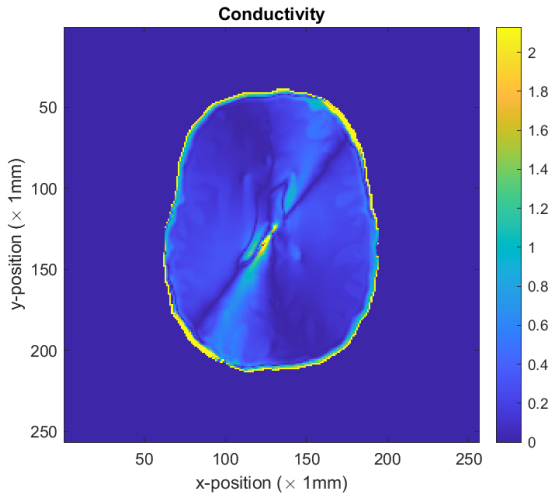

(c) Reconstructed conductivity

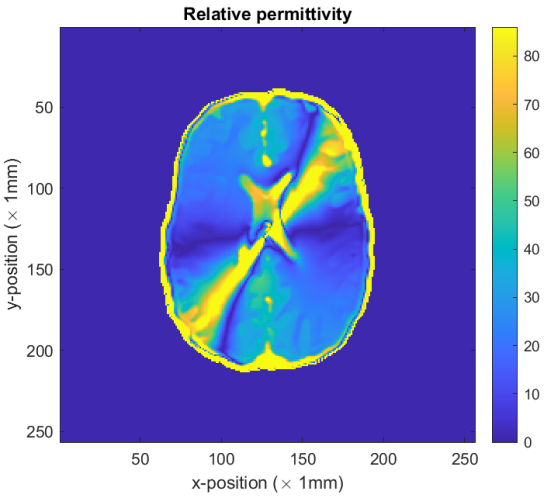

(d) Reconstructed relative permittivity

Figure 4.15: The reconstruction without positivity constraint of the conductivity (a, c) and the relative permittivity (b, d) of M30 slice 80. The reconstruction in the top row was made with an incident field offset of 0^o, while the bottom row has an offset of 240^o.

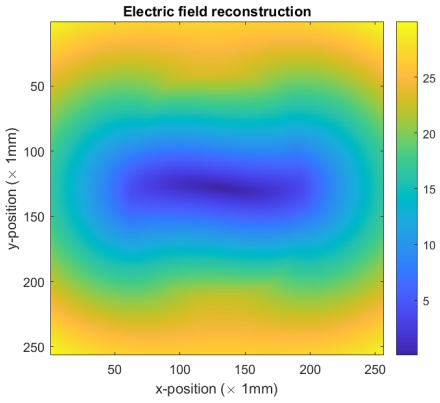

(a) Final electric field

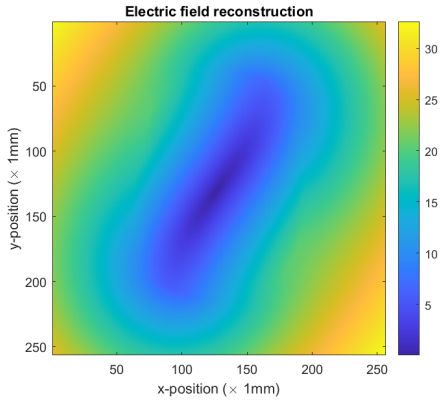

(b) Final electric field

Figure 4.16: The total electric field reconstructions without positivity of M30 slice 80. The reconstruction in the left column was made with an incident field offset of 0^o, while the right column has an offset of 240^o.

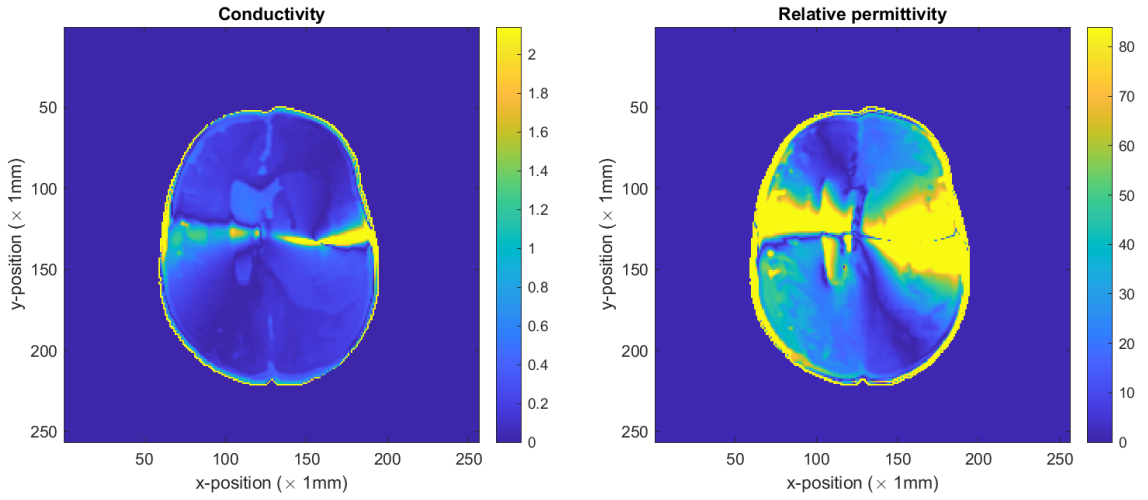

(a) Reconstructed conductivity

(b) Reconstructed relative permittivity

Figure 4.17: The reconstruction without positivity constraint of the conductivity (a) and the relative permittivity (b) of M86 slice 80. The reconstructions are made with an offset of 0^o.

Brain model with tumor

Figure 4.17 shows the EPs for the brain model with a tumor inclusion and an offset of 0^o. The tumorous regions are reconstructed quite well in the conductivity, while these regions in the relative permittivity include quite some artefacts. Furthermore, it can be observed that the location of the artefact line corresponds perfectly to the line seen in the top row of Figure 4.15. When the offset was adjusted, the line changed position. Therefore, this again suggests that combining information from multiple images results in a reasonable estimation of the whole area except for some pixels in the centre, which are always beneath artefacts.

4.3.2. With positivity

Healthy brain

Figure 4.18 shows the reconstruction with the positivity constraint implemented. The reconstruction still converges correctly locally instead of for the entire imaging domain. However, a larger section of the conductivity is reconstructed with each offset compared to the converted data reconstructions. On the other hand, the correctly reconstructed area for the relative permittivity is smaller than before, but luckily, it is not by much. Therefore, the conductivity and the relative permittivity can be found with only a few runs. Moreover, the local results with positivity are better than those without the positivity constraint. Consequently, there is a preference for using the positivity constraint. Still, there are some areas in which the values overshoot. These areas correspond to the areas with a small electric field.

Figure 4.20 presents a perfect match between the areas where the positivity constraint is applied and where the algorithm fails. Therefore, in the 3D dataset, the positivity constraint does not help the converge in the pixels where it is used; however, it does help the algorithm to focus on accurately reconstructing local areas. Furthermore the proper reconstruction areas still include unreasonable large values in the centre. Nevertheless, the positivity constraint maps can help by combining multiple reconstructions with different offsets as done with the other time convention. In this way, it is possible to reconstruct the entire imaging domain.

Combine images

In the case that the data is not converted, the correctly reconstructed local areas in conductivity and relative permittivity reconstructions spread decent areas. The conductivity covers a much larger area than the conductivity for the converted data. Therefore, it is possible to reconstruct the entire imaging domain with fewer reconstructions, making the algorithm significantly faster. However, for consistency, it is decided to take offset differences of 10^0 and combine reconstructions of 36 runs. As before, the

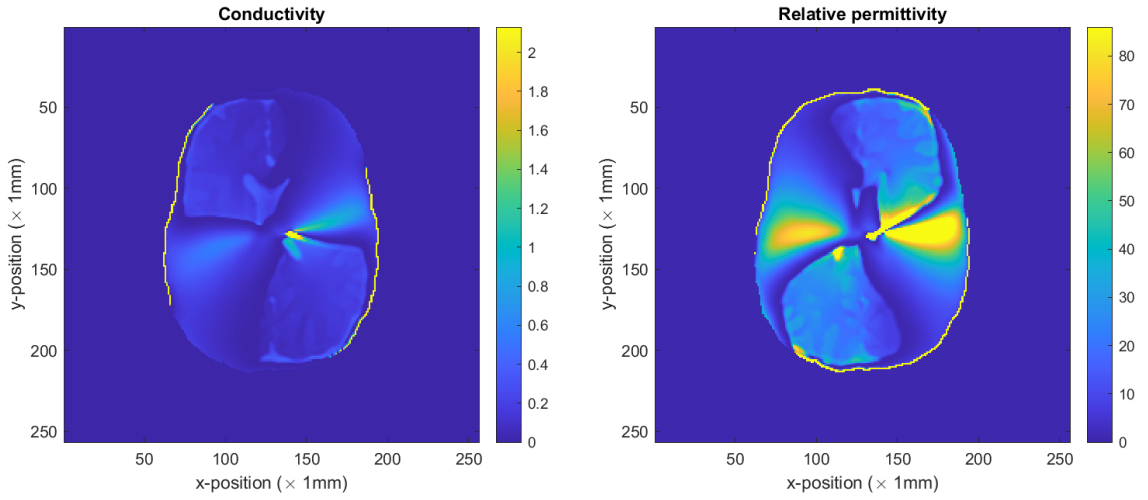

(a) Reconstructed conductivity

(b) Reconstructed relative permittivity

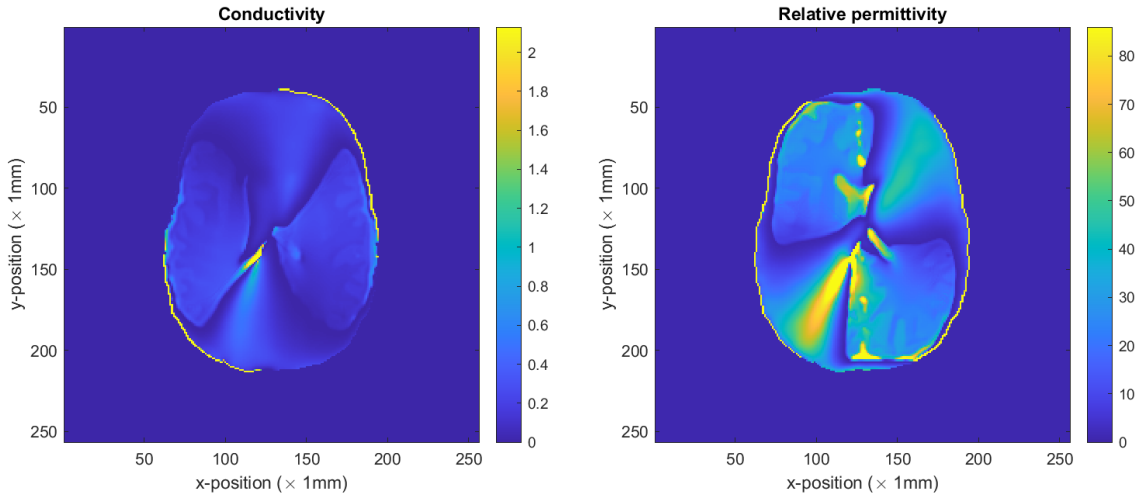

(c) Reconstructed conductivity

(d) Reconstructed relative permittivity

Figure 4.18: The reconstruction with positivity constraint of the conductivity (a, c) and the relative permittivity (b, d) of M30 slice 80. The reconstruction in the upper row was made with an incident field offset of 0^o, while the bottom row has an offset of 240^o.

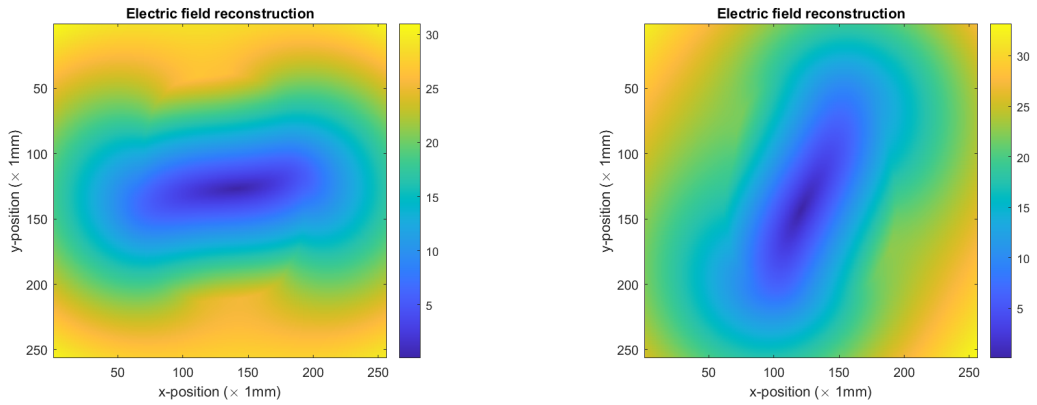

(a) Final electric field

(b) Final electric field

Figure 4.19: The total electric field reconstructions with positivity constraint of M30 slice 80. The reconstruction in the left column was made with an incident field offset of 0^o, while the right column has an offset of 240^o.

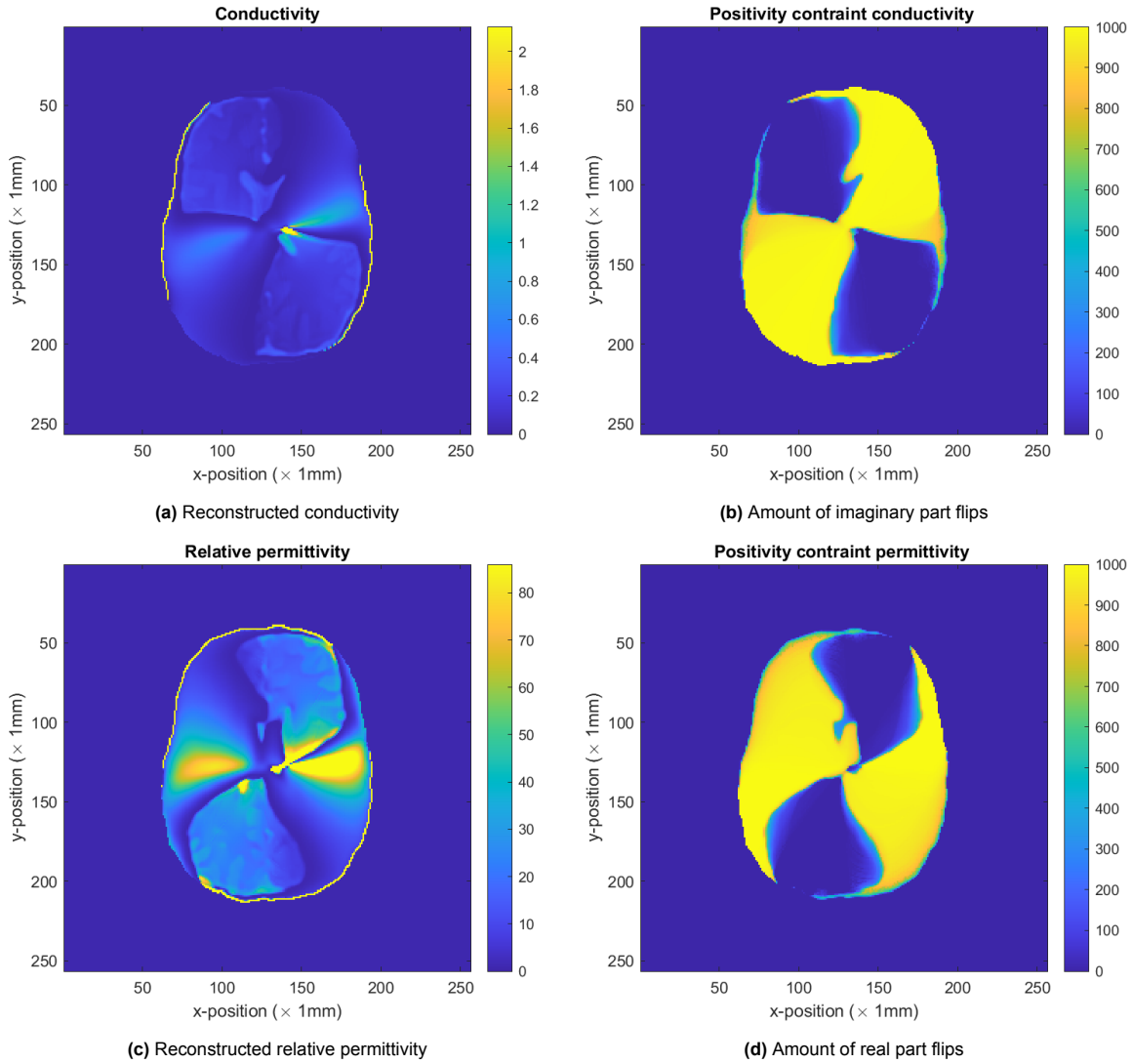

(a) Reconstructed conductivity

(b) Amount of imaginary part flips

(c) Reconstructed relative permittivity

(d) Amount of real part flips

Figure 4.20: The upper row shows the conductivity reconstruction (a) and the number of flips of the imaginary part (b). The bottom row shows the relative permittivity reconstruction (c) and the number of flips of the real part (d).

average is taken between each reconstruction that works on a pixel. The reconstruction works on a pixel when no positivity constraint is applied there. Figure 4.21 provides the combined reconstructions. The structures in the conductivity are reconstructed with high accuracy except for the centre. These problems in the centre are as expected as that area has a small electric field. The reconstruction values are underestimated due to the mismatch between the magnitudes of the incident fields and the total fields. Moreover, the algorithm is known to underestimate the values. The bright spots in the centre of the reconstruction are caused by the bright areas seen in, for example, 4.18. The relative permittivity has large areas that are reconstructed correctly; however, larger bright spots are observed. The large values could be excluded by removing pixels much larger than the average or taking the median of the reconstructions instead of the average. Furthermore, there is a horizontal area in the relative permittivity in the centre, which has a larger average value than the surrounding areas. The combination method should be adjusted to handle this; for example, the magnitude between reconstructions should be matched. Another option is a filter which finds values depending on the neighbours. A last option would be to implement the Jacobi update scheme [41] instead of the conjugate gradient scheme. This method is known to smooth areas; in this way, the reconstruction would have more homogeneity and sharper edges between different tissues.

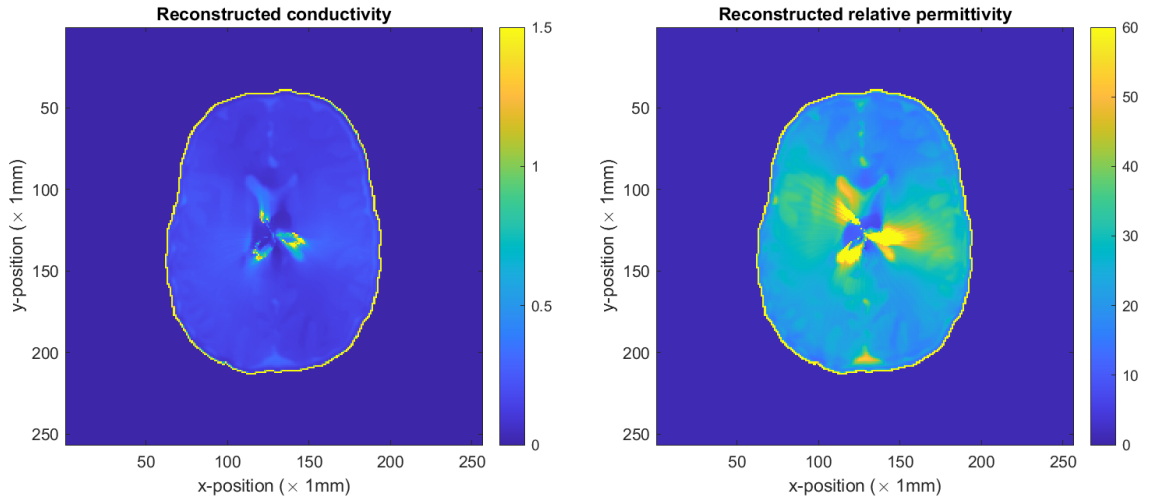

(a) Combined conductivity

(b) Combined relative permittivity

Figure 4.21: The conductivity (a) and relative permittivity (b) combined reconstructions are given for slice 80 of brain model M30. The combination comprises 36 images with an offset difference of 10^o.

If Figures 4.12 and 4.21 are compared, the conductivity reconstructions are very similar, but when the data was converted, more lines are seen in the pictures. These lines result from the small areas captured in each run. Therefore, the pixels are reconstructed using fewer runs, resulting in slight magnitude deviations. On the other hand, when the data is converted, the relative permittivity does not show these lines. At the same time, these lines are visible in the relative permittivity when the data is not converted. Furthermore, the relative permittivity without conversion includes more extreme values. On the contrary, this relative permittivity has fewer areas with an overall higher average. In this case, it is a horizontal strip, while the converted data results in these artefacts in the upper left and lower right corner. Hence, for the relative permittivity, both combined reconstructions have advantages and disadvantages. The conductivity does seem to have better reconstructions when the data is not converted. These advantages suggest a slight preference for applying the algorithm without converting the ADEPT data.

Brain model with tumor

Figure 4.22 shows the reconstruction for the brain model with a tumor inclusion, with an offset of 0^o. More than half of the conductivity is correctly reconstructed, and the tumor region is already visible. A small area lies in proper reconstruction where the pixel values are too large. The relative permittivity has a large area where the reconstruction values exceed logical values. This effect can relate to some pixels of the relative permittivity reconstruction inside the positivity constraint mask are close to the areas where the electric field is small. Without the positivity constraint, the relative permittivity is more affected by the smaller electric field than the conductivity, so it can result in worse images when multiple runs are combined without taking measures for this observed effect.

Combine images

Figure 4.23 provides the combined reconstruction. The conductivity reconstruction is accurate almost everywhere. Only the centre has a gap and a circle with extreme values. The circle could be avoided by measures mentioned before, such as removing the extreme values before taking the average. Fortunately, a large area is still reconstructed correctly. The relative permittivity has a larger area with unrealistic larger values. The area almost covers the tumorous region, making it difficult to observe the exact shape. Therefore, this shows that further research is essential to remove these bright spots.

If Figures 4.14, and 4.23 are compared, the relative permittivity is reconstructed with fewer artefacts when the data is converted. At the same time, the conductivity is better when the data is not converted. The conductivity is a promising biomarker for many illnesses, while the relative permittivity is expected

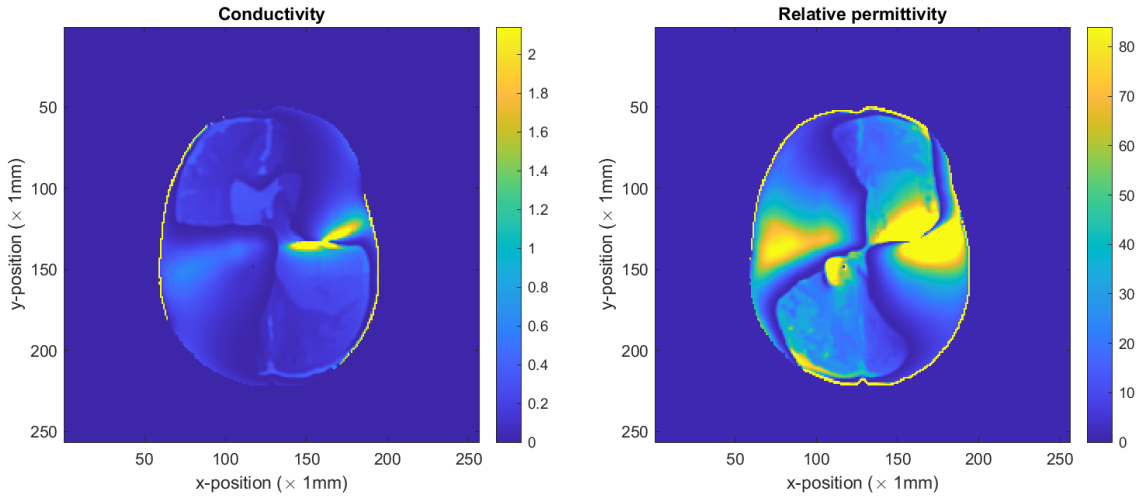

(a) Reconstructed conductivity

(b) Reconstructed relative permittivity

Figure 4.22: The reconstruction with positivity constraint of the conductivity (a) and the relative permittivity (b) of M86 slice 80. The reconstructions are made with an offset of 0^o.

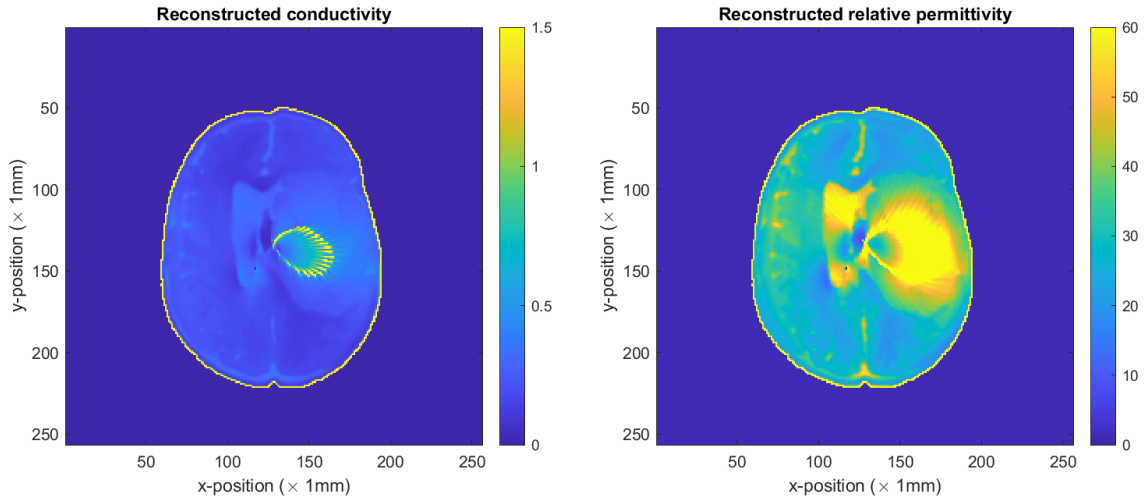

(a) Combined conductivity

(b) Combined relative permittivity

Figure 4.23: The conductivity (a) and relative permittivity (b) combined reconstructions are given for slice 80 of brain model M86. The combination comprises 36 images with an offset difference of 10^o.

to be effective. Moreover, the relative permittivity should be estimated more easily in a 7T machine than in the 3T machine used here. Therefore, it is more important to create proper conductivity images. Hence, it is suggested that it is better not to convert the data before applying the algorithm.

4.4. Conclusion

As seen in this chapter, the 2D-CSI algorithm can reconstruct 3D data for both a healthy brain model and a brain model with tumor inclusion. Unfortunately, it is less straightforward than for the 2D dataset. First, the data's magnitude must match the incident field's magnitude. After that, one should decide if the positivity constraint should be implemented. Without the positivity constraint, the entire imaging area is reconstructed but with significant artefacts, especially at the locations where the electric field is small. The location at which the electric field is small depends on the chosen incident field offset. In the 2D dataset, the algorithm had difficulties reconstructing the data when there was a mismatch between the data's offset and the incident fields' offset. Eventually, the algorithm could not reconstruct anymore. Luckily, in this 3D case, the algorithm is still able to reconstruct independently of the offset, but there is

no offset for which the algorithm is artefact-free. This effect suggests that the simulated incident field is not an entirely correct fit, and, therefore, the algorithm can still reconstruct something but with errors. This mismatch is reasonable as the incident fields consider infinitely long wires and no edge effects present. Moreover, these incident fields do not consider the head's loading. If the incident fields were modelled better, the reconstructions could improve a lot.

If the positivity constraint is implemented, the reconstruction focuses on a small section of the entire imaging domain. However, these local areas are reconstructed accurately. The location of the proper reconstructed areas depends on the chosen offset of the incident field. A more accurate incident field could help these reconstructions as well. In this case, the dependence on the offset could be used as a tool. Namely, good local reconstructions with different offsets could be combined to fill the entire imaging domain. This process can even be automated as the pixels on which the positivity constraint is not applied correspond to the pixels reconstructed quite well. It is important to note the local areas include some bright spots. More research should be performed on automatically finding and removing these bright spots. The resulting images can reconstruct the entire image domain with only minor artefacts, making it preferred above the reconstructions without positivity constraint. For these reconstructions, it also holds that a more accurate incident field can help to improve the reconstructions.

A last consideration is whether the received data should be converted to match the incident fields' and algorithms' time convention. It might seem straightforward to state that they should match; however, this chapter found that the algorithm reconstructs the conductivity better when data is not converted. On the other hand, the relative permittivity reconstruction is of a somewhat higher quality when the conversion is applied. However, as the advances in the conductivity reconstruction are more significant than the degrading of the relative permittivity, the reconstructions without the conversion are recommended.

5

Conclusion

This thesis investigates whether the 2D receive phase-corrected CSI algorithm can reconstruct the EPs of two brain models (one healthy brain model and one with a tumor inclusion) from the realistic 3D ADEPT dataset with high quality. The algorithm is first improved on a simpler 2D dataset to make it more robust. Three enhancements are proposed for this 2D dataset. The first enhancement is an early stopping at the minimum cost function. The early stopping is chosen because the cost function can increase when optimising an ill-posed problem, and this increase results in the modelling of artefacts. This adjustment results in a faster algorithm that models fewer artefacts but with blurred reconstructions. Therefore, this improvement is already helping the algorithm, although more adjustments are necessary to achieve sharper images.

The second enhancement is a positivity constraint on the conductivity and relative permittivity. The constraints are applied to the real and imaginary parts of the contrast function, as the algorithm does not update the conductivity and relative permittivity directly. The constraint is verified in every iteration instead of adjusting the cost function, keeping the simplicity. The positivity constraint helps to model the physics better, resulting in fewer artefacts related to the failing TPA. Additionally, the positivity constraint guides the algorithm more towards the ground truth which leads to the cost function minimum being at a later iteration. This results in sharper reconstructions at this minimum. The combination of the early stopping and the positivity constraint already leads to high quality images on the 2D dataset.

Lastly, to make the algorithm even faster and more accurate, another initialization is proposed. It is adjusted from back propagation to HEPT reconstructions. This adjustment is, however, only helpful in the noise-free at a slice without fine structures. Therefore, it is decided to not implement this further on.

The early stopping and positivity constraint are then tested in a robustness analysis. First, the offset of the incident field does not match the offset of the other fields. With the positivity constraint and early stopping the reconstructions become very close to the original except for some boundary issues. Without the positivity constraint but with the early stopping the reconstructions were very blurred. Lastly, without positivity and early stopping many artefacts are present. Therefore, it can be concluded that the positivity constraint and early stopping help the algorithm to be more robust to a mismatch in the fields' offset.

Furthermore, it is investigated if the early stopping and positivity constraint let the algorithm handle noise better. The reconstructions show that the positivity constraint shifts the cost function minimum to a later iteration and so results in sharper images. However, the noise is more present. Still, as the algorithm is able to capture more details, it is preferred to implement the positivity constraint. When the early stopping and positivity constraint were omitted the reconstructions include many artefacts and so this shows again that the enhancements should be used further on in later research. Hence, it can be concluded that the early stopping and positivity constraint indeed make the algorithm more robust.

The 2D-CSI algorithm is then applied to the 3D ADEPT dataset. First, the magnitude of the 2D simulated incident fields are matched to the 3D data. Then the ADEPT dataset is converted to match the time convention of the algorithm and the incident fields. After that, the 2D-CSI algorithm without and with the positivity is applied to the dataset to inspect the effect of the positivity constraint on the reconstructions. Without the positivity constraint, the reconstructions values are underestimated but part of the structure could be observed. Unfortunately, a large line artefact is formed in the reconstructions. The position of the artefacts depends on the reconstructed electric fields, which vary with different offsets in the incident electric field. This dependence on the offset suggests that the algorithm heavily depends on correctly simulating the incident fields.

With the positivity constraint, the algorithm only converges in certain areas where the positivity constraint was not violated (with still an underestimation of the values). Luckily, the location of the good reconstructions varies with the different offsets of the incident fields. Therefore, the positivity constraint maps can be exploited to combine multiple reconstruction areas. In the corresponding reconstructions, fewer artefacts are present than those without positivity constraint. However, the centre of the reconstruction domain still causes problems as almost no reconstruction includes the correct point, and some better pre-processing is necessary to account for value deviations between images and outliers.

The reconstruction of the 3D data depend a lot on the chosen incident fields, therefore, it is analysed if the algorithm is able to reconstruct if the time convention of the ADEPT data is different from the time convention of the incident fields and the algorithm. The corresponding reconstructions show similar behaviour for without and with positivity constraints. In this case, the conductivity reconstructions with positivity constraint do have larger correctly reconstructed areas as compared with the converted reconstructions while the relative permittivity shows the opposite. However, the conductivity is more important, making this second approach better. Note that this second approach is still not able to reconstruct the entire imaging domain in one run as the incident fields should not follow the 2D assumption.

In conclusion, the 2D CSI algorithm could be used to reconstruct EPs of brain models with and without a tumor when the brain is in the centre of a birdcage coil. The positivity constraint is a valuable tool for removing some artefacts, but the centre of the reconstruction domain still has some issues which can be avoided with more sophisticated post-processing.

In the future, more research should be performed to simulate the incident field better, as the algorithm heavily depends on the incident field. A better estimation of the shielding effect could be implemented in the incident field simulation. Moreover, finite antennas should be modelled, and the loading of the head should be considered. Another option could be to use the Sim4life software to create the incident fields by inserting the empty head model of Duke. In this way, the incident fields are very close to the incident fields underlying the actual data. Additionally, the algorithm could benefit from an appropriate initialisation. For example, the boundaries seen in the intensity images could be used as a starting point to give each tissue type an approximate value. Besides the initialisation, the combining of the different reconstructions should be researched more. This includes the outlier removal but also balancing the value levels between different reconstructions. An other option would be to put more effort in making the 3D-CSI algorithm faster. A suggestion could be to use Newton's method instead of gradient descent. Lastly, it could be interesting to look at different body parts, as the head is a circular and relatively symmetric body part compared with, for example, the chest slice. However, there is no dataset available for this yet.

References

[1] Freddie Bray et al. “Global cancer statistics 2022: GLOBOCAN estimates of incidence and mortality worldwide for 36 cancers in 185 countries”. In: *CA: A Cancer Journal for Clinicians* (Apr. 2024). ISSN: 0007-9235. DOI: 10.3322/caac.21834.

[2] David Crosby et al. *Early detection of cancer*. Mar. 2022. DOI: 10.1126/science.aay9040.

[3] Peter Goode. *Medical Devices and Systems*. Tech. rep. 2006.

[4] Xiaotong Zhang, Jiaen Liu, and Bin He. “Magnetic-resonance-based electrical properties tomography: A review”. In: *IEEE Reviews in Biomedical Engineering* 7 (2014), pp. 87–96. ISSN: 19411189. DOI: 10.1109/RBME.2013.2297206.

[5] Jiaen Liu et al. *Electrical Properties Tomography Based on B1 Maps in MRI: Principles, Applications, and Challenges*. Nov. 2017. DOI: 10.1109/TBME.2017.2725140.

[6] Edmond Balidemaj et al. “Feasibility of electric property tomography of pelvic tumors at 3T”. In: *Magnetic Resonance in Medicine* 73.4 (Apr. 2015), pp. 1505–1513. ISSN: 15222594. DOI: 10.1002/mrm.25276.

[7] Reijer L. Leijsen et al. “3-D Contrast Source Inversion-Electrical Properties Tomography”. In: *IEEE Transactions on Medical Imaging* 37.9 (Sept. 2018), pp. 2080–2089. ISSN: 1558254X. DOI: 10.1109/TMI.2018.2816125.

[8] Reijer Leijsen et al. “Developments in electrical-property tomography based on the contrast-source inversion method”. In: *Journal of Imaging* 5.2 (Feb. 2019). ISSN: 2313433X. DOI: 10.3390/jimaging5020025.

[9] Reijer Leijsen et al. “Electrical properties tomography: A methodological review”. In: *Diagnostics* 11.2 (Feb. 2021). ISSN: 20754418. DOI: 10.3390/diagnostics11020176.

[10] Ulrich Katscher and Cornelius A.T. van den Berg. *Electric properties tomography: Biochemical, physical and technical background, evaluation and clinical applications*. Aug. 2017. DOI: 10.1002/nbm.3729.

[11] Edmond Balidemaj et al. “CSI-EPT: A Contrast Source Inversion Approach for Improved MRI-Based Electric Properties Tomography”. In: *IEEE Transactions on Medical Imaging* 34.9 (Sept. 2015), pp. 1788–1796. ISSN: 1558254X. DOI: 10.1109/TMI.2015.2404944.

[12] Reijer Leijsen et al. “Transverse-EPT: A Local First Order Electrical Properties Tomography Approach Not Requiring Estimation of the Incident Fields”. In: *Progress In Electromagnetics Research M* 102 (2021), pp. 137–148. ISSN: 19378726. DOI: 10.2528/PIERM21021006.

[13] Patrick S. Fuchs et al. “First-Order Induced Current Density Imaging and Electrical Properties Tomography in MRI”. In: *IEEE Transactions on Computational Imaging* 4.4 (Oct. 2018), pp. 624–631. ISSN: 2573-0436. DOI: 10.1109/tci.2018.2873407.

[14] Peter R.S. Stijnman et al. “Transceive phase corrected 2D contrast source inversion-electrical properties tomography”. In: *Magnetic Resonance in Medicine* 85.5 (May 2021), pp. 2856–2868. ISSN: 15222594. DOI: 10.1002/mrm.28619.

[15] Andreas Christ et al. “The Virtual Family - Development of surface-based anatomical models of two adults and two children for dosimetric simulations”. In: *Physics in Medicine and Biology* 55.2 (2010). ISSN: 00319155. DOI: 10.1088/0031-9155/55/2/N01.

[16] T. G. Meerbothe et al. “A database for MR-based electrical properties tomography with in silico brain data—ADEPT”. In: *Magnetic Resonance in Medicine* (2023). ISSN: 15222594. DOI: 10.1002/mrm.29904.

[17] Ulrich Katscher, Dong Hyun Kim, and Jin Keun Seo. *Recent progress and future challenges in MR electric properties tomography*. 2013. DOI: 10.1155/2013/546562.

[18] E K Insko and L Bolinger. “Mapping of the Radiofrequency Field”. In: *Journal of Magnetic Resonance, Series A* 103.1 (1993), pp. 82–85. ISSN: 1064-1858. DOI: https://doi.org/10.1006/jmra.1993.1133. URL: https://www.sciencedirect.com/science/article/pii/S1064185883711332.

[19] Laura I. Sacolick et al. “B1 mapping by Bloch-Siegert shift”. In: *Magnetic Resonance in Medicine* 63.5 (2010), pp. 1315–1322. ISSN: 15222594. DOI: 10.1002/mrm.22357.

[20] Vasily L. Yarnykh. “Actual flip-angle imaging in the pulsed steady state: A method for rapid three-dimensional mapping of the transmitted radiofrequency field”. In: *Magnetic Resonance in Medicine* 57.1 (2007), pp. 192–200. ISSN: 15222594. DOI: 10.1002/mrm.21120.

[21] Kay Nehrke and Peter Börnert. “DREAM-a novel approach for robust, ultrafast, multislice B1 mapping”. In: *Magnetic Resonance in Medicine* 68.5 (2012), pp. 1517–1526. ISSN: 15222594. DOI: 10.1002/mrm.24158.

[22] Astrid L.H.M.W. Van Lier et al. “B1+ phase mapping at 7 T and its application for in vivo electrical conductivity mapping”. In: *Magnetic Resonance in Medicine* 67.2 (2012), pp. 552–561. ISSN: 15222594. DOI: 10.1002/mrm.22995.

[23] Soraya Gavazzi et al. “Transceive phase mapping using the PLANET method and its application for conductivity mapping in the brain”. In: *Magnetic Resonance in Medicine* 83.2 (Feb. 2020), pp. 590–607. ISSN: 15222594. DOI: 10.1002/mrm.27958.

[24] Wyger Brink et al. “Fast Subject-Specific Local SAR and B1+ Prediction for PTx at 7T using only an Initial Localizer Scan”. In: *Proceedings of the 31th Annual Meet*. London, United King dom, 2022. DOI: 10.58530/2022/0387.

[25] Felix Krueger et al. “Rapid estimation of 2D relative B1+-maps from localizers in the human heart at 7T using deep learning”. In: *Magnetic Resonance in Medicine* 89.3 (Mar. 2023), pp. 1002–1015. ISSN: 15222594. DOI: 10.1002/mrm.29510.

[26] Peter M Van Den Berg and Ralph E Kleinman. *A contrast source inversion method*. Tech. rep. 1997, pp. 1607–1620.

[27] Aria Abubakar et al. “Application of the finite-difference contrast-source inversion algorithm to seismic full-waveform data”. In: *Geophysics* 74.6 (2009). ISSN: 00168033. DOI: 10.1190/1.3250203.

[28] Amer Zakaria, Ian Jeffrey, and Joe Lovetri. *FULL-VECTORIAL PARALLEL FINITE-ELEMENT CONTRAST SOURCE INVERSION METHOD*. Tech. rep. 2013, pp. 463–483.

[29] Aria Abubakar and Peter M. Van Den Berg. “Three-dimensional nonlinear inversion in cross-well electrode logging”. In: *Radio Science* 33.4 (1998), pp. 989–1004. ISSN: 00486604. DOI: 10.1029/98RS00975.

[30] Edmond Balidemaj et al. “CSI-EPT: A novel contrast source approach to MRI based electric properties tomography and patient-specific SAR”. In: *Proceedings of the 2013 International Conference on Electromagnetics in Advanced Applications, ICEAA 2013*. June 2013, pp. 668–671. ISBN: 978-1-4673-5705-0. DOI: 10.1109/ICEAA.2013.6632328.

[31] Reijer L. Leijsen et al. “Effects of Simulated Error-Sources on Different 3-D CSI-EPT Strategies”. In: *IEEE Transactions on Computational Imaging* 7 (2021), pp. 713–723. ISSN: 23339403. DOI: 10.1109/TCI.2021.3094742.

[32] Necip Gurler and Yusuf Ziya Ider. “FEM based Design and Simulation Tool for MRI Birdcage Coils including Eigenfrequency Analysis”. In: Milan: COMSOL Conference, 2012. URL: http://hdl.handle.net/11693/52381.

[33] Bob Van Den Bergen et al. “Ultra fast electromagnetic field computations for RF multi-transmit techniques in high field MRI”. In: *Physics in Medicine and Biology* 54.5 (2009), pp. 1253–1264. ISSN: 00319155. DOI: 10.1088/0031-9155/54/5/010.

[34] P M Van Den Berg and A Abubakar. *CONTRAST SOURCE INVERSION METHOD: STATE OF ART*. Tech. rep. 2001, pp. 189–218.

[35] P M Van Den Berg, A L Van Broekhoven, and A Abubakar. *Extended contrast source inversion*. Tech. rep. 1999, pp. 1325–1344. URL: http://iopscience.iop.org/0266-5611/15/5/315.

[36] R Remis and E Charbon. “An Electric Field Volume Integral Equation Approach to Simulate Surface Plasmon Polaritons”. In: *Advanced Electromagnetics* 2.1 (Feb. 2013), pp. 15–24. DOI: 10.7716/aem.v2i1.23. URL: https://aemjournal.org/index.php/AEM/article/view/23.

[37] E. M. Haacke et al. *Extraction of conductivity and permittivity using magnetic resonance imaging*. Tech. rep. 6. 1991, pp. 723–734. URL: http://iopscience.iop.org/0031-9155/36/6/002.

[38] Thomas V. Pollet and Leander van der Meij. “To Remove or not to Remove: the Impact of Outlier Handling on Significance Testing in Testosterone Data”. In: *Adaptive Human Behavior and Physiology* 3.1 (Mar. 2017), pp. 43–60. ISSN: 21987335. DOI: 10.1007/s40750-016-0050-z.

[39] J. Jin. *Electromagnetic Analysis and Design in Magnetic Resonance Imaging*. Ed. by M.R. Neuman. 1st ed. New York: Taylor & Francis, 1999, pp. 137–202.

[40] Youcef Saad and Martin H Schultz. *GMRES: A GENERALIZED MINIMAL RESIDUAL ALGORITHM FOR SOLVING NONSYMMETRIC LINEAR SYSTEMS**. Tech. rep. 3. 1986. URL: https://epubs.siam.org/terms-privacy.

[41] F J Helfferich. *MULTIPLICATIVE CONTRAST SOURCE INVERSION METHOD IN ELECTRICAL PROPERTIES TOMOGRAPHY BASED ON JACOBI MATRIX INVERSION*. Tech. rep. 2024. URL: http://repository.tudelft.nl/..

A

Ella head slice further investigation

A.1. Setting conductivity and relative permittivity to zero

Instead of the implementation proposed in the text, it is also possible to set the conductivity and relative permittivity to zero if the conditions are unmet.

1. If $\Re\{\chi(\boldsymbol{r})\} + 1 \leq 0$ then $\chi_{new}(\boldsymbol{r}) = 1 + j\Im\{\chi_{old}(\boldsymbol{r})\}$.
2. If $\Im\{\chi_{old}(\boldsymbol{r})\} \geq 0$ then $\chi_{new}(\boldsymbol{r}) = \Re\{\chi_{old}(\boldsymbol{r})\} + j * 0$.

In Figure A.1, the reconstruction with the implementation with zeros is given. The reconstructions are close to the implementation with the sign flip. Moreover, the minimum cost function is very close together (996 versus 993 iterations). Hence, this implementation is also a reasonable option.

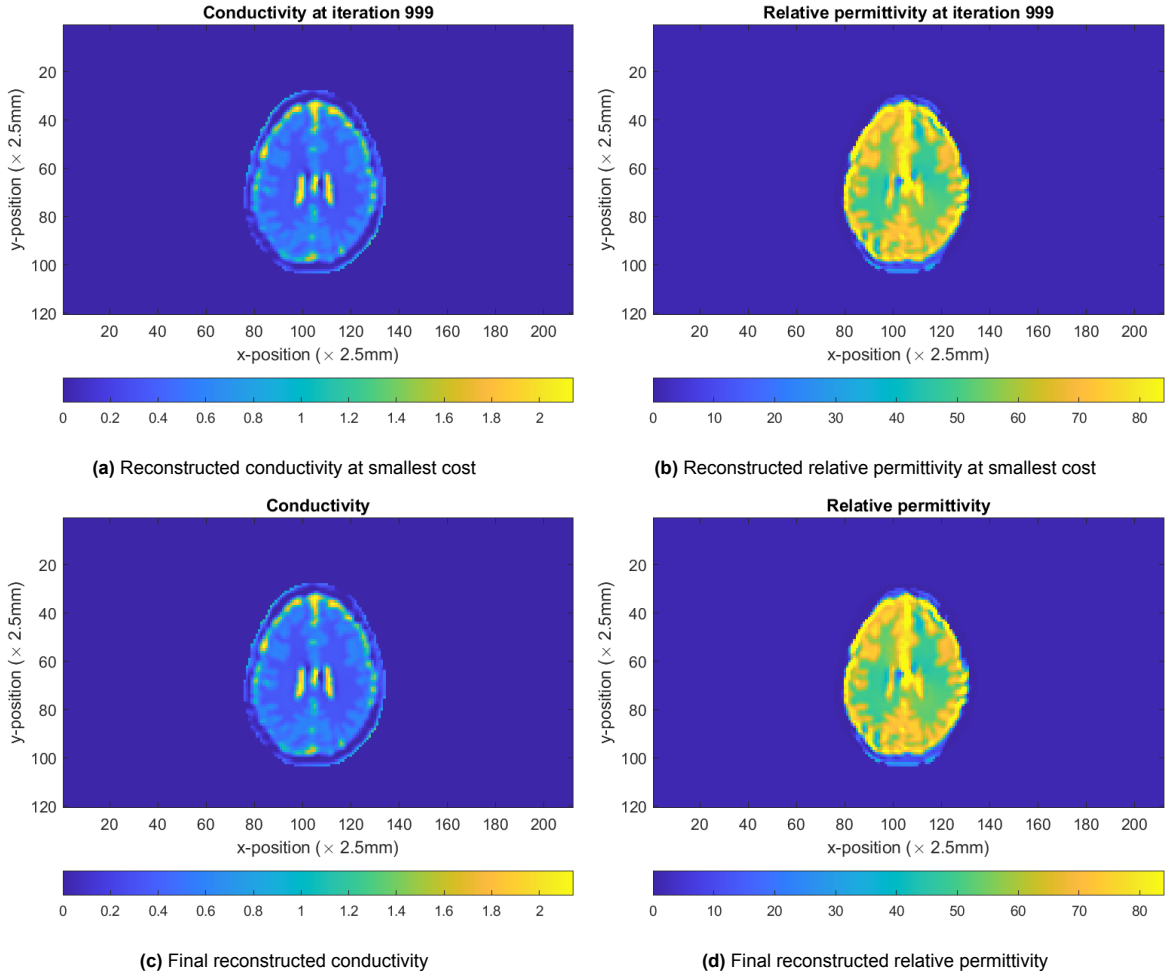

(a) Reconstructed conductivity at smallest cost

(b) Reconstructed relative permittivity at smallest cost

(c) Final reconstructed conductivity

(d) Final reconstructed relative permittivity

Figure A.1: The conductivity (a, c) and relative permittivity (b, d) of slice 320 with the positivity constraint implemented in the second way. The upper row shows the reconstruction at the iteration with the minimum cost functional, and the bottom row shows the final reconstruction.

A.2. No early stopping in robustness analysis

A.2.1. Effect on offset

In Figure A.2, the reconstructions after the 1000th iteration are shown for the case where the offset of the incident field does not match the measured field's offset. If these reconstructions are compared to those in Figure 3.16, the reconstructions with positivity do not deviate much. This similarity is as expected as the 999th iteration is compared to the 1000th iteration. Without the positivity constraint, there are large differences. The later reconstruction is a lot sharper, but artefacts are present, making it more difficult to interpret the images correctly. The reconstruction fails, especially for the relative permittivity. This effect suggests a preference for still using the early stopping and a preference for using the positivity constraint.

A.2.2. Effect on noise

In Figure A.3, the reconstructions are provided at the 1000th iteration when the SNR was 50. If the top row of this figure is compared to the top row in Figure 3.17, the noise is modelled more at the later reconstruction, resulting in worse reconstructions. Even more concerning is that the artefacts seen in the noise-free case are again present, making reconstructions unreliable. The bottom row of Figure A.3 and the top row of Figure 3.18 are similar, but in the last twenty iterations, the noise is more disturbing the image. Therefore, these images show that the early stopping helps create readable images with few artefacts.

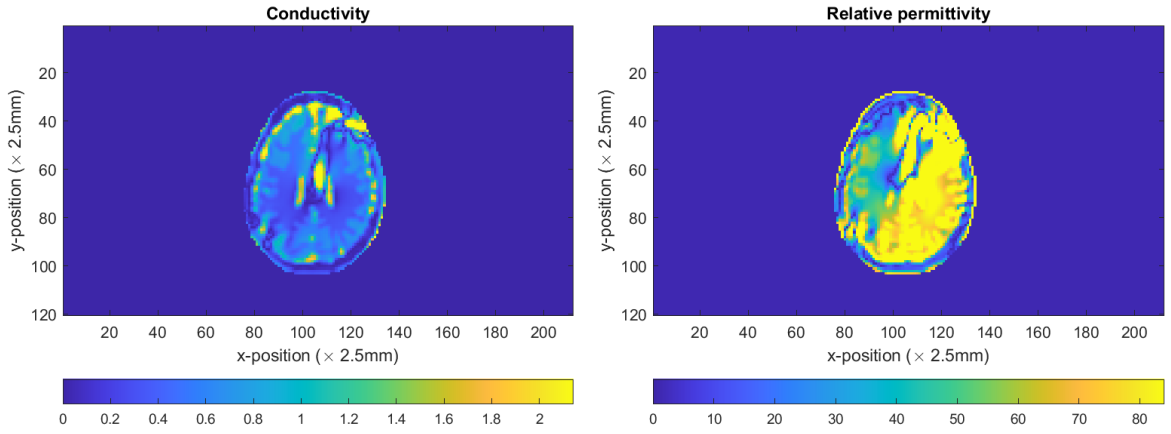

(a) Reconstructed conductivity without positivity

(b) Reconstructed relative permittivity without positivity

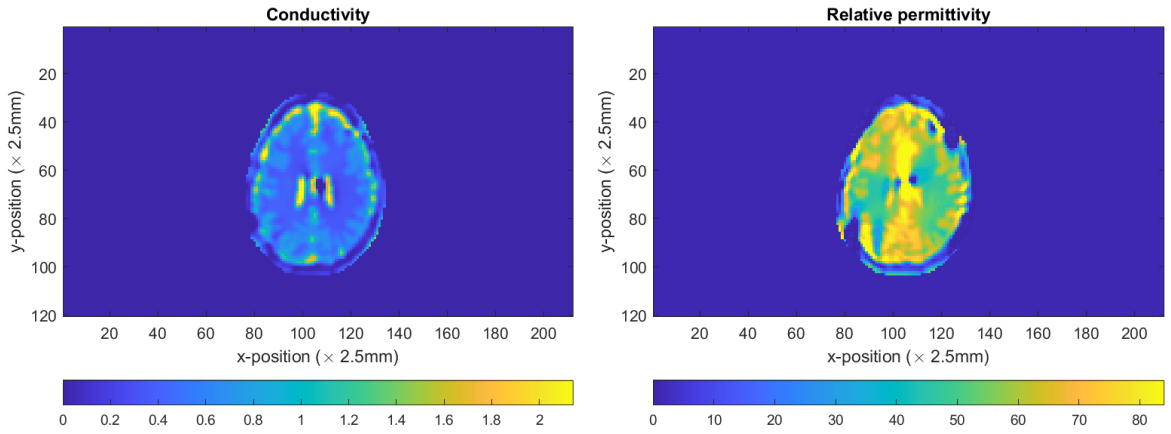

(c) Reconstructed conductivity with positivity

(d) Reconstructed relative permittivity with positivity

Figure A.2: The conductivity (a, c) and relative permittivity (b, d) of slice 320 with an offset difference of 5° between the measured fields and the incident fields at the 1000th iteration. The upper row shows the reconstructions without positivity constraint, while the bottom shows the reconstruction with positivity constraint.

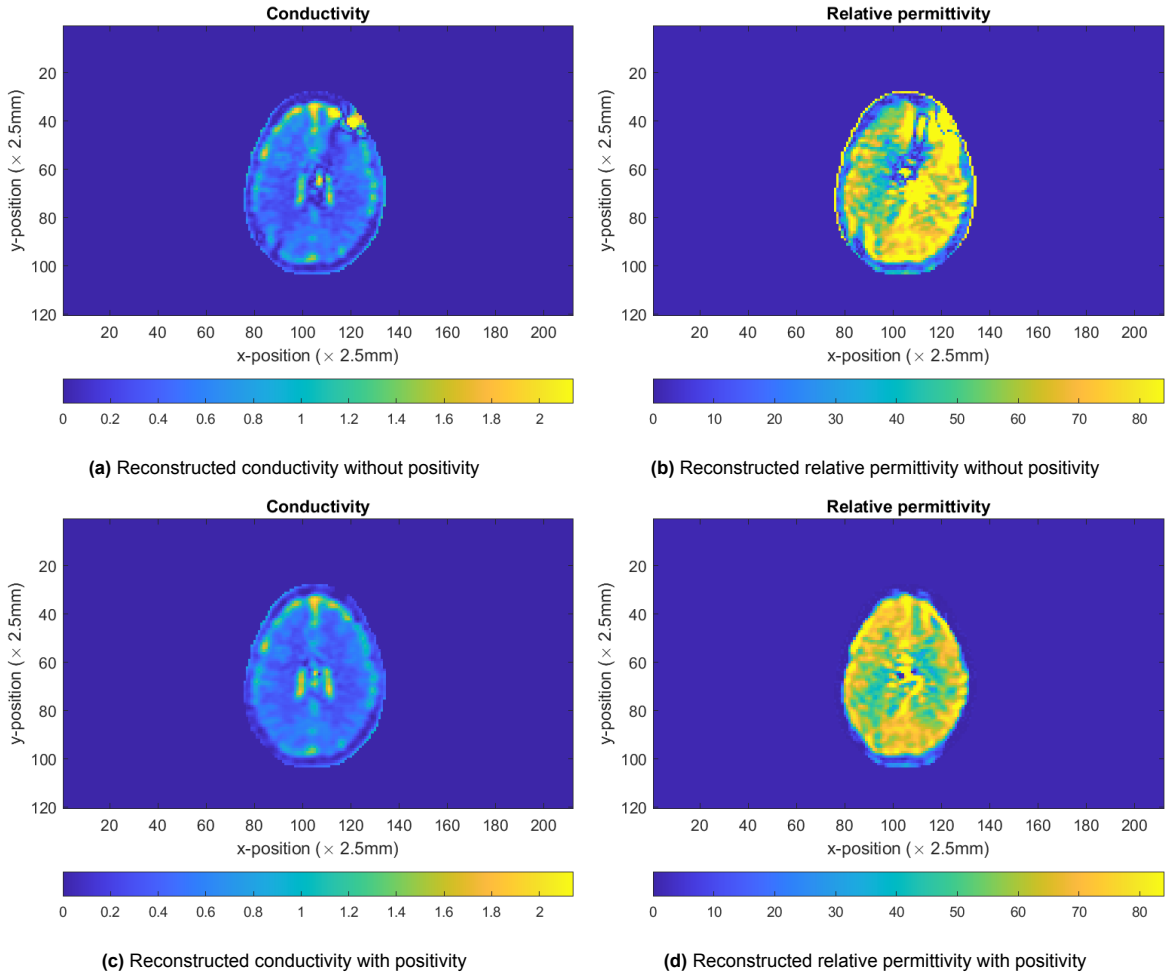

(a) Reconstructed conductivity without positivity

(b) Reconstructed relative permittivity without positivity

(c) Reconstructed conductivity with positivity

(d) Reconstructed relative permittivity with positivity

Figure A.3: The conductivity (a, c) and relative permittivity (b, d) of slice 320 with an SNR of 50 at the 1000th iteration. The upper row shows the reconstructions without positivity constraint, while the bottom shows the reconstruction with positivity constraint.

B

Ella dataset other slices

In this Appendix, two more slices in the Ella dataset are investigated. First, the 2D-CSI algorithm is applied to a leg slice. This slice is interesting as it consists of only a few points, which can cause problems for a global algorithm such as 2D-CSI. The second slice is the pelvis slice, which is of interest as this slice is far less symmetric than the head slice, and therefore, the TPA holds even less here.

B.1. No enhancements

B.1.1. Slice 55

Slice 55, which represents the legs, is analysed first. Figure B.1 shows a dip around iteration 140 in which the cost functional and errors are the smallest. So, this suggests that the reconstructions at the cost functional minimum might be interesting. When the reconstruction in Figure B.2 is analysed, the algorithm has modelled data artefacts. These artefacts can be explained by the fact that the data on the legs is relatively small. Therefore, phase reconstruction can cause problems as there are too few points to support phase reconstruction, and so does EP reconstruction.

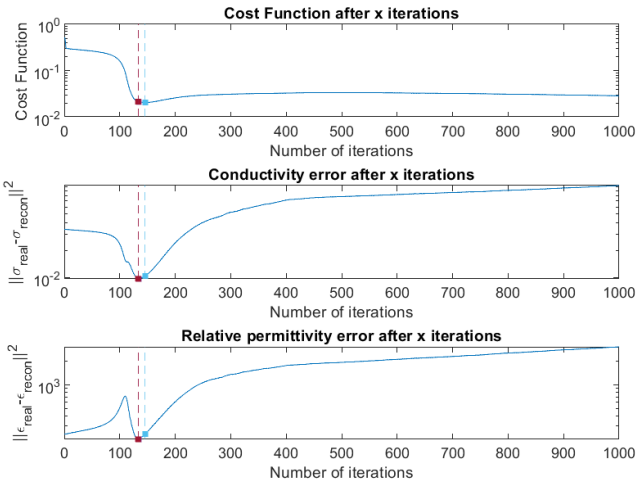

Figure B.1: The algorithm's performance at slice 55 over different iterations is measured using the cost function magnitude, the mean squared error of the conductivity, and the relative permittivity. The light blue, purple, and red vertical lines represent the points at the iteration with the lowest cost function value, conductivity error, and relative permittivity er,ror respectively.

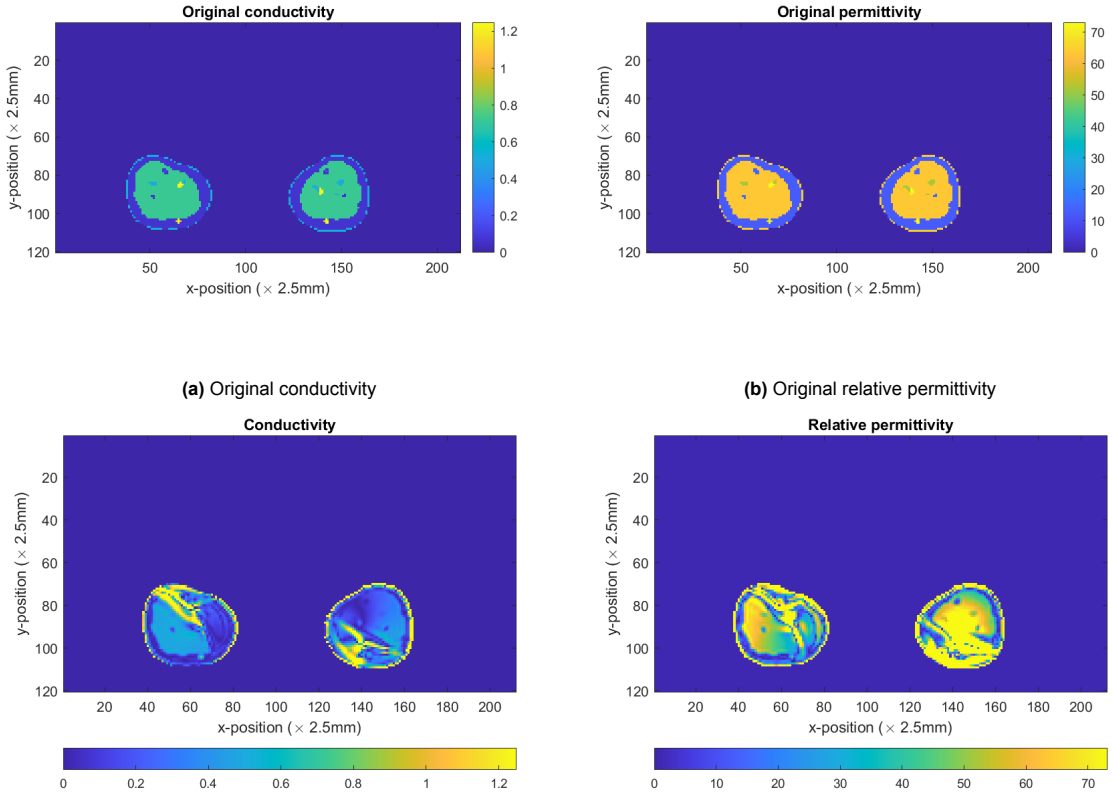

(a) Original conductivity

(b) Original relative permittivity

(c) Final reconstructed conductivity

(d) Final reconstructed relative permittivity

Figure B.2: The conductivity and relative permittivity of slice 55. The upper row shows the original image. The bottom row shows the reconstruction without applying any improvements.

B.1.2. Slice 168

The second slice is the 168th slice (pelvis) of the Ella model. In Figure B.3, the cost function first decreases and, after 275, starts to increase again. The mean squared error for the conductivity and relative permittivity shows similar patterns except in the first iterations. Therefore, a logical update could be to look at the result at the lowest cost functional, which is implemented later. Figure B.4 shows the reconstruction results without any adjustments. The reconstruction algorithm can capture parts of the original data, but it fails, especially in the middle, due to the low electric field and on the diagonal. This effect on the diagonal is expected as the CSI algorithm uses the transceive phase and an estimate of the receive phase instead of the transmit phase for the reconstruction, which often results in unreliable data on the diagonal [7, 8].

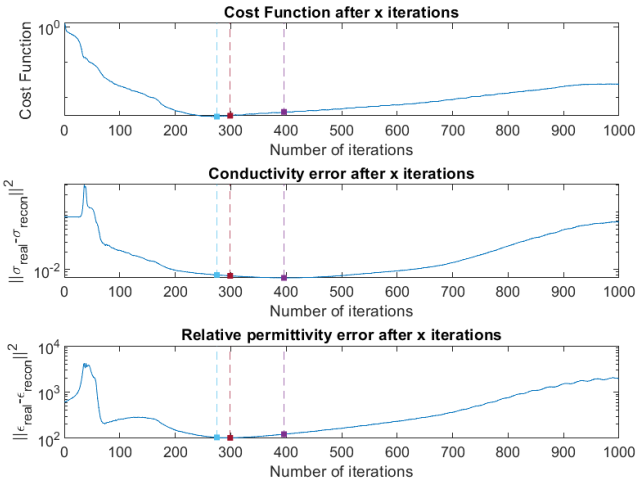

Figure B.3: The algorithm's performance for slice 168 over different iterations was measured using the cost functional magnitude, the mean squared error of the conductivity, and the relative permittivity. The light blue, purple, and red vertical lines represent the points at the iteration with the lowest cost function value, conductivity error, and relative permittivity error, respectively.

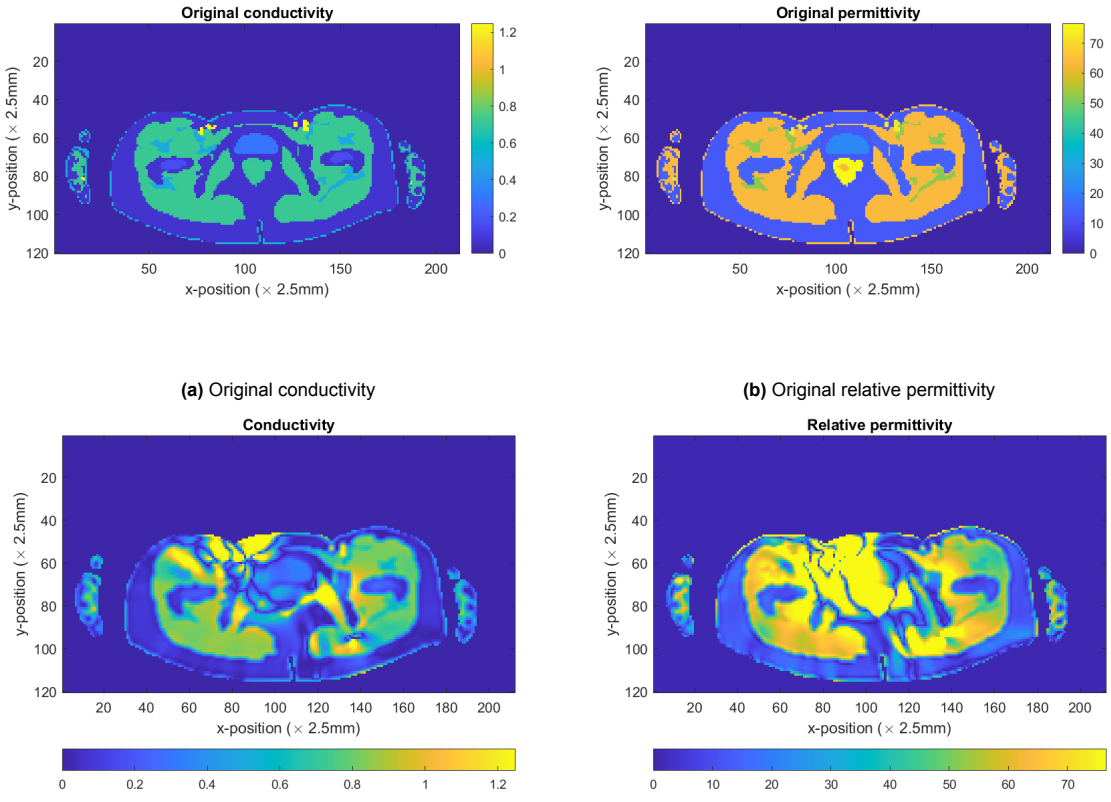

(a) Original conductivity

(b) Original relative permittivity

(c) Final reconstructed conductivity

(d) Final reconstructed relative permittivity

Figure B.4: The conductivity and relative permittivity of slice 168. The upper row shows the original image, and the bottom row shows the reconstruction without applying any improvements.

B.2. Minima

In the cost functional and error images, the graphs would decrease first and then increase again. If the reconstruction at those minima is better than the final reconstruction, then the reconstruction time could be reduced.

B.2.1. Slice 55

The first update is to look at the EPs at the minima of the cost functional (iteration 146), conductivity reconstruction error (iteration 134), and the relative permittivity reconstruction error (iteration 133). Note that the minima for both errors can only be calculated if the EPs are known before the reconstruction. Hence, the results at the minimum of the cost functional are available in a real live setting, while the error minima can only be found in simulations. Figure B.5 presents the reconstructions at the minima. The three reconstructions are very similar. However, the reconstructions are still far from the original conductivity and relative permittivity. When the reconstructions at the minima are compared with the final reconstructions, the final reconstruction does include more details of the original EPs. Still, the values are less reliable, and more spots have large signal values. Therefore, the early stopping seems to have a better indication of the values but filters out all details. In this case, all the reconstructions are not reliable enough. This behaviour can be due to the relatively small size and disconnection between the two legs.

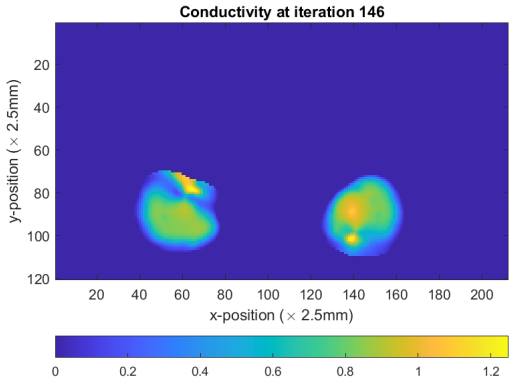

(a) Reconstructed conductivity at smallest cost

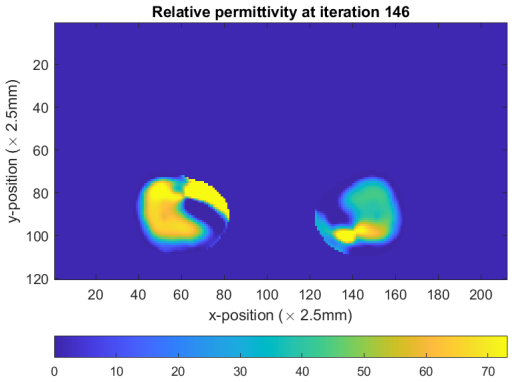

(b) Reconstructed relative permittivity at smallest cost

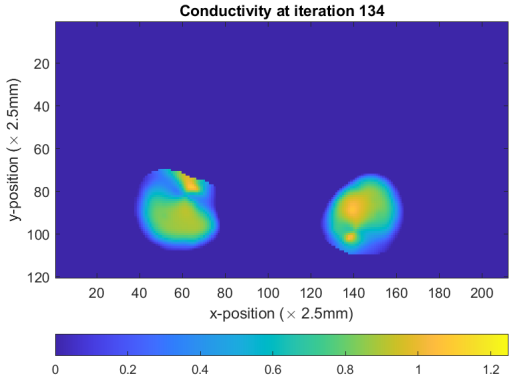

(c) Reconstructed conductivity with best conductivity

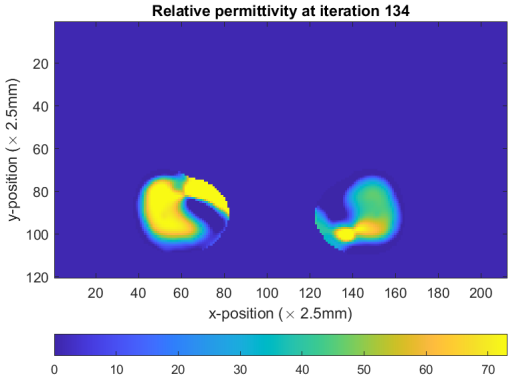

(d) Reconstructed relative permittivity with the best conductivity

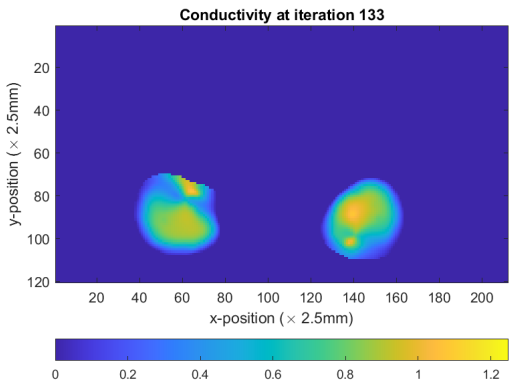

(e) Reconstructed conductivity with best relative permittivity

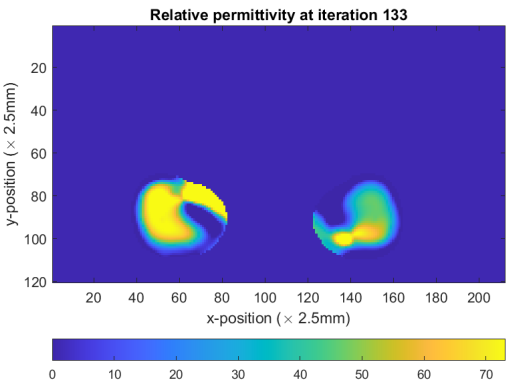

(f) Reconstructed relative permittivity with best relative permittivity

Figure B.5: The conductivity and relative permittivity of slice 55. The upper, middle and bottom rows show the reconstructions at the minima of the cost functional, conductivity error and relative permittivity error, respectively.

B.2.2. Slice 168

For the pelvis slice, the cost functional, conductivity error, and relative permittivity error minima are at iteration 275, 396, and 299, respectively. The three reconstructions are very similar. If the reconstruction at the 1000th iteration is compared to these reconstructions, these earlier reconstructions are much closer to the original EPs. Moreover, the artefacts on the diagonal are reduced. Only the middle of the relative permittivity still has some errors. The algorithm modelling errors at later iterations cause better reconstructions at an earlier iteration.

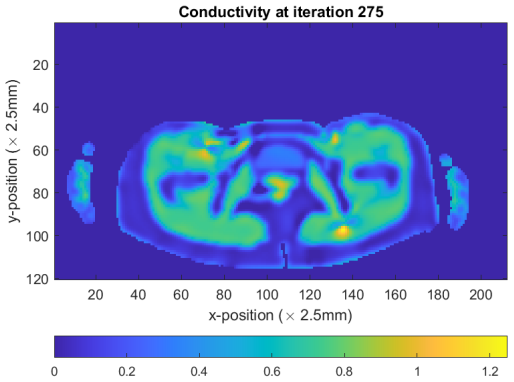

(a) Reconstructed conductivity at smallest cost

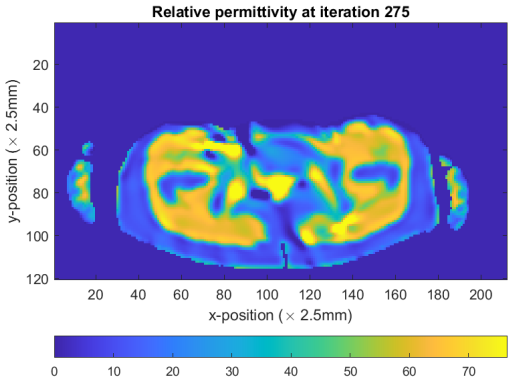

(b) Reconstructed relative permittivity at smallest cost

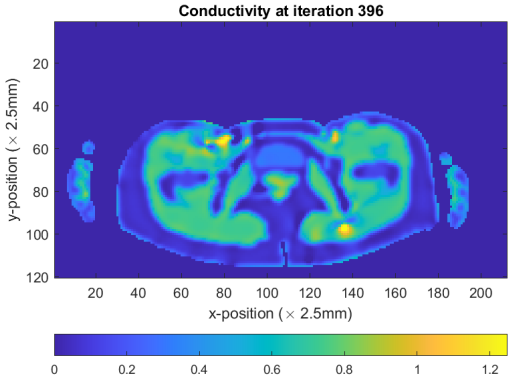

(c) Reconstructed conductivity with best conductivity

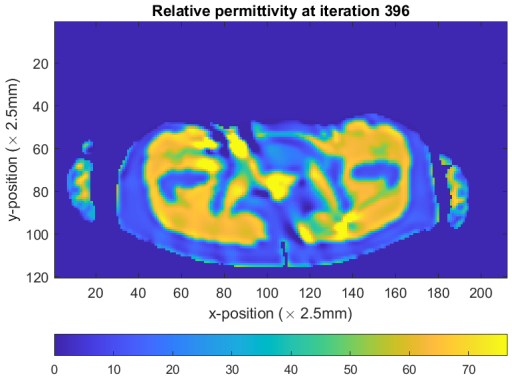

(d) Reconstructed relative permittivity with the best conductivity

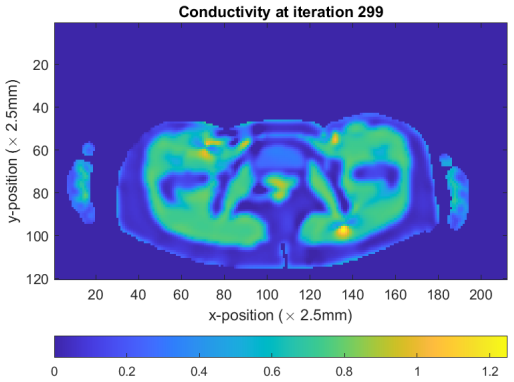

(e) Reconstructed conductivity with best relative permittivity

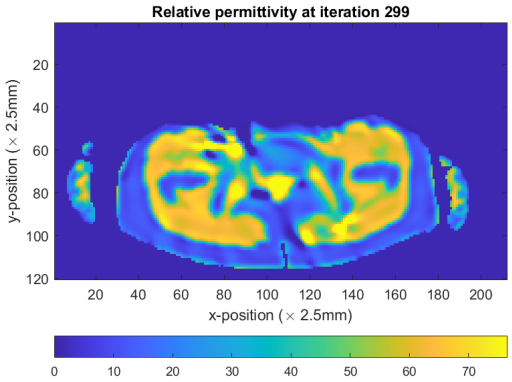

(f) Reconstructed relative permittivity with best best relative permittivity

Figure B.6: The conductivity and relative permittivity of slice 168. The upper, middle and bottom rows show the reconstructions at the minima of the cost functional, conductivity error and relative permittivity error, respectively.

B.3. Positivity of conductivity and relative permittivity

As mentioned in Chapter 3, a second possible update is implementing a positivity constraint for both the conductivity and the relative permittivity. As the legs show problems caused by the small number of points, it is decided that further investigations should be focused only on slice 168.

B.3.1. Slice 168

After implementing the positivity constraint, the results become as in Figure B.7. When eyeballing the final reconstruction without positivity (Figure B.4) and the final reconstruction with positivity, the results with positivity are improved in the middle. Furthermore, comparing the reconstructions with positivity constraints shows that the results at iteration 257 are preferred above the final reconstruction as the final reconstructions have artefacts in the centre and on the diagonal. Lastly, when the results of the EPs without positivity at iteration 275 (Figure B.6) and with positivity at iteration 257 are observed, then the results are closely related. However, the positivity constraint does improve the centre of the reconstruction. The enhancement is primarily noted in the reconstruction of the relative permittivity. However, the algorithm still has some difficulties reconstructing the relative permittivity boundaries. These difficulties can be caused by the relatively small displacement currents at 3T.

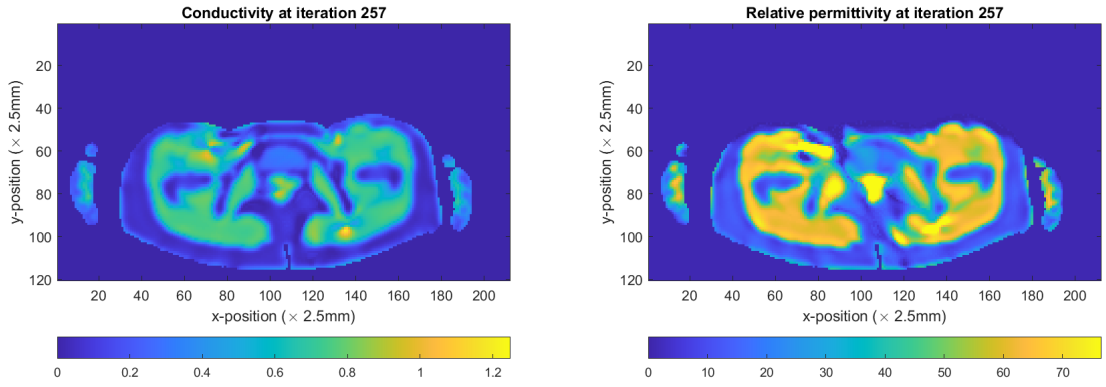

(a) Reconstructed conductivity at smallest cost

(b) Reconstructed relative permittivity at smallest cost

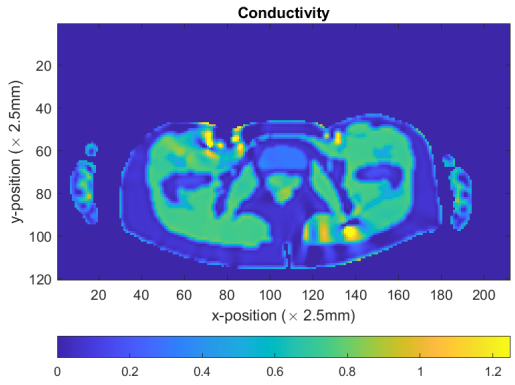

(c) Final reconstructed conductivity

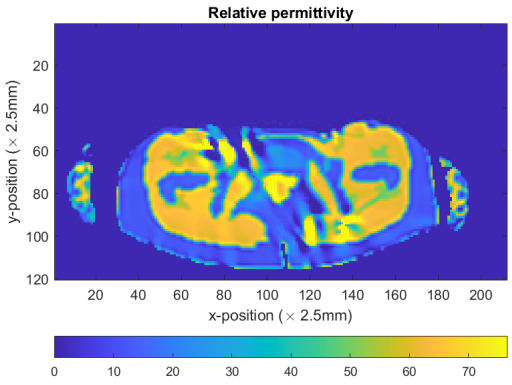

(d) Final reconstructed relative permittivity

Figure B.7: The conductivity and relative permittivity of slice 168 with the positivity constraint implemented. The upper row shows the reconstruction at the iteration with the minimum cost functional, and the bottom row shows the final reconstruction.

B.4. Initialize with HEPT

Another update which might improve the algorithm is adding an appropriate initial condition. The first contrast source estimate in the images above is determined using back projection as discussed in [34] Equation 35. A better initialisation could be using the results from HEPT. This HEPT initialisation might improve both the final result and speed up the convergence. However, the CSI algorithm should be able to remove the boundary error of HEPT, which is researched here.

B.4.1. Slice 168

In Figure B.8, the reconstructions are provided when the algorithm is initialised with HEPT results. After the first iteration, the reconstructions include most of the outlines. However, the values are not representative yet, which is reasonable as HEPT at the tissue boundaries becomes very large, resulting in clear outlines. If the iterations proceed, the reconstruction is improved, and in the 766th iteration, the cost function is minimal. The resulting conductivity and relative permittivity are close to the original images (Figure B.4).

Furthermore, when this result is compared to the 257th iteration with back projection (Figure B.6), the new reconstruction seems sharper but with more variations over a single area and boundary errors. It is important to note that the HEPT adds 509 iterations to find the optimal solution. So, using HEPT as an initial condition is slower and is not much more accurate than the previous results. One last remark: in this case, HEPT is based on noiseless information. The advancements are less in a noisy environment as the HEPT reconstructions are primarily affected by noise.

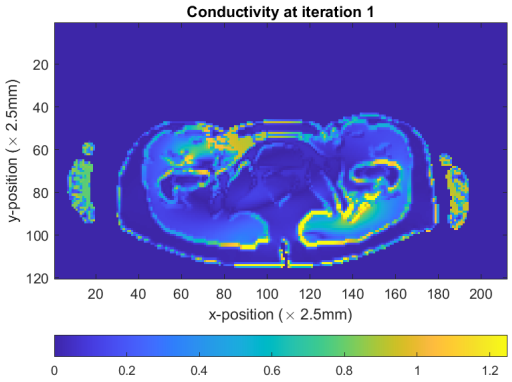

(a) Reconstructed conductivity after first iteration

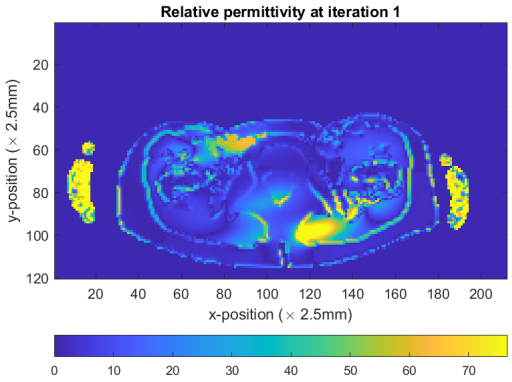

(b) Reconstructed relative permittivity after first iteration

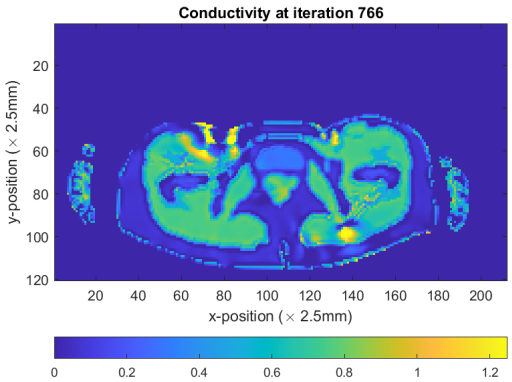

(c) Reconstructed conductivity at smallest cost

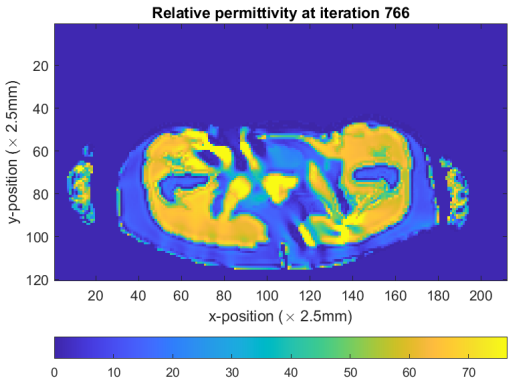

(d) Reconstructed relative permittivity at smallest cost

Figure B.8: The conductivity and relative permittivity of slice 168. The upper row shows the reconstruction after the first iteration. The bottom row shows the reconstruction at the cost functional minimum. The positivity constraint was implemented in these reconstructions.

C

Effect of fields magnitude

The magnitude of the ADEPT dataset is not matched to the magnitude of the incident fields. This match is not straightforward as the dataset is 3D while the incident fields are created under the 2D assumption. Therefore, this is done manually. First, a factor between the maximum of the incident and the maximum of the total field is calculated, which results in the two factors

$$\kappa_{B;max} = \frac{\max(B^{+;inc})}{\max(B^{+;tot})} \text{ and } \kappa_{E;max} = \frac{\max(\boldsymbol{E}^{inc})}{\max(\boldsymbol{E}^{tot})}. \tag{C.1}$$

An extra parameter is introduced to match the field to provide more freedom. Therefore, the incident fields are scaled to

$$B^{+;inc_{sc}} = \frac{B^{+;inc}}{\kappa_{B;max} * \kappa_{B;sc}} \text{ and } \boldsymbol{E}^{inc_{sc}} = \frac{\boldsymbol{E}^{inc}}{\kappa_{E;max} * \kappa_{E;sc}}, \tag{C.2}$$

where $B^{+;inc_{sc}}$, and $\boldsymbol{E}^{inc_{sc}}$ are the scaled transmit and electric incident fields. Furthermore, $\kappa_{B;sc}$, and $\kappa_{E;sc}$ the additional scaling factors. In Figure C.1, the conductivity reconstructions with varying $\kappa_{B;sc}$ is provided while $\kappa_{E;sc} = 1$. If the factor is too small, the algorithm does not converge or only converges at a small area. A scaling factor between 3 and 25 results in good reconstructions. The larger factors result in larger convergence areas, however, it does create overexposed areas. This is seen by the scaling factors larger than 25. The transmit field scaling factor, which seems to be best considering both sides, is $\kappa_{B;sc} = 10$. In Figure C.2, the $\kappa_{B;sc} = 10$ and the $\kappa_{E;sc}$ is varied. When the scaling factor is too small (below 0.5) the values are much underestimated. The reconstructions between 0.5 and 1 are proper. Increasing the values further results in more and more data getting lost. At a factor of 5 already, almost no information is left. Increasing even further results in an entire blue reconstruction. It is again chosen to meet in the middle and set the $\kappa_{B;sc} = 0.75$.

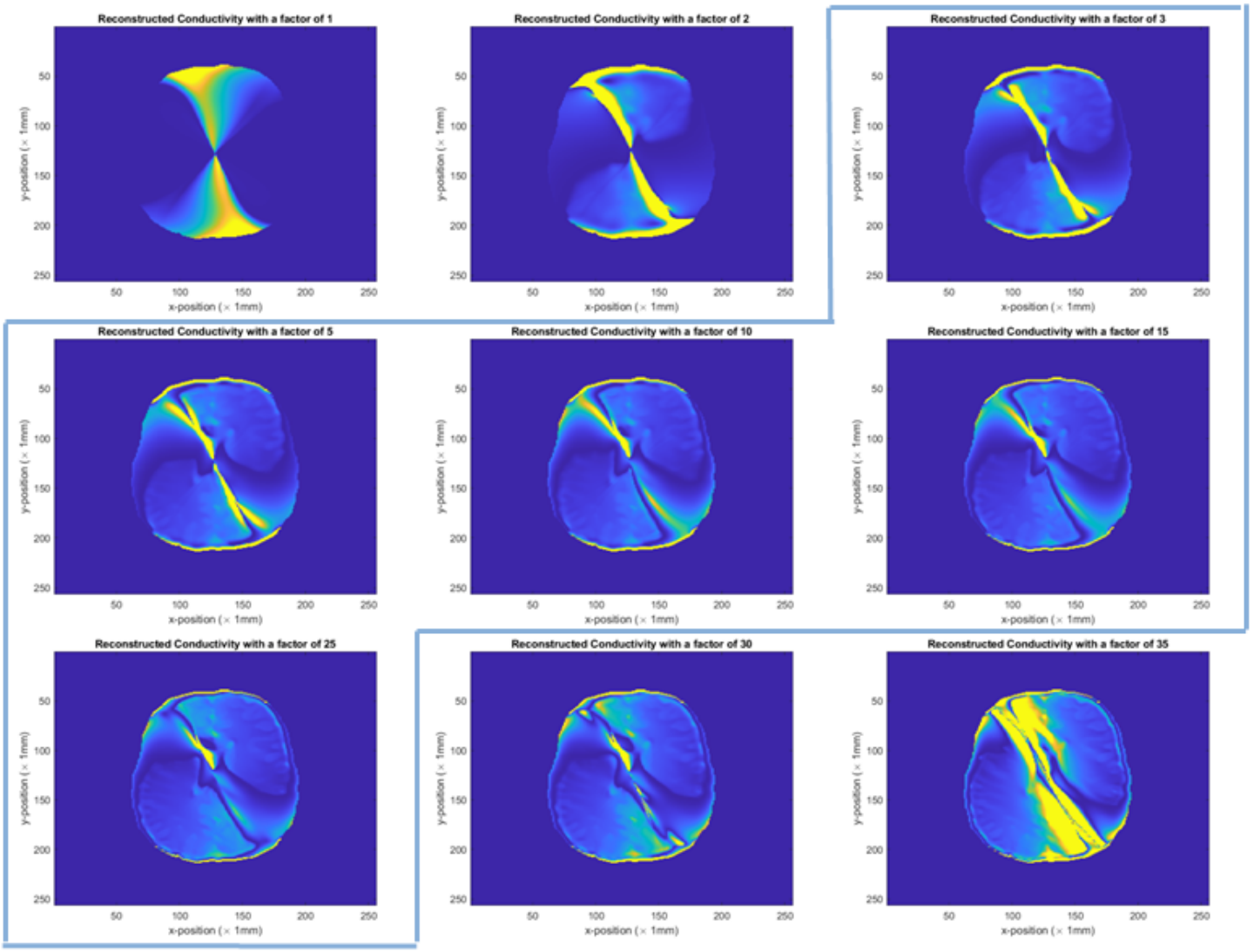

Figure C.1: Different conductivity reconstructions are provided with varying transmit scaling factors while setting $\kappa_{E;sc} = 1$. The reconstructions inside the blue outline show decent reconstructions. The positivity constraint is applied in these images and the ADEPT dataset is not converted.

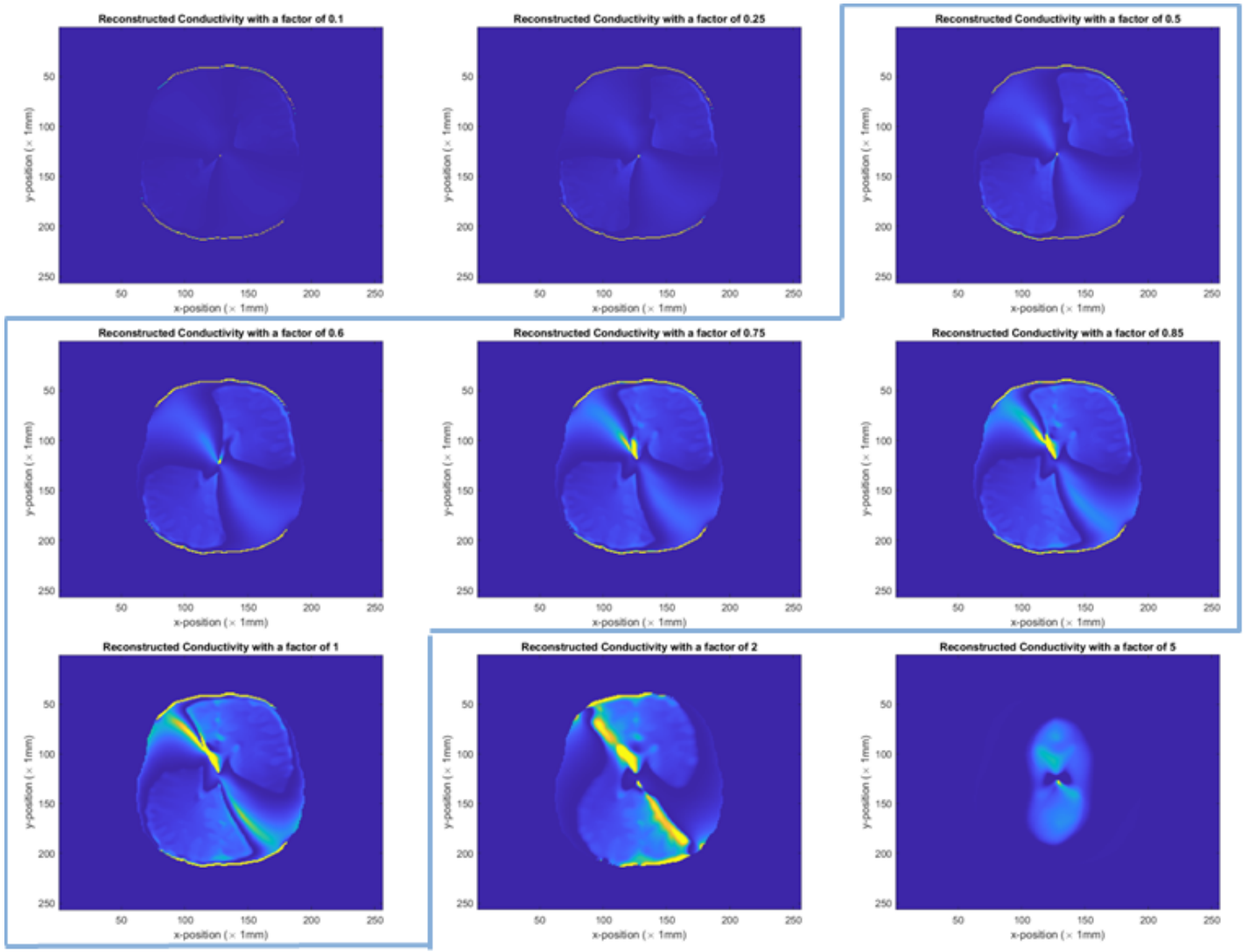

Figure C.2: Different conductivity reconstructions are provided with varying electric field scaling factors while setting $\kappa_{B;sc} = 10$. The reconstructions inside the blue outline show decent reconstructions. The positivity constraint is applied in these images and the ADEPT dataset is not converted.